

UNCLASSIFIED

AD NUMBER

AD485277

LIMITATION CHANGES

TO:

Approved for public release; distribution is unlimited.

FROM:

Distribution authorized to U.S. Gov't. agencies and their contractors; Critical Technology; JUL 1966. Other requests shall be referred to Arnold Engineering Development Center, Arnold AFS, TN. This document contains export-controlled technical data.

AUTHORITY

AEDC ltr, 23 Nov 1971

THIS PAGE IS UNCLASSIFIED

AEDC-TR-66-103

eyo 10

AUG 05 1985

JUN 1 1988

JUL 7 1968

OCT 21 1990

MAY 1 1992



EVALUATION OF SHORT-DURATION ROCKET ENGINE TECHNIQUE FOR BASE HEAT TESTING WITH EXTERNAL AIRFLOW

Property of U. S. Air Force
AEDC LIBRARY
F40600-81-G-0004

John G. Dawson, Jr.

ARO, Inc.

**TECHNICAL REPORTS
FILE COPY**

AF 94(600)1200

July 1966

~~This document is subject to special export controls and each transmittal to foreign governments or foreign nationals may be made only with prior approval of Arnold Engineering Development Center.~~

This document has been approved for public release and sale; its distribution is unlimited. (per AF Ltr, 23 Nov. 71, XON)

ROCKET TEST FACILITY
ARNOLD ENGINEERING DEVELOPMENT CENTER
AIR FORCE SYSTEMS COMMAND
ARNOLD AIR FORCE STATION, TENNESSEE

NOTICES

When U. S. Government drawings specifications, or other data are used for any purpose other than a definitely related Government procurement operation, the Government thereby incurs no responsibility nor any obligation whatsoever, and the fact that the Government may have formulated, furnished, or in any way supplied the said drawings, specifications, or other data, is not to be regarded by implication or otherwise, or in any manner licensing the holder or any other person or corporation, or conveying any rights or permission to manufacture, use, or sell any patented invention that may in any way be related thereto.

Qualified users may obtain copies of this report from the Defense Documentation Center.

References to named commercial products in this report are not to be considered in any sense as an endorsement of the product by the United States Air Force or the Government.

EVALUATION OF SHORT-DURATION ROCKET ENGINE
TECHNIQUE FOR BASE HEAT TESTING
WITH EXTERNAL AIRFLOW

John G. Dawson, Jr.
ARO, Inc.

This document has been approved for public release
and sale; its distribution is unlimited. *(per AF letter, 23 Nov. 71, XCN)*

This document is subject to special export controls
and each transmittal to foreign governments or foreign
nationals may be made only with prior approval of
Arnold Engineering Development Center.

FOREWORD

The work presented herein was sponsored by Headquarters, Arnold Engineering Development Center (AEDC), Air Force Systems Command (AFSC), Arnold Air Force Station, Tennessee, under System 921A. The model was designed for NASA, Marshall Space Flight Center, Huntsville, Alabama, by Cornell Aeronautical Laboratory, Inc. (CAL), Buffalo, N. Y., and was used by permission of NASA. Technical assistance was provided by CAL.

The results of the tests were obtained by ARO, Inc. (a subsidiary of Sverdrup & Parcel and Associates, Inc.), contract operator of AEDC under Contract AF40(600)-1200. The test was conducted in Propulsion Engine Test Cell (T-1) of the Rocket Test Facility (RTF) from October 7 to November 4, 1965, under ARO Project Number RA0417, and the manuscript was submitted for publication on April 18, 1966.

This technical report has been reviewed and is approved.

John W. Hitchcock
Major, USAF
AF Representative, RTF
DCS/Test

Jean A. Jack
Colonel, USAF
DCS/Test

ABSTRACT

Base recirculation data were obtained on a 5.47-percent-scale model of the Saturn I-Block II booster at trajectory Mach numbers of 1.16 and 1.63. The rocket nozzle flow was produced by use of the Cornell Aeronautical Laboratory short-duration combustor. The turbine exhaust gases were simulated by hydrogen. The test objectives were (1) to compare results obtained by the short-duration technique to those obtained by long-duration test methods and (2) to evaluate the operational advantages of the short-duration method as compared to other techniques. A comparison of model test to flight test data is also presented.

CONTENTS

	<u>Page</u>
ABSTRACT	iii
NOMENCLATURE	viii
I. INTRODUCTION	1
II. APPARATUS	2
III. PROCEDURE	6
IV. RESULTS AND DISCUSSION	8
V. SUMMARY OF RESULTS	20
APPENDIXES	20
I. Summary of Non-Steady Flow Equations for a Sonic Venturi	21
II. Method of Determining Hydrogen Flow Rate	24
III. Methods of Calculation	25
IV. Determination of Jet Boundaries	27
REFERENCES	29

ILLUSTRATIONS

Figure

1. Comparison of Model with Full-Scale SI-Block II Booster Afterbody	
a. Full-Scale Booster Afterbody	33
b. 5.47-Percent-Scale Model Afterbody	34
2. Schematic of Short-Duration Propellant System	35
3. Charge Tube Venturis	
a. Photograph	36
b. Schematic	37
4. Autovalve	
a. Photograph	38
b. Installation Photograph	39
5. Autovalve Schematic	
a. Open Position	40
b. Closed Position	40
6. Propellant Injector	
a. Components	41
b. Assembly	42

<u>Figure</u>	<u>Page</u>
7. Model Exhaust Nozzle	
a. Photograph	43
b. Schematic	44
8. Outboard Nozzle with 360-deg Exhausterator	
a. Photograph (Short Duration)	45
b. Schematic (Short Duration)	46
c. Schematic (Full Scale)	47
d. Schematic (Long Duration)	47
9. Turbine Exhaust Duct and Hydrogen Chillover Duct Design	48
10. Model External Hardware	
a. Model Air Scoops, Flow Deflectors, and Outboard Engine Shrouds	49
b. Model Fins	50
11. Model Base Shield	
a. Photograph	51
b. Base Pressure Locations	52
c. Base Heat Transfer Gage Locations	53
12. Flame Shield	
a. Photograph	54
b. Instrumentation Locations	55
13. Model Installation	
a. Photograph Mach Number 1.63	56
b. Schematic Mach Number 1.63	57
c. Photograph Mach Number 1.16	58
d. Schematic Mach Number 1.16	59
14. Thin-Film Heat Transfer Gage	
a. Photograph	60
b. Schematic	61
15. Short-Duration Heat Gage Circuit Schematic	62
16. Typical Oscilloscope Chamber Pressure and Heat Transfer Gage Output Photographs.	63
17. Schematic of Lead Zirconium Titanate Short- Duration Pressure Transducer	64
18. Typical Oscillograph of Model Sequence of Operation and Pressure Traces	
a. M = 1.16	65
b. M = 1.63	66

<u>Figure</u>	<u>Page</u>
19. Base Pressure Distribution with Engines Operating	
a. $M = 1.16$, Altitude 26,600 ft, $p_c = 500$ psia . . .	67
b. $M = 1.63$, Altitude 38,000 ft, $p_c = 500$ psia . . .	67
20. Cold Flow Base Pressure	
a. Cold Flow Base Pressure versus Mach Number	68
b. Cold Flow Base Pressure versus Altitude	68
21. Effects of Altitude and Combustor Pressure on Base Pressure	
a. Model Data	69
b. Comparison of Model and Flight Data	69
22. Jet Boundaries Calculated for Various Altitudes	
a. 33,000 ft	70
b. 38,000 ft	70
c. 45,000 ft	70
d. 50,000 ft	70
e. 38,000 ft, Comparison of $\gamma = 1.15$ and 1.25 . . .	71
23. Ambient-to-Chamber Pressure Ratio versus Altitude	72
24. Flame Shield Pressure versus Altitude	73
25. Flame Shield-to-Base Pressure Ratio versus Altitude	73
26. Model Base Total Heat Transfer Distribution at $M = 1.63$ and 38,000 ft	74
27. Comparison of Model Data and Flight Test Base Heating Data	75
28. Typical Long-Duration Base Calorimeter Temperature and Heat Transfer-Time Histories	
a. Temperature	76
b. Heat Transfer	76
29. Typical Temperature and Heat Transfer-Time History for a Flight Test Heat Transfer Gage	77
30. Flame Shield Heat Transfer Rate	
a. Comparison of Short- and Long-Duration Model Data	78
b. Comparison of Model and Flight Data	79

TABLES

	<u>Page</u>
I. Engine and Afterbody Design Parameters	81
II. Instrumentation	82

NOMENCLATURE

A	Area, ft^2
a	Acoustic velocity, ft/sec
F	View factor of radiation heat transfer gage
h_c	Film coefficient, $\text{Btu}/\text{ft}^2\text{-sec-}^\circ\text{R}$
k	Thermal conductivity, $\text{Btu}/\text{ft-sec-}^\circ\text{R}$
ℓ	Length
M	Mach number
O/F	Oxidizer-to-fuel ratio
Pr	Prandtl number
p	Pressure, $\text{lb}_f/\text{in.}^2$
\dot{q}	Heat transfer rate, $\text{Btu}/\text{ft}^2\text{-sec}$
R	Gas constant, $\text{ft-lb}_f/\text{lb}_m\text{-}^\circ\text{R}$
Re/ℓ	Reynolds number per unit length
S	Entropy
T	Temperature
TE	Turbine exhaust
t	Time
w	Mass flow rate, lb_m/sec
γ	Ratio of specific heats
δ	Thermal diffusivity, ft^2/sec
ϵ	Emissivity
λ	Dummy integration variable (time units)

ρ	Density, lb_m/ft^3
σ	Stefan-Boltzmann constant 0.1713×10^{-8} , $\text{Btu}/\text{ft}^2\text{-hr-}^\circ\text{R}^4$

SUBSCRIPTS

b	Base
c	Combustor or combustion chamber
FS	Flame shield
m	Mass
w	Wall
∞	Free stream

SECTION I INTRODUCTION

Nearly all rocket-powered vehicles having sustained periods of powered flight have encountered the problem of base heating. While the techniques of using two or more engines on one booster stage and multiple nozzles on one combustion chamber have proved successful as a means of obtaining required thrust and shortening nozzle length, respectively, both have magnified the problem of base heating by the increased complexity of the base flow field. A survey of the main sources of base heating and a discussion of their characteristics are presented in Ref. 1.

Work in the field of base heating was started at the Rocket Test Facility with a series of tests in 1958, using small cold-flow nozzles (Ref. 2). Since that time many experiments have been conducted at the RTF and at other research laboratories to explore the physical laws governing base heating; however, base heating has not yet proved amenable to theoretical prediction. It is necessary, therefore, to obtain base heating data for each missile configuration by scale model testing at trajectory conditions.

This report presents the results of base heating tests conducted with a 5.47-percent-scale model of the Saturn I-Block II in Propulsion Engine Test Cell (T-1) at Mach number 1.16 at 26,600 ft, and at Mach number 1.63 at 38,000-, 40,000-, and 50,000-ft altitudes. The model utilized a short-duration combustor (single chamber with 8 nozzles) developed by the Cornell Aeronautical Laboratory (CAL) to provide the rocket gases (Ref. 3). Charge tubes were used for propellant storage and a fast-acting propellant valve gave rapid start and stop capability to the system. The basic objectives of this test were (1) to evaluate the short-duration technique as applied to base recirculation testing, (2) to compare results obtained with previous long-duration model data, and (3) to compare these data with Block II flight test data. Previous testing was conducted using water-cooled, long-burning (10 to 55 sec), liquid-propellant rockets (Refs. 4 and 5).

The advantages of this short-duration system are (1) single chamber (therefore, all engines have equal pressure), (2) no water cooling required, (3) one control system (for all nozzles) as opposed to one control system per rocket, and (4) capability of many firings during a short time period. The disadvantages of the system are (1) precise timing required for sequencing all systems, (2) special high response instrumentation is required (Refs. 6, 7, and 8), and (3) the short test time may not be sufficient for the flow field to develop fully.

This report presents an evaluation of (1) base and flame shield pressure data and (2) base and flame shield heat transfer data obtained by the short-duration technique using a 5.47-percent-scale Saturn I-Block II model. These data are compared to previous model data and flight test data. Tunnel test conditions were Mach number 1.16, 26,600 ft and Mach number 1.63, 38,000 to 50,000 ft.

SECTION II APPARATUS

2.1 TEST ARTICLE

A model of the Saturn I-Block II (SI-II) afterbody built to a linear scale of 5.47 percent was used as the test article. A comparison of model external shroud contour with the full-scale vehicle is shown in Fig. 1. Simulation of the aft shroud contours was provided from model station 0 forward to model station 14, equivalent to the aft-most 224 in. of the full-scale booster. The portion of the model forward of model station 14 was cylindrical in cross section. The model assembly consisted of the scale model afterbody, a propellant system, combustion chamber assembly, and a turbine exhaust simulation system.

The propellant system (Fig. 2) contained charge tubes, sonic flow-metering venturis, a fast-acting bipropellant automatic valve (autovalve), and a bipropellant injector. The propellants, gaseous oxygen (GO_2) and gaseous ethylene (C_2H_4), were stored under high pressure in separate charge tubes, each 28 ft long, 1.5-in. ID, and 2.5-in. OD. The propellants were heated (to prevent condensation during expansion) with strip heaters, which were mounted on the outside charge-tube walls, and the charge tubes were insulated to retain heat.

The length of the charge tubes and the gas used determined the steady-state test time. After the propellant gas flows were initiated by the autovalve opening, the maximum steady-state test time was governed by the time for the expansion wave to travel from the autovalve to the forward end of the charge tubes and reflect back to the combustor. The expansion time is given in Ref. 9 as $t \approx 2l/a$, where l is the charge-tube length and a is the acoustic velocity of the gas contained by the charge tube. With the 28-ft charge tubes, $t \approx 45$ msec for both oxygen and ethylene. The engine starting transient was approximately 15 msec, resulting in a steady-state test time of approximately 30 msec.

Propellant flow rates were controlled by sonic flow metering venturis (Fig. 3) located near the charge tube-autovalve junction. Flow coefficients

for both venturis were assumed to be 0.99. The venturi contours were established by criteria presented in Ref. 10, and the mass flow versus charge-tube pressure curves were supplied by CAL. Appendix I outlines the method by which the flow curves were determined.

The autovalve (Figs. 4 and 5) consists of two mechanically linked, pneumatically operated piston valves housed in a single body and was located between the charge tubes and the injector. The autovalve had externally mounted strip heaters to help maintain gas temperature. The autovalve opened in 15 msec; closing time was approximately the same.

The injector (Fig. 6) was located at the exit of the autovalve and introduced the gaseous fuel and oxidizer into the combustor. Since the propellants were already in a gaseous state, atomization was not required, and a simple direct-impinging spray pattern was used. Approximately 20 percent of the ethylene flow was injected through film cooling orifices in the combustor extension insert ring, which directed the flow onto the copper combustion chamber extension to reduce wall heating and erosion.

The model used a single brass combustion chamber with an eight exhaust nozzle configuration. Nominal combustor pressures were 500 and 600 psia. The O/F ratios were varied from 2.16 to 2.45. Ignition was accomplished by a single spark plug located in the combustion chamber wall.

The combustion gases were exhausted through eight, scaled, convergent-divergent, rocket nozzles (Fig. 7) constructed of steel and copper. The model engines were clustered with the four inboard engines fixed in a 3-deg outboard cant, and the four outboard engines were fixed at a 6-deg outboard cant from the model centerline. The arrangement was the same as that of the full-scale booster engines when in the null position.

The full-scale propellant pump turbine exhaust gases were simulated by hydrogen gas which was simultaneously discharged through 360-deg exhausters (Figs. 8a and b) located circumferentially about each of the four outboard engines (Figs. 8c and d are schematics of the long-duration and flight exhausters) and from overboard ducts for each of the four inboard engines (Fig. 9). The hydrogen gas was supplied from two manifolds (Fig. 2) having eight outlets; gas metering was accomplished with a 0.0625-in.-diam sonic orifice in each line. The 150-ft-long H₂ supply manifold functioned the same as the propellant charge tubes, providing approximately 70 msec of steady flow.

The quantity of hydrogen gas flow was scaled to provide the heat content of the full-scale missile turbine exhaust gases (Appendix II).

The model external hardware consisted of the instrumented base plate and flame shield, outer engine shrouds with air scoops, base flow deflectors, and aerodynamic fins (Fig. 10). The steel base plate (Fig. 11) and flame shield (Fig. 12) were instrumented with iron-constantan (IC) thermocouples, reference pressure taps, short-duration base pressure gage taps, and heat gages.

2.2 INSTALLATION

The assembled model showing outer engine shrouds with air scoops, flow deflectors, fins, and turbine exhaust ducts is shown in Fig. 13. Testing was conducted in Propulsion Engine Test Cell (T-1), which is a continuous-flow, open-circuit, wind tunnel (Ref. 11). For Mach number 1.63 testing, the test cell was equipped with an axisymmetric, supersonic nozzle (37.5-in. -diam test section) with a centerbody contoured to conform to the stream surface in the flow field necessary to obtain Mach 1.63 (Figs. 13a and b and Ref. 12). Mach 1.16 testing was conducted with the centerbody installed in a perforated 42-in. -diam test section which had a cylindrical approach section and a minimum area throat where the perforated section and the cylindrical section meet (Figs. 13c and d). The model and centerbody are cantilever-mounted from a spider arrangement in the plenum chamber of the test cell and extend aft through the nozzle or cylindrical transonic approach section into the test section. The Mach 1.16 test section exhausted into a 72-in. -diam diffuser, whereas the Mach 1.63 test section expanded into a conical section, then into the 72-in. -diam diffuser.

All model instrumentation lines, electrical control lines, and propellant and turbine exhaust charge tubes were routed through the centerbody and out the support spider into the plenum chamber. All lines except the propellant charge tubes were routed out the plenum chamber through a pressure-tight porthole to the proper facility supply or recording system. The propellant charge tubes extended upstream into the inlet ducting.

2.3 INSTRUMENTATION

Model base heat transfer rates were obtained from thin-film-type resistance thermometers (Refs. 6 and 7). The thin-film resistance thermometer can be represented by a one-dimensional slab of finite thickness mounted on a dissimilar, semi-infinite material. The first

slab functions as a temperature sensor, and the semi-infinite body acts mechanically as a mount for the sensor and thermally as a heat sink. Reference 13 presents a solution of this problem for constant heat transfer to the exposed surface, and Ref. 14 presents a solution for the time dependent case. The gages utilized for these tests were dual-element units (Fig. 14); the front face is utilized to determine total heating rate, and the rear face is utilized to determine radiant heating. The two strips are at right angles to each other to minimize the shadowing of the rear face. The temperature sensing elements were strips of a platinum-alloy, approximately 4μ in. thick, which are deposited on quartz substrate (heat sink) by brushing on a platinum solution and firing the units in a furnace. A thin magnesium fluoride coating is painted over the gage element to provide both mechanical protection of the film and electrical insulation to preclude any possibility of short-circuiting of the film when immersed in an ionized medium. The resulting platinum strips are approximately 0.030 in. wide and 0.25 in. long. Silver tabs are deposited at the terminals of these film strips for lead wire attachment. The change in resistance (of the platinum film) with change in temperature was determined by calibrations furnished by CAL. During any given run the change in resistance is measured, and therefore the temperature of the film or front side of the semi-infinite slab is determined. Initially some of the heat gage outputs were put into an electronic passive differentiator, which converted the ΔT signal of the gage into an output proportional to \dot{q} . This output was displayed on a dual-channel oscilloscope and photographically recorded (see Fig. 15 for a typical trace). During the latter portion of the test, the resistance change of all the thin-film gages was measured by making the gage one leg of a Wheatstone bridge and recording the output of that bridge by an analog-to-digital converter onto magnetic tape (see Fig. 16 for schematic of heat gage circuit). Playback of this tape on a computer gave a digital printout of temperature rise versus time. Heat transfer rates were calculated using a modified semi-infinite solid heat conduction equation (Ref. 15 and Appendix III).

Base pressure measurements were obtained from flush-mounted, shock-mounted self-generating piezoelectric differential transducers having lead-zirconium titanate crystals (Ref. 9 and Fig. 17). During an early portion of this test, short-duration base pressure outputs were put into an analog-to-frequency converter and recorded on magnetic tape. Playback of the tape on a computer gave a digital printout of pressure versus time. During the latter phase of the test, the millivolt outputs of these transducers were recorded on a photographically recording galvanometer-type oscillograph. Each transducer output was fed through high impedance field effect transistors and amplified for recording. Oscillograph galvanometers with frequency response of 600 and 1000 cps were utilized to record base pressure. The galvanometers served a primary purpose of

a data measuring device and a secondary purpose of a high frequency filter. The transistors and the oscillograph were calibrated simultaneously by putting a "step" pressure input at the base pressure orifice and recording each transducer output. Since the transducer/transistor combination does not have dc response, the calibrations were reduced at approximately the same time interval after initiation of the step pressure input as the data were taken after ignition of the combustor. Reference pressures for each base pressure location were measured by mercury manometers referenced to atmosphere. The ΔP obtained from the short-duration pressures was then added to or subtracted from the reference pressure to obtain the absolute base pressure. The short-duration transducers were shock-mounted. Locations of base pressure transducers are shown in Fig. 11b.

Combustor pressure, GO_2 and C_2H_4 injector and venturi pressures, and turbine exhaust manifold pressures were measured by crystal-type transducers with charge amplifiers and recorded on a direct-printing, photographically recording, galvanometer-type oscillograph at a recorder speed of 64 in./sec. Charge-tube and system operating pressures were measured with strain-gage-type transducers and recorded on continuous-inking, null-balance potentiometers.

Charge-tube, turbine exhaust, and base plate temperatures were measured with Chromel®-Alumel® (CA) thermocouples and recorded by continuous-recording or intermittent-recording null-balance potentiometers. Tunnel and diffuser pressures were measured by mercury manometers and photographically recorded.

A summary of model and test cell instrumentation showing the accuracy of the measuring and recording systems is given in Table II.

Selected runs were photographically recorded by a high-speed, motion-picture camera operating at 5000 to 6000 frames/sec. The cameras were mounted at the test section camera port at the exit plane of the engine nozzles.

SECTION III PROCEDURE

Prior to each test period, a new combustor spark plug was installed, and a spark check was made to ensure satisfactory operation during the ignition phase. All other pre-operational procedures were performed to ensure safe and reliable operation of all systems. Pre-fire sea-level calibrations were completed, the test cell pressure was reduced to

2.0 psia, and altitude calibrations were performed. After completion of all calibrations and preoperational procedures, tunnel flow was established.

The tunnel pressure settings were determined from the desired simulated altitude in the test section and from the pressure ratio corresponding to the desired Mach number. For the Mach 1.16 portion of the test, pitot-static probes were used to determine altitude and Mach number. For the Mach 1.63 portion of the test, the test section Mach number was determined from a pre-test total pressure survey; the pressure ratio corresponding to the calibration Mach number was used to determine tunnel operating conditions. Nozzle inlet temperature for all testing was maintained at $100 \pm 3^\circ\text{F}$.

At a pre-selected time prior to initiation of airflow, the charge-tube and propellant valve heaters were turned on to allow the charge-tube gas temperatures and autovalve temperatures to stabilize at 250°F . During this period, propellant charge tubes were pressurized to the desired level. The desired pressure level was dictated by the desired mass flow rates of each gas.

After tunnel flow was established and stabilized and after charge-tube and propellant temperatures stabilized, each heat gage bridge was balanced so that its output was approximately 10 percent of the maximum output which could be recorded (this was done because the gages were extremely sensitive and slight changes in base temperature would cause the gage output to exceed that which could be recorded).

When all procedures and calibrations were completed, the firing was initiated. The sequence of events was as follows:

t-5 sec	Continuous, null-balance recorders - on; analog-to-digital recorder - on
t-2 sec	Oscillographs - on
t-0 sec	Fire switch - on, (fire switch initiates automatic sequencer and timers with the following chain of events) - Timer No. 1 starts
t-0 sec	High-speed cameras - on
t+2800 msec	Timer No. 1 (1) signals autovalve to open (2) signals Timer No. 2 to begin (H_2) (3) signals Timer No. 3 to begin (closing valve)

t+2840 msec	Timer No. 2 signals H ₂ turbine exhaust valve to open.
t+2870 msec	Propellant valve starts to open; opening of valve does the following: (1) triggers a microswitch which is used as time correlation of data - activates a backup propellant valve closing system (2) triggers a second microswitch which closes spark plug circuit and ignites the combustible gases in chamber
t+2885 msec	Autovalue fully open, start of steady-state operation
t+2920 msec	Propellant valve begins to close
t+2935 msec	Propellant valve closed; turbine exhaust valve closed
t+5000 msec	Start switch - off

See Fig. 18 for a typical trace of model sequence of operation and pressures.

All timers utilized for this sequencer were resistance-capacitor network timers and during this test were repeatable to ± 5 msec.

SECTION IV RESULTS AND DISCUSSION

The 5.47-percent-scale model of the Saturn I-Block II afterbody was tested (1) to evaluate the short-duration technique as applied to base recirculation testing, (2) to compare results obtained with previous long-duration model data, and (3) to compare these data with Block II flight test data. Testing was conducted at a simulated altitude of 26,600 ft at Mach number 1.16 and at simulated altitudes of 38,000 to 50,000 ft at Mach number 1.63.

Pressure distribution on the model base and the effects of varying chamber pressure on base pressure and flame shield pressure are discussed. The effects of varying chamber pressure and various O/F ratios on base and flame shield heat transfer are also presented.

4.1 BASE PRESSURE

Typical base pressure oscillograph traces for firings at Mach numbers 1.16 and 1.63 are presented in Fig. 18. Base pressure stabilized at the same time the chamber pressure stabilized (10 to 15 msec after initiation of the combustion event; this is as predicted in Ref. 16). At Mach number 1.16, the base pressures were steady for approximately 25 msec, at which time a tunnel flow disturbance occurred which invalidated further model base data. Testing was also conducted at Mach number 0.8; however tunnel flow stabilization time exceeded the operating time on the short-duration combustor, and, therefore, no valid base pressure or base heat transfer data were obtained at this test condition. The Mach 1.63 base pressure (Fig. 18b) were steady during the entire combustion event (after combustor pressure stabilized) with no tunnel flow disturbance evident. An exception to this occurred at 50,000 ft where a base pressure rise occurred after 25 msec of combustor operation; this disturbance was also observed on the tunnel wall at approximately the same time. Sufficient short-duration transducers were not available to define the cause of this flow disturbance; therefore, an analysis of this disturbance is not possible. It should be noted that the severity of this disturbance increased with increasing combustor pressure. The disturbance also increased in severity when H_2 , simulating the turbine exhaust gas, was flowed. These effects of chamber pressure and turbine exhaust simulation indicate that afterburning may possibly be occurring downstream of the model base causing a back pressure or diffuser pressure rise sufficient to affect nozzle flow.

Typical hot flow base pressure distribution was as shown in Fig. 19. Repeatability of base pressure data for runs at similar operating conditions was well within the measuring accuracy (Table II). Since there was no apparent drastic pressure profile across the base, the arithmetic average of the individual base pressures will be utilized in discussions to follow.

4.1.1 Cold Flow Base Pressure

Average cold flow (engines off) base pressure ratios as a function of Mach number are presented in Fig. 20a. The trend of the base pressure data is one of decreasing base pressure ratio with increasing Mach number. These data are compared with data from Ref. 17, which were obtained at turbulent boundary layer conditions. Reference 17 also notes that, for a constant Mach number, base pressure ratio remains constant when the boundary layer is turbulent. Data presented in Fig. 20b (Mach number 1.63) indicate that the model boundary layer was turbulent since no change in p_b/p_∞ is evident at altitudes from 38,000

to 50,000 ft. Two-dimensional data presented in Fig. 20a (from Ref. 18) indicate the same base pressure ratio trend as the model data but lower in value. Reference 19 presents cold flow axisymmetric base pressure data using Zumwalt's method; cold flow model data in Fig. 20a are in good agreement with these data.

The Mach 1.63 test section extended only one model diameter downstream of the model base; therefore, a test was conducted to determine if variations in the diffuser pressure affected base pressure, since undisturbed supersonic flow must exist to a sufficient distance downstream of the model base to allow the subsonic wake to fully close to keep pressure disturbances from feeding up this subsonic wake. This required distance is a function of model diameter and free-stream Mach number. The downstream diffuser pressure was raised almost 1.8 psi above test conditions utilized for Mach 1.63 testing before any pressure effect was noted on the model base. This type test could not be accomplished at Mach number 1.16 since the test section Mach number and altitude are a function of upstream and downstream pressure and pressure ratio. It should be noted that valid cold flow base pressures are not a necessity for true simulation of base conditions during hot flow since the model wake will be filled by the engine nozzle plume during rocket operation, and therefore, the downstream pressure disturbances will not affect base pressure.

4.1.2 Effects of Altitude and Combustor Pressure on Hot Flow Base Pressure

The effects of altitude are shown for chamber pressures of 500 and 600 psia in Fig. 21a; the effects of H_2 turbine exhaust simulation are also shown. At Mach number 1.63, base pressure ratio increased with increasing altitude. This increase in base pressure ratio was attributed to increasing exhaust plume diameter (Fig. 22), with increasing altitude resulting in increased mass rejection into the base (see Appendix IV for method of calculation of plume shape). Although the base pressure ratio increases, the absolute value of base pressure decreases. Theory (Ref. 18) indicates that base pressure ratio (with no base mass addition) is a function only of Mach number and stream total temperature to base temperature ratio and not a function of ambient pressure; therefore, the trend of increasing pressure ratio with increasing altitude is totally attributed to the effects of the rocket plume geometry change.

It would be expected that for a constant free-stream Mach number, the base pressure ratio (p_b/p_∞) would be equal when the ratio of p_∞/p_c was equal since plume size is a function of this ratio; however, this was not true. This is illustrated by the example outlined in Fig. 23 where for

$p_{\infty}/p_c = 5.0 \times 10^{-3}$, p_b/p_{∞} should be equal at 38,000 and 42,000 ft for $p_c = 600$ and 500 psia, respectively. The base pressure ratio for $p_c = 500$ psia (42,000 ft) was 0.695, whereas for $p_c = 600$ psia (38,000 ft) this ratio was 0.745. Since the base pressure ratios for the two chamber pressures at similar ambient-to-chamber pressure ratios are not similar, this suggests that the mass rejected into the flame shield region from impingement of the four inboard engines is exhausted into the base and has a significant effect on base pressure. The analysis of flame shield pressure is discussed in a later section.

The effect of turbine exhaust simulation on base pressure ratio was an increase in base pressure compared to runs where no H_2 was flowed (Fig. 21a). The rise in pressure ratio was attributed to hydrogen burning in the base region in addition to the mass addition into the base. This pressure rise from hydrogen burning is confirmed by (1) the base heating was higher during the TE simulation than during runs without H_2 and (2) several runs were made with an inert gas (Argon) through the turbine exhaust with no increase in base pressure.

Data obtained with a long-duration model (10- to 55-sec burn time) Saturn I-Block II (Refs. 4 and 5) are shown in Fig. 21 compared with short-duration data. The long-duration Mach number 1.16 data (26,600 ft) were obtained from Ref. 4 with an eight-engine model utilizing LO_2 -RP-1 propellants (see Table I for model characteristics). The Mach number 1.63 (Ref. 5) data were obtained by the author using the same model and technique reported in Ref. 4. The long-duration model is identical in outside dimensions to the short-duration model. As shown in Fig. 21, the long-duration base pressure ratio data at a chamber pressure of 500 psia are significantly higher at all altitudes than the 500-psia short-duration data. Possible reasons for this disagreement are (1) differences in plume shape as a result of change in the isentropic exponent of the long- and short-duration combustion products, (2) difference in engine efficiency, (3) difference in nozzle wall temperature, and (4) unequal engine nozzle mass flow distribution.

The values of the isentropic exponent of the products of combustion (equilibrium flow) for the long- and short-duration model data are given in Table I as 1.25 and 1.15, respectively. The inviscid plume shape for a given value of p_{∞}/p_c and given nozzle is a function of the isentropic exponent, as is the value of the nozzle exit gas properties such as pressure, density, and temperature. As shown in Fig. 22e, the inviscid plume diameter for $\gamma = 1.25$ is smaller than the plume diameter for $\gamma = 1.15$ (all other parameters constant). Therefore, the difference in plume shape is not the reason for the higher base pressure since the larger plume has a lower base pressure.

As shown in Table I, the c^* efficiency of the long-duration engine was approximately 80 percent, whereas the c^* efficiency of the short-duration engine was approaching 100 percent. The total weight flow rate of propellants was 17.84 lb_m/sec for the eight-engine long-duration model, whereas the total weight flow rate for the short-duration model was only 12.5 lb_m/sec. This difference in total propellant weight flow rate gives a corresponding difference in combustion chamber gas density and of exhaust gas density at the nozzle exit. Therefore, if the plume shapes for both techniques were similar, the mass of gas rejected would be greater for the long-duration test. Also, since the long-duration c^* efficiency was low, the rejected partially burned propellants of the long-duration model could react with air in the base regions and burning could occur, with a resulting rise in base pressure. Of the two factors, density and burning, the latter is probably the more significant.

Different nozzle wall temperatures of the short- and long-duration models could have an effect on nozzle boundary layer, base heating, and base pressure. The effect on base heating has been investigated by CAL (Ref. 20) and a significant increase noted when the nozzles were heated. However, no base pressure data were obtained with the heated nozzle and base by CAL.

Data obtained from CAL indicate that individual nozzle exit static pressures are within ± 5 percent of the average of the nozzle exit static pressures. Therefore, the differences ~~are in~~ nozzle flow distribution are probably not the reason for the base pressure difference.

4.1.3 Comparison of Model Data to Flight Test Data

Average base pressure data from flights SA-6 and SA-7, Saturn I-Block II vehicle obtained from Refs. 21 and 22 are presented in Fig. 21b. These data are an average of five base pressure measurements. The relative base location of these pressures is shown in Fig. 11b. Reference 22 indicates that the SA-7 flight trajectory resulted in slightly higher base pressures than had previous SI-Block II flights (SA-5 and SA-6). Therefore, the difference in the SA-6 and SA-7 data indicates a data spread which may be expected from similar flights. The approximate Mach numbers at which these data were obtained are shown over each data point. The trend of the base pressure data of the model and flight test data is in agreement, but the magnitude of the flight test data is higher. The long-duration model data were obtained at a chamber pressure of 500 psia because of rocket engine limitations. Had the long-duration data been obtained at combustion chamber pressure of 600 psia (as was the case with the flight vehicle) and the same percent rise exhibited as with the 500- and 600-psia short-duration data, agreement

would have been much better. Three calculated points are shown in Fig. 21, which assume a rise in base pressure proportional for the 500- and 600-psia long-duration technique and the 500- to 600-psia short-duration technique.

4.1.4 Flame Shield Pressure

Model and flight test flame shield pressure are presented in Fig. 24 (all flame shield pressure data were obtained from the pressure tap location most closely approximating the location of the tap on the flight vehicle). The short-duration model data exhibit a decrease in pressure with increasing altitude; the decrease being very slight from 38,000 to 50,000 ft. Both 500- and 600-psia pressures exhibit the same trend, with the pressure level of the 600-psia data being higher. The long-duration model data are similar in trend to the short-duration data but are higher in magnitude. The flame shield pressure data from flights SA-6 and SA-7 are also presented in Fig. 24. The measured flame shield pressure for the SA-7 test flight became constant at about 32,500 ft, whereas the SA-6 flame shield pressure continued to decrease with increasing altitude up to 48,000 ft, at which time the pressure became constant at approximately 2.7 psia. No reason for this difference in measured flame shield pressure of the two flights was given. The higher flame shield pressure of the SA-7 flight as compared to that of the SA-6 flight is consistent with the trend of the base pressure, SA-7 being higher than SA-6.

Since the gases rejected into the flame shield region are exhausted into the base region and the flame shield pressure is probably strongly influenced by the base region pressure, the flame shield pressure is presented as a ratio to the base pressure in Fig. 25. Once again the long-duration data are in good agreement with flight test data. The short-duration data are significantly lower than either long-duration or flight test data. The three differences which should be most significant are (1) the short-duration and flight test vehicle inboard engines are canted outboard 3 deg from missile centerline; the long-duration model was not canted, (2) the flight vehicle had 600-psia chamber pressure; the long-duration model had only 500, and (3) the isentropic exponent varied as shown in Table I. The differences between the long-duration test and flight vehicle test should be offsetting and not cumulative. The reasoning given for the lack of agreement of short-duration and long-duration base pressure data are applicable here also. In addition, since long-duration base pressures were higher than short-duration base pressures this would result in an effect on flame shield pressure.

4.2 BASE AND FLAME SHIELD HEATING

4.2.1 Short-Duration Base Heating

The total heat transfer distribution on the short-duration model base at chamber pressures of 500 and 600 psia is presented in Fig. 26. Symmetry is assumed about the lines which pass through the outboard engines and the model centerline; these dashed lines are shown in Fig. 26 at 45, 135, 225, and 315 deg. The base is also divided into two basic regions, the inner and the outer regions. The outer region is that base region outside of a circle which passes through the centerline of the outboard engines; the inner region is the region inside this circle with the exception of the area under the flame shield. The location of each calorimeter is shown in Fig. 11c.

Heating on the base was not symmetrical with this model. In both the inner and outer base regions (Fig. 26), the maximum heating occurred in the 135- to 225-deg quadrant of the base. Heating distribution was similar for both the 500- and 600-psia chamber pressure runs, with the higher heating rates occurring during the higher chamber pressure runs. The effects of the H₂ turbine exhaust simulation are more evident with the 600-psia data; the increase in base heating, when compared to no turbine exhaust simulation, is much higher than with the 500-psia tests. The general shape of the heating distribution did not change with the turbine exhaust simulation; however, the heating in the inner region was slightly higher than in the outer region. As previously mentioned, the base pressure increased (for both 500- and 600-psia tests) when H₂ turbine exhaust simulation was utilized. Since it has previously been assumed that the rise in base pressure during tests conducted with H₂ TE simulation as opposed to tests without H₂ was attributed to the burning of the H₂ gas in the base, a higher rise in base heating for the H₂ tests would have been anticipated at 500-psia chamber pressure.

Several tests were run with varying oxidizer-to-fuel ratios. No discernible difference in base heating was evident over an O/F range from 2.16 to 2.44.

Although there was a systematic variation of heating with location as defined by the local heat transfer data, the radiation heating was constant over the base. At Mach number 1.16, the average radiation heating was 1.2 Btu/ft²-sec for the 500- and 600-psia chamber pressure data. At Mach number 1.63 the average radiation was 0.75 Btu/ft²-sec, over the range of altitude and chamber pressure investigated. Hydrogen turbine exhaust simulation had no measurable effect on base radiation heating.

4.2.2 Comparison of Short-Duration to Long-Duration Base Heating

Total heat transfer rates measured on the base of a long-duration Saturn I-Block II model (Refs. 4 and 5) are presented in Fig. 27. However, before a comparison of the heat transfer data of the long-duration to the short-duration data can be made, some discussion of the method of data acquisition is necessary. The heat transfer gage characteristics and method of data reduction for the short-duration data have previously been discussed. Long-duration heat transfer data were obtained by the use of copper slug calorimeters and reduced using the expression

$$\dot{q} = \frac{c_p m}{A} \frac{dT}{dt}$$

No correction was made for radiation or conduction losses. In general, the slug temperature was low enough (200 to 300°F) such that radiation was less than 0.2 Btu/ft²-sec, and the slug installation was designed to hold the conduction losses to a minimum. Data for turbine exhaust simulation and no turbine exhaust simulation were obtained during each test firing by initiating H₂ flow after several seconds of steady-state engine operation. A typical temperature/heat transfer rate time history is shown in Fig. 28. The heat rate indicated by A (in Fig. 28) was defined as the "engines only" heating, whereas the heating indicated by C minus B was defined as heat rate from hydrogen burning, and A + (C - B) was defined as total heating (Ref. 4). For short-duration testing, separate tests were run to obtain turbine exhaust and no turbine exhaust simulation data. This was necessitated by the fact that the 40-msec test time was not sufficient to conduct the test in the same manner as the long-duration. When turbine exhaust flow was simulated (during short-duration testing), the H₂ flow was initiated prior to combustor ignition, which allowed H₂ to flow into the base prior to ignition. Had both tests been conducted in the same manner to determine effects of turbine exhaust, this variable of test method could be eliminated, and therefore correlation of data would be more meaningful.

4.2.3 Comparison of Model Data to Flight Test Base Heating Data

Flight test heat transfer data obtained from Refs. 21 and 22 are presented in Fig. 27. Location of the gages are shown in Fig. 11c. As was the case with the comparison of the two model techniques, the type gage used on the flight vehicle, the method of data reduction, and the difference between tunnel model testing and flight testing must be investigated before any conclusion can be made as to data correlation.

First, one must consider that the flight test data presented in Fig. 27 were obtained at an altitude of 38,000 ft, after approximately 68.5 sec of

powered flight. A typical temperature and heat transfer time history for a flight test gage is presented in Fig. 29. The data presented in Fig. 27 were obtained using a slug-type calorimeter; one data point was obtained from an asymptotic-type gage whose millivolt output is proportional to heat input. The asymptotic gage data were reduced by use of a pre-flight laboratory-radiation calibration such as that mentioned in Ref. 23. The slug heat transfer rates (total and radiation) were reduced by use of the "in-flight calibration" method as outlined in Ref. 24. This "in-flight" method is basically a heat balance performed after main engine cutoff:

$$\dot{q}_{in} = \dot{q}_{stored} + \dot{q}_{out} = \dot{q}_{conduction} + \dot{q}_{radiation}$$

The \dot{q}_{stored} term is readily calculated from

$$\dot{q}_{stored} = \rho C_p \ell \frac{dT}{dt}$$

The radiation loss is evaluated as

$$\dot{q}_{radiation} = \epsilon \sigma F T_w^4. (\epsilon \text{ and } F \text{ assumed} = 1.0)$$

The conduction loss term is evaluated at booster engine cutoff by assuming \dot{q}_{in} equal to zero and solving the heat balance equation. The conduction loss is said to be $K(T_w - T_{initial})$ where K is the loss coefficient.

This method leads to several possible sources of error which must be evaluated prior to comparison to model data. Several of these errors are (1) assumption that the form factor (F) and emissivity (ϵ) are equal to 1.0, (2) effect of difference of reradiation with gage location, and (3) effect of rocket exhaust contamination on measurement of base heat transfer.

If the emissivity and form factor are both assumed equal to 1, any actual value of the two less than 1 will result in excessive estimated values of radiation loss and consequently a lower value for the loss coefficient. Also, conduction losses at engine cutoff will be different from those encountered during the boosted phase since a good portion of the base will be heat soaked by the time engine cutoff occurs. During any given test, the field of view for any given calorimeter may vary as the plume shape increases with increasing altitude. Some gages, such as the flame shield gages and gages located between nozzles, may have no reradiation during the latter portion of the test as the only area these gages see is that of the rocket plume and therefore cannot radiate to this area. The third error, which has just recently been investigated, considers the effect on base heating measurements of rocket exhaust contaminants (Ref. 25). The results of this investigation indicate that

rocket exhaust contaminants deposited on the calorimeter tend to give measured heating rates less than actual. Since this contaminant thickness probably increases with test time, the error will also increase. Contaminants are probably not a problem with the radiation gages if the gaseous nitrogen which is used to purge the gage window of deposits is effective. Although this contaminant deposit is common to all the bases and therefore the results as measured are indicative of the base heating, an analysis of the contaminants must be made prior to comparison to model data.

Examination of the flight test and model data presented in Fig. 27 reveals two significant facts (1) the general level of total heat transfer rate of the model data and the flight data are comparable, whereas there is a marked difference in the measured radiation heat transfer rates for the model and the flight data, and (2) the fact that similarly located gages of the flight test data indicated a marked difference between flights SA-6 and SA-7. Flight data (Refs. 21 and 22) indicate that the primary source of base heating is the radiation of the plumes and that there is convective cooling on the base since the measured total heat transfer rate is less than the measured radiation heat rate. Short-duration model data, on the other hand, indicate that convective heating is the primary source of base heating and that the radiation heating is from 5 to 20 percent of the total. The difference in the base heat transfer data of the two test flights is possibly indicative of the band of data scatter which can be expected.

4.2.4 Flame Shield Heat Transfer

The average heating rates for the long- and short-duration model tests and the flight test flame shield calorimeters are presented in Fig. 30. The total heat transfer data are presented as a function of calorimeter location from the center of the flame shield. When analyzing these data, the differences previously discussed concerning instrumentation, model characteristics, and test technique must still be considered.

All data presented show the trend of decreasing heating with increasing distance from the center of the flame shield. Although the trends of the data are similar, the heating rates for similar test conditions for the different test techniques are not consistent. Good agreement exists between long- and short-duration data at Mach number 1.63 at 38,000 ft, whereas there is a big difference in the data obtained at Mach number 1.16 at 26,600 ft. This disagreement of the data can be better understood by examination of flame shield pressure data (Figs. 24 and 25 and Table I). Based on the measured radiation heating ($0.75 \text{ Btu/ft}^2\text{-sec}$) of the short-duration model at $M = 1.63$, it is

assumed that the heating is primarily convection and not radiation. Since convective heat transfer is basically

$$\dot{q} = h_c (T_g - T_w)$$

the factors which affect these three variables must be examined. The gas temperature or chamber temperature is given in Table I where T_{chamber} (long-duration) is only 62 percent of T_{chamber} (short-duration). Initial wall temperature was 70 to 100°F for both tests. The gas film coefficient is a function of several factors which can be quantitatively analyzed and compared. For a flat plate, the film coefficient is

$$h_c \propto \frac{\ell}{k} c (Re)^a (Pr)^b$$

where

- ℓ = length
- k = thermal conductivity of gas
- a, b, c = constants (value of these determined by type of flow and velocity of flow)
- Re = Reynolds number = $\rho V \ell / \mu$
- Pr = Prandtl number

It is assumed that, for comparison of the flame shield data, all of the above can be assumed constant except Reynolds number which will vary with velocity and density. The velocity of the gas will vary with the ratio of the flame shield pressure to the base pressure, a high ratio corresponding to high velocity. The gas density will vary with composition, temperature, and pressure. The pressure ratios (p_{fs}/p_b) at 26,600 ft for both the long- and short-duration models are equal; therefore, the density and Reynolds number, will vary inversely as the square root of the temperature only, which will result in a lower Re for the short-duration flame shield. The higher heat transfer is therefore attributed to the greater $(T_g - T_w)$ term of the short-duration model. At 38,000 ft, Mach number 1.63, the flame-shield gas density of the short-duration model is much lower than for the long-duration model because of the lower flame shield pressure and higher temperature; the pressure ratio (p_{fs}/p_b) is much lower than for the long-duration model, resulting in lower velocity potential for the short-duration model and the gas temperature of the short-duration model is higher. The first two items would predict lower values of \dot{q} for the short-duration model, whereas the latter would predict a higher value; the results are almost equal values of \dot{q} for both test techniques. The $P_c = 600$ psia short-duration heat transfer values are presented for reference.

The flight test data points obtained at 26,600 and 38,000 ft are presented in Fig. 30. The flight gage located at $x/\ell = 0.275$ is a total heat transfer gage, whereas the other gage is a radiation gage. As was the case with base heat transfer comparisons, the different techniques utilized to acquire the model and flight test data must be thoroughly studied prior to comparison of the flame shield heat transfer data.

Although the short-duration heat transfer and the flight test data were acquired in the same manner as discussed previously, the long-duration data were obtained in a slightly different manner. The raw temperature-time data were reduced by

$$\dot{q} = \frac{mc_p}{A} \frac{dT}{dt}$$

and this \dot{q} value plotted versus the average temperature for that \dot{q} value. This \dot{q}/T curve was then extrapolated linearly to the temperature of the calorimeter prior to the firing.

No attempt is made to correlate the model data to the flight data because of the many differences discussed.

4.3 EVALUATION OF THE SHORT-DURATION BASE HEATING TECHNIQUE

During this series of tests, the short-duration base heating technique was evaluated. The results of this evaluation are:

1. The test duration (≈ 45 msec) is sufficiently long for base pressure adjustment due to the pressure disturbance caused by ignition and burning of the rocket engines. However, base and flame shield pressures obtained during these tests were significantly lower than comparable long-duration model or flight test data.
2. The test duration is sufficiently long for the H_2 gas (used to simulate the turbine exhaust gas) to flow into the base region and ignite.
3. The base total heat transfer rates obtained using the short-duration test technique are in agreement with comparable long-duration and flight test data. It is not known, however, if temperature equilibrium is reached in the base flow region.

Although the absolute values of the base pressure data are lower than flight test data, a relative evaluation of various model configurations (turbine exhaust, flow defectors, scoops, etc.) can easily be obtained by the short-duration technique.

SECTION V

SUMMARY OF RESULTS

A short-duration (45 msec) and a long-duration (10 to 15 sec) 5.47-percent-scale model of the Saturn I-Block II were tested at Mach numbers 1.16 and 1.63 and at altitudes from 26,600 to 50,000 ft. The results of these tests, concerning base pressure and base heating, and an evaluation of the short-duration technique are summarized as follows:

1. The short-duration model base pressure and flame shield pressure were significantly lower than corresponding long-duration model data.
2. At test conditions simulating flight trajectory conditions, the short-duration model base pressure and flame shield pressure were significantly lower than flight test data.
3. Short-duration model test data indicate that the primary source of base heating is convection, whereas flight test data indicate the primary source of heating is radiation.
4. The short-duration technique for base heat testing is an effective tool for a relative evaluation of various model configurations even though the model base pressure data are not in agreement with flight test data.

APPENDIX I SUMMARY OF NON-STEADY FLOW EQUATIONS FOR A SONIC VENTURI

For the one-dimensional, non-steady flows of an ideal gas in a constant area duct, the continuity equation is

$$\frac{1}{\rho} \frac{\partial \rho}{\partial t} + \frac{u}{\rho} \frac{\partial \rho}{\partial x} + \frac{\partial u}{\partial x} = 0 \quad (1)$$

u = velocity in x direction

and the dynamical equation of motion (Newton's second law) is

$$\frac{\partial u}{\partial t} + \frac{\partial u}{\partial x} = - \frac{1}{\rho} \frac{\partial p}{\partial x} \quad (2)$$

for a nonviscous fluid. From the definition of the local speed of sound and the first law of thermodynamics for an isentropic process,

$$2 \frac{da}{a} = \frac{dT}{T} \quad (3)$$

$$\left(\frac{2}{\gamma - 1} \right) \frac{da}{a} = \frac{dp}{p} \quad (4)$$

$$\left(\frac{2\gamma}{\gamma - 1} \right) \frac{da}{a} = \frac{dp}{p} \quad (5)$$

Substitution of Eqs. (3), (4), and (5) into Eqs. (1) and (2) will give

$$\frac{d}{dt} \left(\frac{2}{\gamma - 1} a \pm u \right) = 0 \quad (6)$$

In the Saturn I-Block II flow system, actuation of the automatic valve initiates the propagation of a centered, non-steady expansion wave which proceeds upstream in each of the charge tubes (see Fig. I-1). It follows from Eq. (6) then, that across the expansion,

$$\frac{a_1}{a_2} = 1 + \frac{\gamma - 1}{2} M_2 = \left(\frac{T_1}{T_2} \right)^{\frac{1}{2}} = \left(\frac{p_1}{p_2} \right)^{\frac{\gamma - 1}{2\gamma}} \quad (7)$$

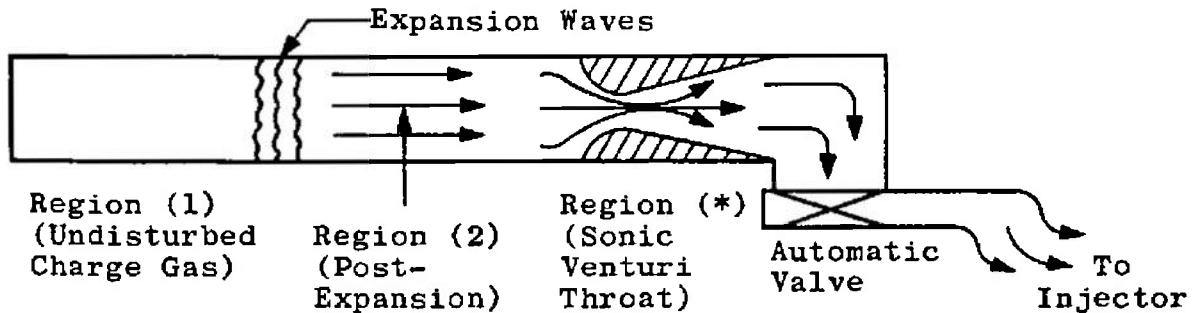


Fig. I-1 Typical Flow Regimes in Charge Tube

For one-dimensional steady flow through a venturi throat, the mass flow rate is given by

$$\dot{w}^* = \rho^* A^* V^* \quad (8)$$

If the flow is isentropic, then $p_t^* = p_{t_2}$, $T_t^* = T_{t_2}$, and Eq. (8) can be transformed into a standard form,

$$\dot{w}^* = \sqrt{\frac{\gamma g}{RT_{t_2} Z_{t_2}}} A^* D^* C_D p_{t_2} \quad (9)$$

where:

$$D^* = \left(\frac{2}{\gamma + 1} \right)^{\frac{\gamma + 1}{2(\gamma - 1)}}$$

at $M = 1.0$

Z_{t_2} = compressibility factor determined by p_{t_2} ,

$T_{t_2} [()_t = \text{total or stagnation conditions}]$

C_D = venturi discharge coefficient

R = gas constant

It should be noted at this point that throughout the development of the equations, an equation of state of the form

$$p = \rho ZRT \quad (10)$$

where Z = compressibility factor

has been assumed. In general, as $Z = Z(p, T)$, development of any flow equation in closed form becomes quite unwieldy. Hence, an investigation of the variation of Z during an isentropic expansion for the present range of interest was carried out for both ethylene and oxygen. This investigation showed Z to be very nearly constant but not necessarily equal to unity. In the equations then, the ratio of the compressibility factors for any two stations in the flow is taken to be 1.0, but the appearance of an individual compressibility factor required the insertion of a specific value (as in Eq. (9)). For convenience, this value is taken to be the value of Z determined from charge conditions. The flow equations may thus be developed in a routine fashion since Eq. (10) may be considered as the equation of state for a "modified ideal gas." Equation (9) can be rewritten as

$$\dot{w} = \sqrt{\frac{\gamma g}{RZ_{CT}}} \sqrt{\left(\frac{1}{T_{CT}} \right) \left(\frac{T_{CT}}{T_{t_2}} \right)} A_{CT} \left(\frac{A^*}{A_{CT}} \right) p_{CT} \left(\frac{p_{t_2}}{p_{CT}} \right) D^* C_D \quad (11)$$

Combining Eq. (7) and the standard isentropic relations for steady flow with Eq. (11) gives:

$$\dot{w} = \frac{A_{CT} P_{CT} C_D}{\sqrt{\frac{\gamma R T_{CT}}{s} Z_{CT}}} \left[\frac{\gamma M_2}{\left(1 + \frac{\gamma - 1}{2} M_2^2\right)^{\frac{\gamma + 1}{\gamma - 1}}} \right] \quad (12)$$

Consideration of thermal imperfections has been carried out through the examination of Eq. (10). Consideration of caloric imperfections requires that the real gas value of the isentropic exponent be examined. From the first law of thermodynamics, for an isentropic process,

$$du = -p dv \quad (13)$$

where u = internal energy

v = volume

The definition of enthalpy and Eq. (13) give

$$dh = v dp \quad (14)$$

or

$$\left. \frac{\partial h}{\partial u} \right|_s = \frac{\rho}{v} \left. \frac{\partial p}{\partial \rho} \right|_s = \left. \frac{\partial \ln p}{\partial \ln \rho} \right|_s \quad (15)$$

By definition,

$$\left. \frac{\partial p}{\partial \rho} \right|_s = a^2$$

An effective isentropic exponent, γ_e , is defined from the relation,

$$a^2 = \frac{\gamma_e p}{\rho} \quad (16)$$

and from Eq. (15),

$$\gamma_e = \left. \frac{\partial \ln p}{\partial \ln \rho} \right|_s \quad (17)$$

Thus, γ_e may be determined from Mollier diagram data and is given by the local slope of $\ln p$ versus $\ln \rho$ along an isentrope, starting from charge conditions. Computation of Eq. (17) for the present region of interest showed straight line variations and hence constant values for the real gas isentropic exponent (although not necessarily the perfect gas value). The γ_e determined by these procedures may then be used directly in the perfect gas relationships developed earlier.

This "Summary of Non-steady Flow Equations for a Sonic Venturi" was furnished by CAL.

APPENDIX II

METHOD OF DETERMINING HYDROGEN FLOW RATE

Gaseous hydrogen was used to simulate the combustible turbine exhaust gases of the full-scale missile. Hydrogen was selected because of its wide flammability limits (9- to 74-percent hydrogen to air, by volume, Ref. 26) and was discharged at a rate which simulated the heat content of the full-scale missile turbine exhaust. Full-scale engine parameters are as follows:

Mass flow rate of turbine exhaust, lb _m /sec/eng	18.6
Heat of combustion in air available, Btu/lb _m	13,500
Temperature of exhaust products, °F	800
γ of turbine exhaust products	1.13

Taking the lower heating value of gaseous hydrogen as 51,600 Btu/lb_m, the model turbine exhaust flow rate,

$$\dot{m} = 18.6 \text{ lb}_m/\text{sec}/\text{eng} \times \frac{13,500 \text{ Btu}/\text{lb}_m}{51,600 \text{ Btu}/\text{lb}_m} \times (0.0547)^2 = 0.0146 \text{ lb}_m/\text{sec}/\text{eng}$$

Turbine exhaust gas momentum and temperature were not simulated.

APPENDIX III METHODS OF CALCULATION

The general methods and equations used to compute the parameters presented in this report are given below:

Heat Transfer Rate

$$\dot{Q}(t)_{\text{gage}} = \left[1 + 0.00033 \Delta T(t) \right] \sqrt{\frac{\pi \rho c_p k}{4t}} \left\{ \Delta T(t) + \frac{1}{\pi} \int_0^t \left[\frac{\sqrt{\lambda} \Delta T(t) - \sqrt{t} \Delta T(\lambda)}{(t - \lambda)^{3/2}} \right] d\lambda \right\}$$

where $\Delta T(t) = \left[1 - \sqrt{(1 - 5.18 \times 10^{-4} \Delta T_{\text{meas}})} \right] / 2.59 \times 10^{-4}$

The equation for $\Delta T(t)$ is an empirical correction to account for the nonlinearity of the sensor resistance with temperature.

$0.00033 \Delta T(t)$ is an empirical correction to match this solution to an exact solution by CAL of the classical nonlinear heat conduction equation with substrate properties given as individual functions of temperature, using numerical techniques and a digital computer. λ is a dummy integration variable with units of time, and the integral is a correction for nonconstant heating rate. The physical properties indicated are those of the substrate evaluated at the engine-off base heat shield temperature. The limiting conditions on the given equation are:

1. Negligible gage Joule heating
2. One-dimensional heat conduction
3. Substrate thickness infinite compared to that of the sensor
4. Thermal conductivity of the sensor is much greater than that of the substrate
5. Test time much greater than sensor characteristic time, l^2/α
6. Gage temperature increasing with time

These conditions were satisfied during this test program.

To obtain actual heating rate values from the measured gage heating rates, the following constants were determined by known-heat-source radiation calibrations and furnished by Chrysler Corporation Space Division (Ref. 27):

$$Q_{\text{rear face gage}} = 0.32 Q_{\text{radiation}}$$

$$\dot{Q}_{\text{convection}} = \dot{Q}_{\text{front face gage}} - 0.43 \dot{Q}_{\text{radiation}}$$

$$\dot{Q}_{\text{total}} = \dot{Q}_{\text{radiation}} + \dot{Q}_{\text{convection}}$$

Mach Number

For Mach number 1.63 testing, the Mach number was determined from a previous supersonic nozzle (total pressure survey) calibration.

For Mach number 1.18 testing, the Mach number was determined from:

$$M = \sqrt{5 \left[\left(\frac{P_{T_{\infty}}}{P_{\infty}} \right)^{\frac{2}{\gamma}} - 1 \right]}$$

APPENDIX IV

DETERMINATION OF JET BOUNDARIES

The actual shape of the engine exhaust jet was determined by using the method of characteristics based on nozzle half angle, exit Mach number, γ , and the ratio p_b/p_c to define the inviscid jet boundary and then applying a viscous correction to this boundary. The viscous correction was accomplished by calculating a mixing layer thickness and superimposing this thickness on the inviscid jet boundary. Since the mixing layer is affected by the boundary layer at the nozzle exit, a calculation of the nozzle exit boundary layer thickness was necessary.

An approximate boundary layer thickness at the nozzle exit was calculated by using the empirical equation,

$$\delta^* = \frac{0.010 (X_{ne})^{0.86} (M_{ne})^{1.25}}{(Re_{ne})^{0.14}}$$

to obtain a value for displacement thickness

where δ^* = Displacement thickness, ft

M_{ne} = Mach number at nozzle exit

Re_{ne} = Reynolds number at nozzle exit

X_{ne} = Distance from the throat to the nozzle exit, ft

Using the tables set up by Tucker (Ref. 28), an approximate nozzle exit boundary layer thickness (δ) of 0.033 in. was obtained, which was considered small enough to ignore as a major influence on mixing layer thickness.

The mixing layer thickness was calculated by referring to the works of Tollmien (Ref. 29), Korst and Tripp (Ref. 30), and Vasiliu (Ref. 31). Tollmien established the incompressible value for spreading rate of a uniform stream mixing with a surrounding ambient gas to be $db/dx_{inc} = 0.255$. A value for db/dx_{comp} was obtained by using the relation for the similarity parameter, σ , proposed by Korst and Tripp in Ref. 30:

$$\sigma_{comp} = \sigma_{inc} + 2.758M$$

where $\sigma_{inc} = 12$

M = Mach number at the initiation of mixing

Because σ , by definition, is inversely proportional to the spreading rate, the following equation was used:

$$\frac{db}{dx_{comp}} = \frac{\sigma_{inc}}{\sigma_{comp}} \cdot \frac{db}{dx_{inc}}$$

giving a value for $db/dx_{comp} = 0.148$. Using the Mach 3.0 value for $\sigma_{inc}/\sigma_{comp}$ proposed by Vasiliu in Ref. 31, a $db/dx_{comp} = 0.077$ was obtained. The value of 0.148 was used because the results predicted, using this value for spreading rate, agreed with the experimental data observed.

Using a spreading rate of 0.148 and introducing s as arc length along the inviscid boundary, the mixing layer thickness was calculated with the equation

$$b = 0.148$$

where

b = Mixing layer thickness

s = Arc length

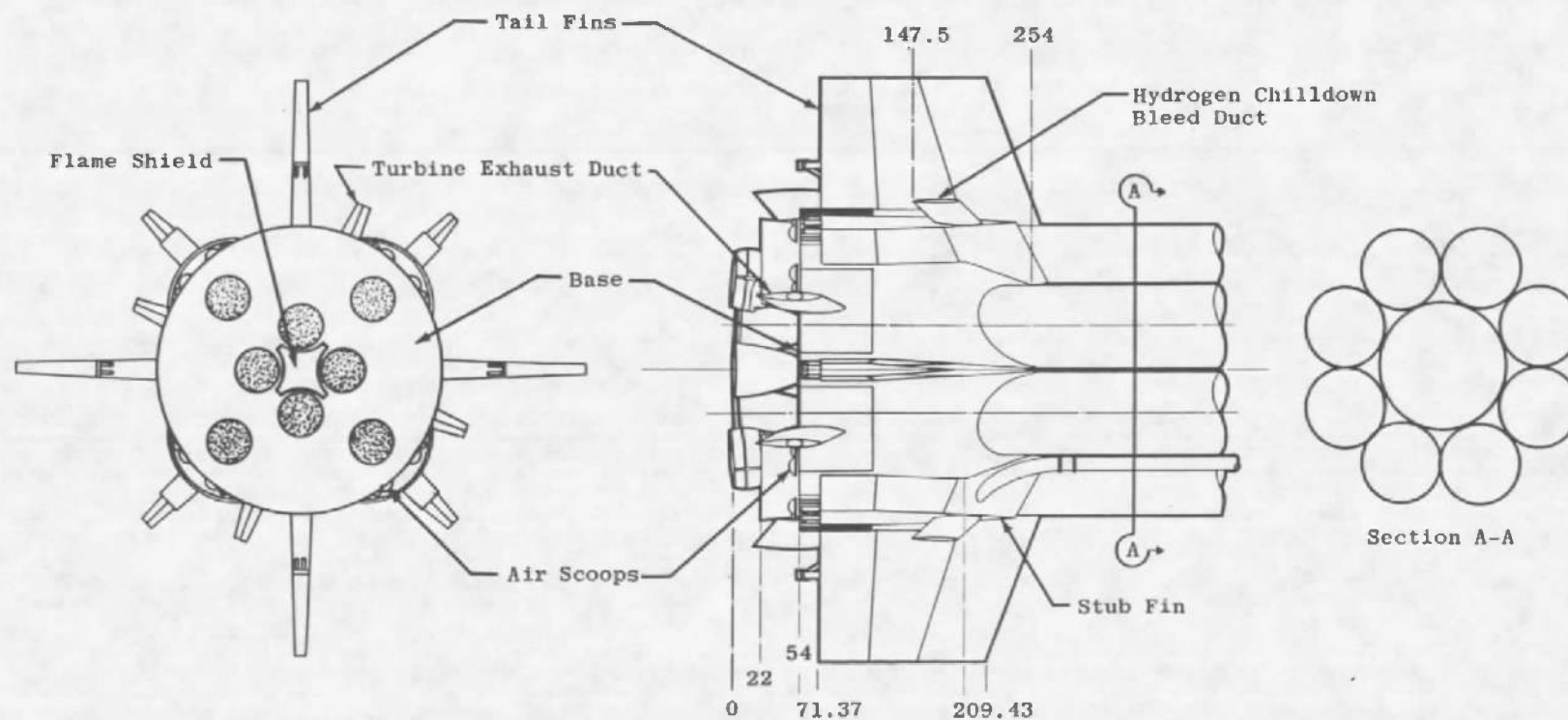
The resulting values for b were superimposed perpendicular to the inviscid jet boundary and located by an arbitrary fraction, θ , where the θ part of b was outside the inviscid jet (Fig. 24a). This was based on the premise that the spreading would propagate to both sides of the inviscid boundary. In the case of jets with equal temperatures and pressures, a θ of 0.5 is used. Work done by Korst and associates (Ref. 30) indicates that a temperature and pressure unbalance will shift the midpoint of the velocity profile toward the low energy side, resulting in a θ of approximately 0.6 to 0.7. An arbitrary value of 0.6 was used for θ in this case to give a conservative estimate of jet intersection.

REFERENCES

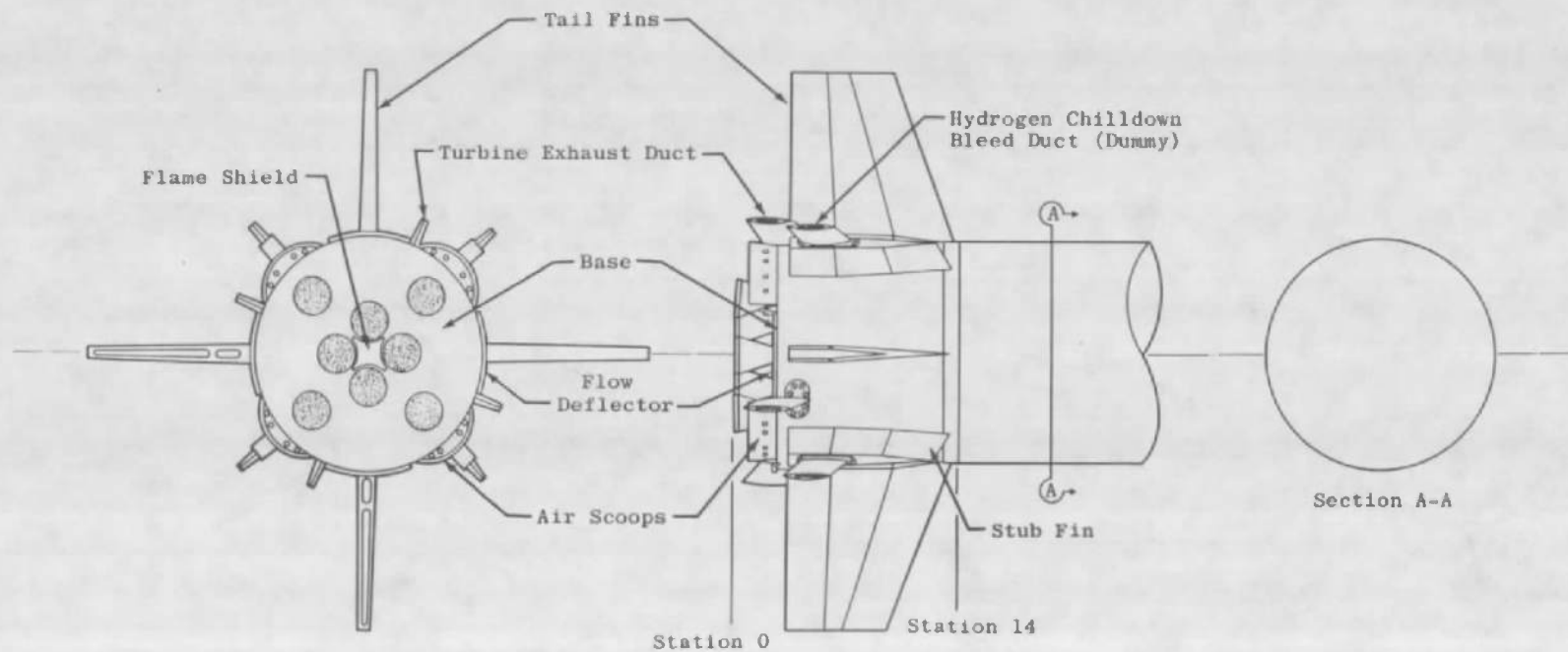
1. Goethert, B. H. "Base Heating Problems of Missiles and Space Vehicles." ARS Paper 1666-61, March 13-16, 1961.
2. Goethert, B. H. and Barnes, L. T. "Some Studies of the Flow Pattern at the Base of Missiles with Rocket Exhaust Jets." AEDC-TR-58-12 (AD302082)(Revised), June 1960.
3. Sergeant, R. J. "The Application of Short-Duration Techniques to the Experimental Study of Base Heating." Cornell Aeronautical Laboratory, Inc., Report No. HM-1510-Y-1 (II), April 1965.
4. Parker, J. R. "An Investigation of Base Heating on a 5.47-percent Scale Model Saturn SA-5 Booster Afterbody at Mach Numbers 0.8 and 1.2 and Typical Trajectory Altitudes." AEDC-TDR-62-62 (AD274714), April 1962.
5. Data obtained by the author on a 5.47-percent-scale model of the Saturn I-Block II at Mach Number 1.63. The technique and model are the same as reported in Ref. 4.
6. Bogdan, Leonard. "High-Temperature, Thin-Film, Resistance Thermometers for Heat Transfer Measurement." Cornell Aeronautical Laboratory, Inc., Report No. HM-1510-Y-5, February 1963.
7. Bogdan, Leonard. "Measurement of Radiative Heat Transfer with Thin-Film Resistance Thermometer." Cornell Aeronautical Laboratory, Inc., Report No. HM-1510-Y-9, July 1963.
8. Martin, James F., Duryea, George R., and Stevenson, Leroy M. "Instrumentation for Force and Pressure Measurements in a Hypersonic Shock Tunnel." Cornell Aeronautical Laboratory, Inc., Report No. 113, January 1962.
9. Matthis, C., Muench, R., and Richard, W. "The Design and Development of a Short-Duration Constant Pressure Combustor for Use in Rocket Base Heating Investigations." Cornell Aeronautical Laboratory, Inc., Report No. HM-1510-Y-2, December 1962.
10. Smith, Robert E., Jr. and Matz, Roy J. "Verification of a Theoretical Method of Determining Discharge Coefficients for Venturis Operating at Critical Flow Conditions." AEDC-TR-61-8 (AD263714), September 1961.

11. Test Facilities Handbook (5th Edition). "Rocket Test Facility, Vol. 2." Arnold Engineering Development Center, July 1963.
12. Peters, C. E. "Annular Nozzles for Missile Base Flow Testing." AEDC-TN-60-62 (AD 236195), May 1960.
13. Carslaw, H. S. and Jaeger, J. C. Conduction of Heat in Solids. Oxford at the Clarendon Press, London, 1950.
14. Vidal, R. J. "Model Instrumentation Techniques for Heat Transfer and Force Measurements in a Hypersonic Shock Tunnel." Cornell Aeronautical Laboratory, Inc., Report No. AD-917-A-1, February 1956.
15. Reiner, A. M. "Reduction of Thin Film Resistance Thermometer Temperature Histories to Heating Rates." Chrysler Corporation Space Division Report No. TN-AE-64-48, December 1964.
16. Ihrig, H. K., Jr. and Korst, H. H. "Quasi-Steady Aspects of the Adjustment of Separated Flow Regions to Transient External Flows." AIAA Journal, Vol. I, No. 4, April 1963.
17. Kurzweg, H. H. "Interrelationship between Boundary Layer and Base Pressure." Presented at Nineteenth Annual Meeting IAS, New York, January 29 - February 1, 1951.
18. Dixon, R. J. and Page, R. H. "Design Charts and Analysis for Heat Transfer and other Parameters in a Two-Dimensional Separated Flow." The Boeing Co. Document No. D2-12765, January 1963.
19. Lee, C. C. and Floyd, J. G. "Computation of Axisymmetric Base Pressure by Zumwalt's Method." Brown Engineering Co., Huntsville, Ala. NASA CR-67108, June 1965.
20. Sergeant, R. J. "The Application of Short-Duration Techniques to the Experimental Study of Base Heating, Part II: A Study of Reynold's Number and Temperature Effects on Base Heating for a Four-Engine Hot Rocket Configuration Operation at High Altitude." Cornell Aeronautical Laboratory, Inc., Buffalo, N. Y., April 1965.
21. Hartley, L. L. and Wolsefer, A. W. "Flight Evaluation of Saturn SA-6 SI Stage Base and Aerodynamic Heating Data." Chrysler Corporation Space Division, TN-AE-64-54, July 1964.
22. Tucker, J. P., et al. "Flight Evaluation of Saturn SA-7, S-I Stage Base and Aerodynamic Heating Data." Chrysler Corporation Space Division TN-AE-64-64, December 1964.

23. Rall, Dieter L. and Stempel, Fred C. "A Discussion of the Standardized Procedure for Calibrating Heat Flux Transducers." 19th Annual Instrument Society of America Conference, New York, October 12-15, 1964.
24. Geraghty, J. "IBM 7094 Base Heating Program for Reducing Temperature Histories to Heating Rates." Chrysler Corporation Space Division TN-AE-64-19, January 3, 1964.
25. Wehofer, S. "Rocket Exhaust Contaminants and Base Heating Tests." AEDC-TR-65-191 (AD472626), October 1965.
26. Drell, Isadore L. and Belles, Frank E. "Survey of Hydrogen Combustion Properties." NACA Report 1383, 1958.
27. Davis, G. L. "Calibration of Thin-Film Resistance Thermometers for Absorptivity Coefficient." Chrysler Corporation Space Division Report No. TN-AE-65-113, December 1965.
28. Tucker, Maurice. "Approximate Calculation of Turbulent Boundary-Layer Development in Compressible Flow." NASA TN 2337, April 1951.
29. Tollmien, Walter, "Calculation of Turbulent Expansion Process." NACA TM 1055, September 1945.
30. Korst, H. H. and Tripp, W. "The Pressure on a Blunt Trailing Edge Separating Two Supersonic, Two-Dimensional Air Streams of Different Mach Numbers and Stagnation Pressures but Identical Stagnation Temperatures." Proceedings of the Fifth Midwestern Conference on Fluid Mechanics, 1957.
31. Vasiliu, J. "Turbulent Mixing of a Rocket Exhaust Jet with a Supersonic Stream Including Chemical Reactions." Journal of the Aerospace Sciences, Vol. 29, No. 1, January 1962, pp. 19.
32. Zeleznik, Frank J. and Gordon, Sanford. "A General IBM 704 or 7090 Computer Program for Computation of Chemical Equilibrium Composition, Rocket Performance, and Chapman-Jouguet Detonations." NASA TN-D-1454, Lewis Research Center, Cleveland, Ohio, October 1962.



a. Full-Scale Booster Afterbody
 Fig. 1 Comparison of Model with Full-Scale S1-Block II Booster Afterbody



b. 5.47-Percent Scale Model Afterbody
Fig. 1 Concluded

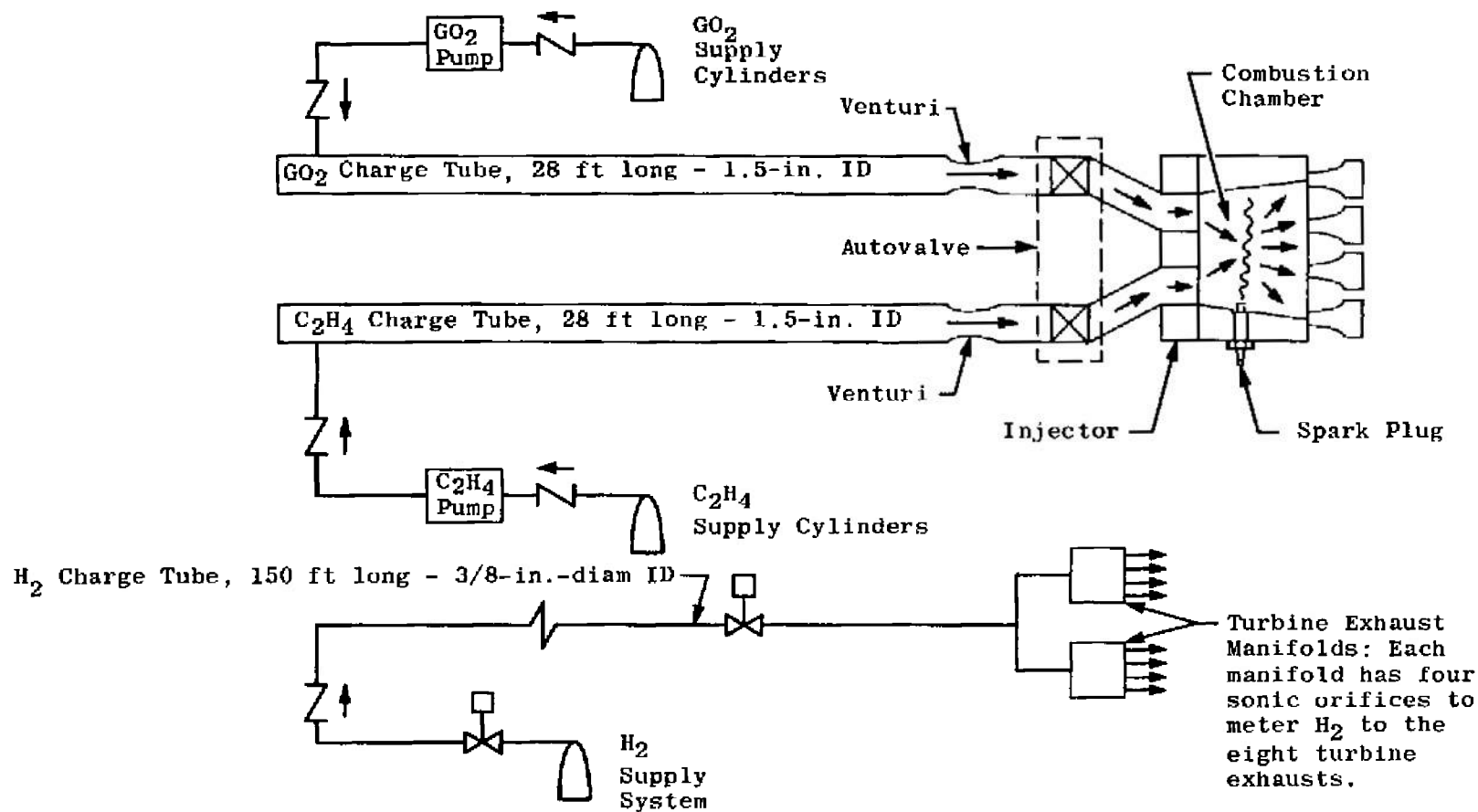
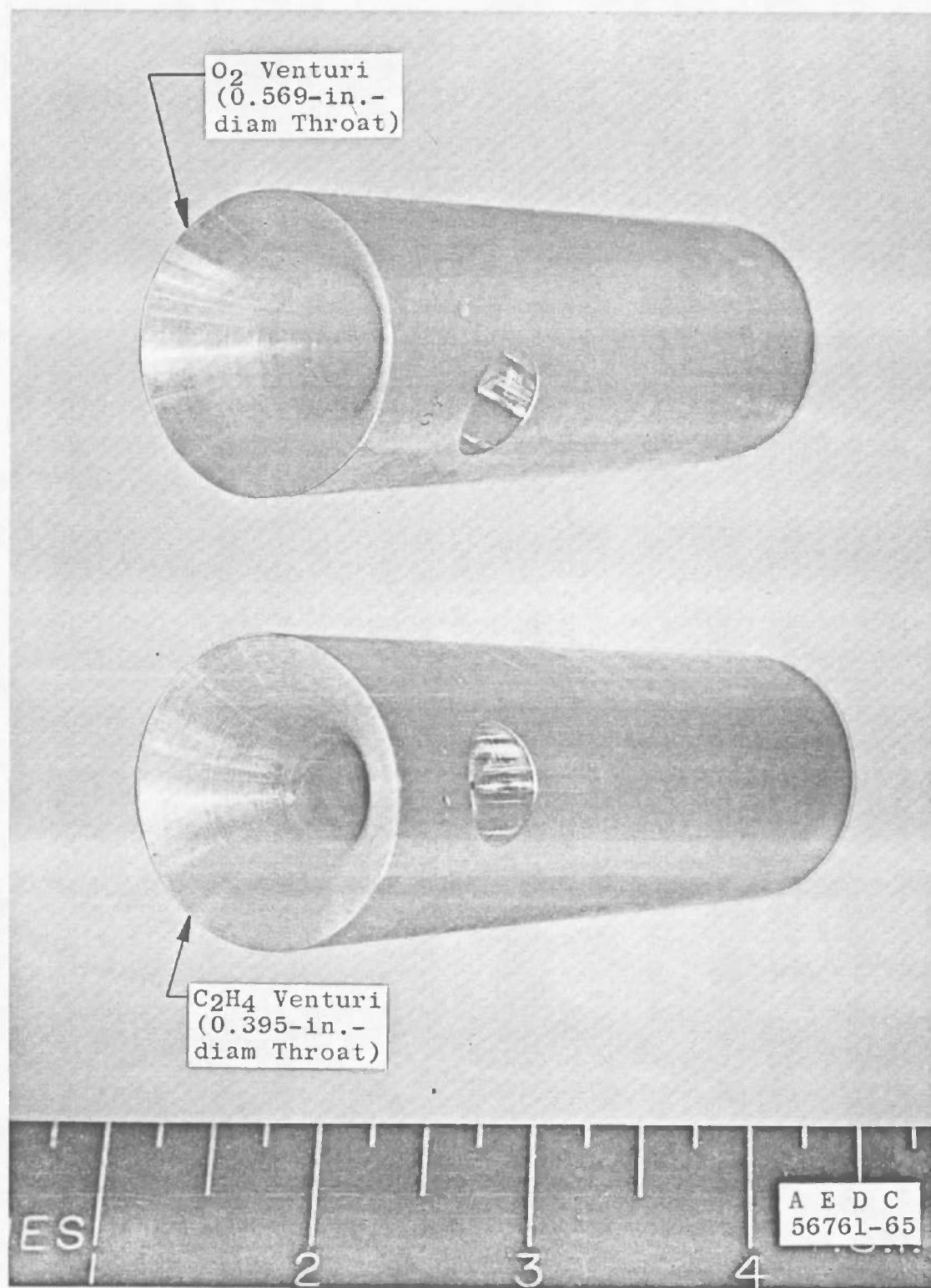
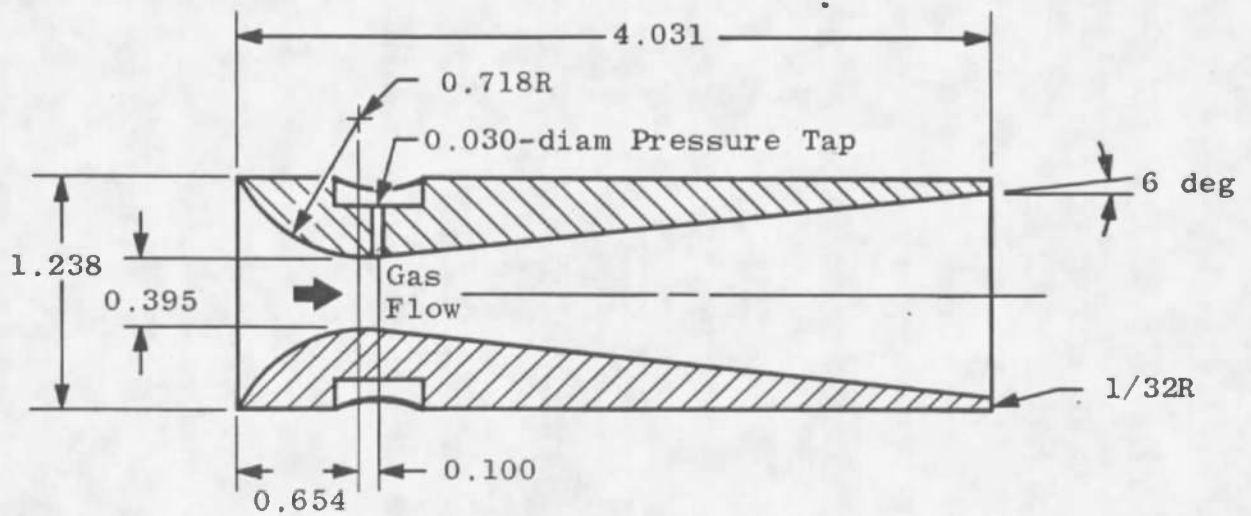


Fig. 2 Schematic of Short-Duration Propellant System

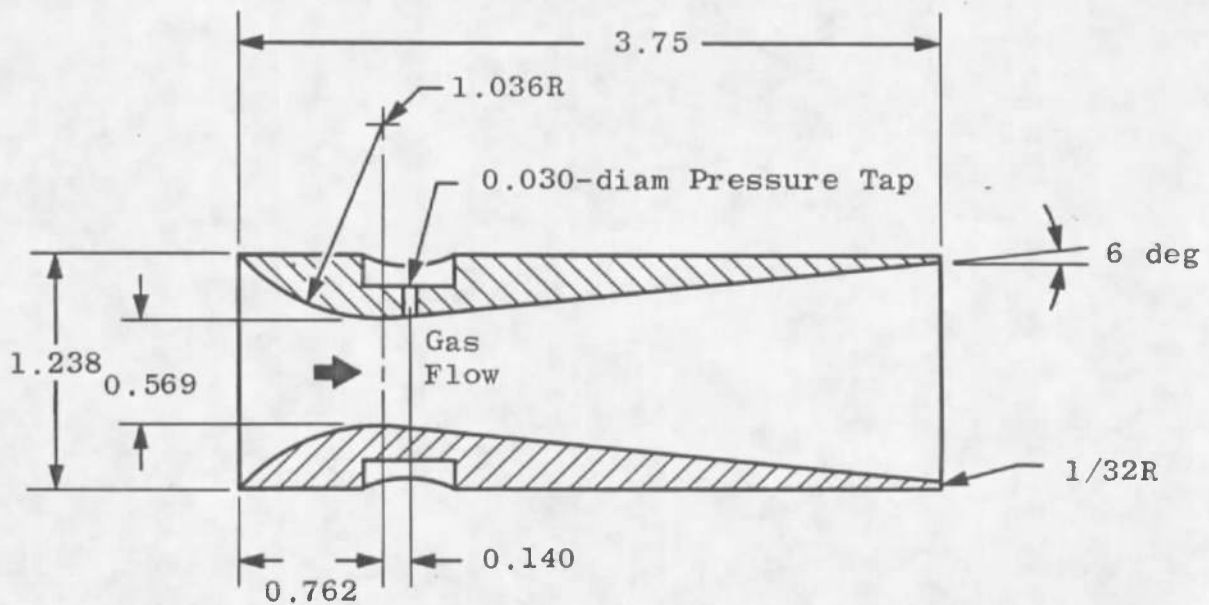


a. Photograph
Fig. 3 Charge Tube Venturis



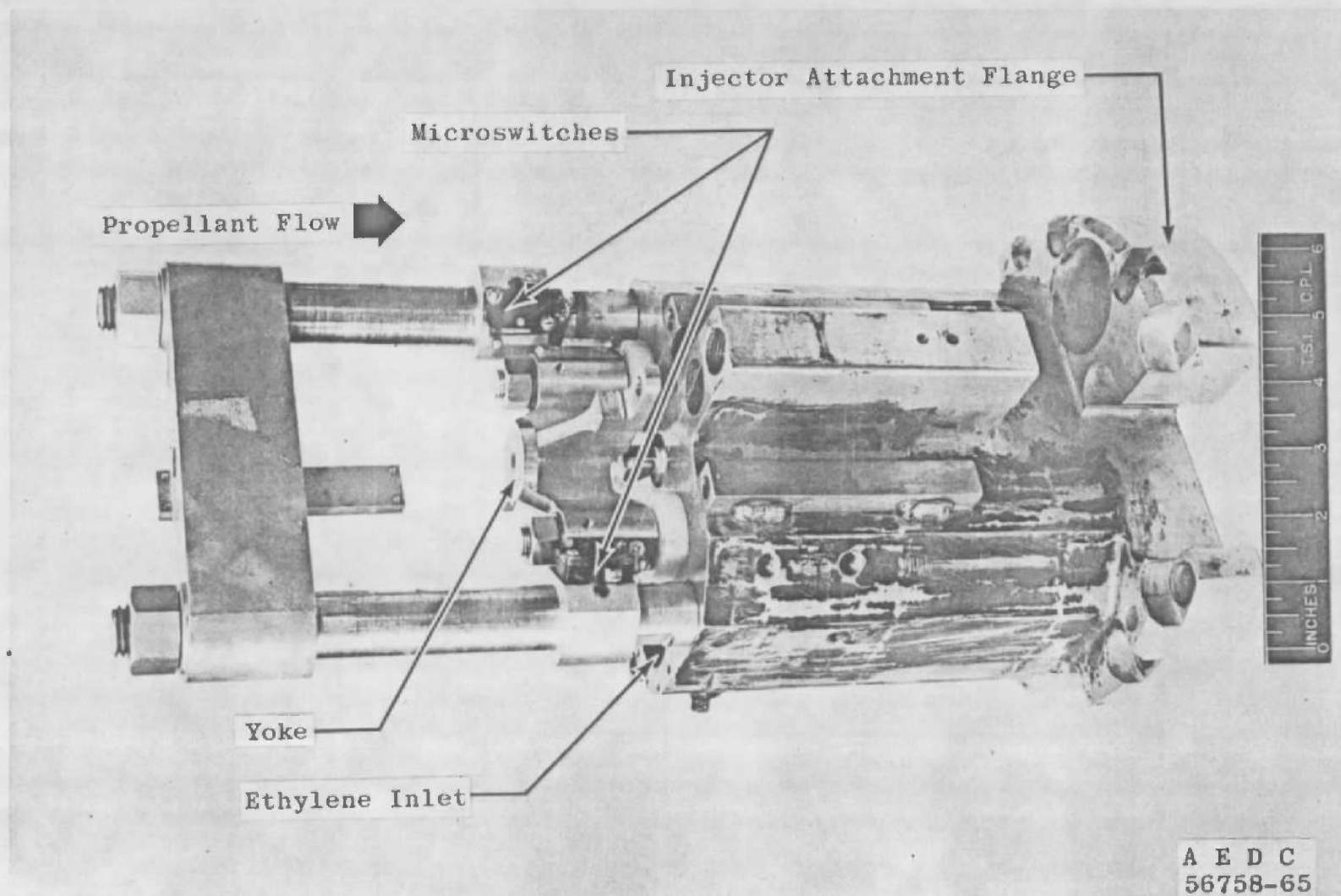
Ethylene Venturi

1. All Dimensions in Inches
2. Material, Brass

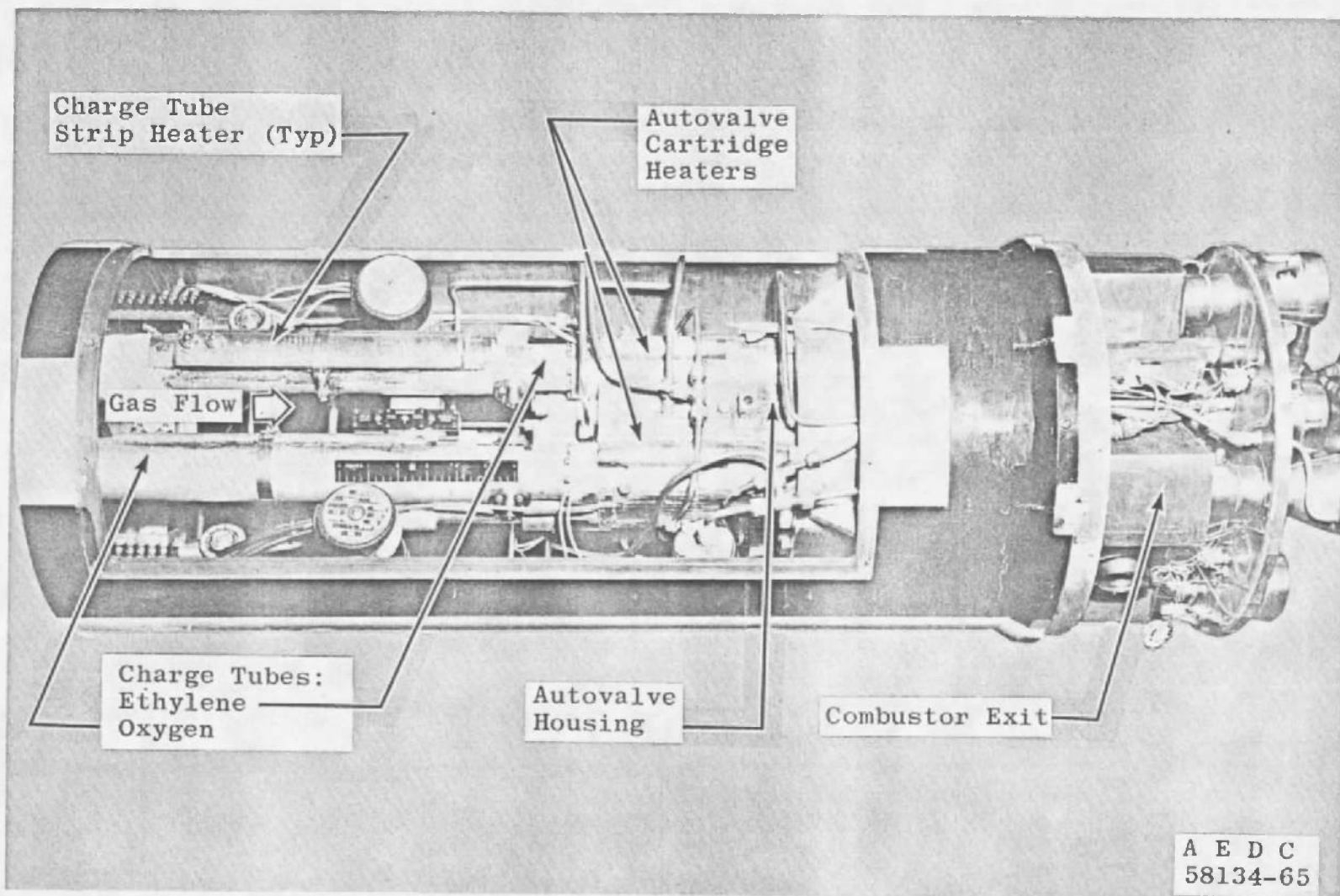


Oxygen Venturi

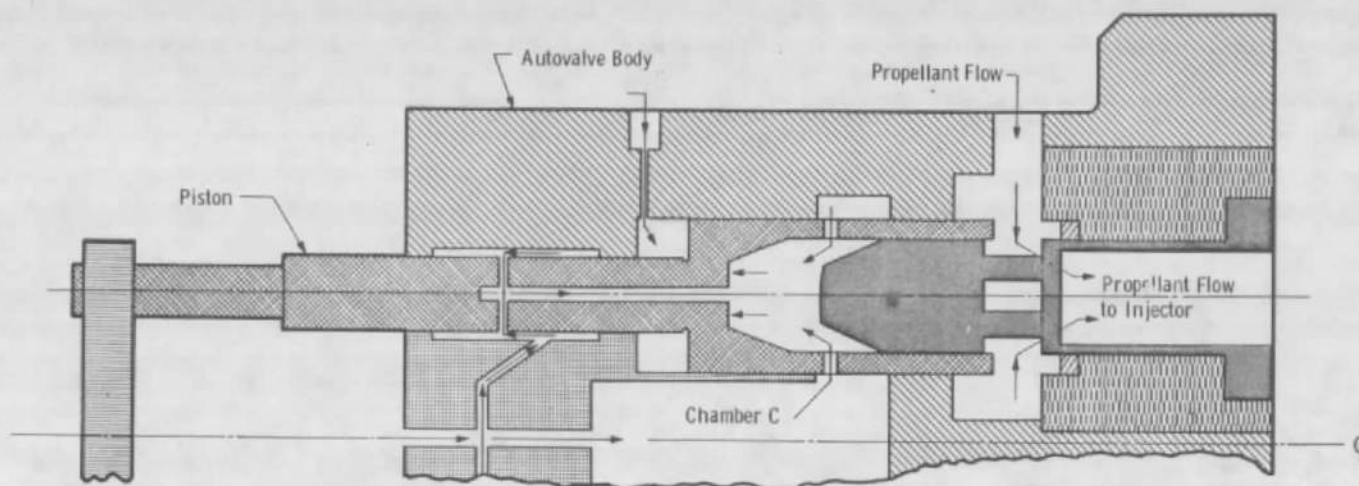
b. Schematic
Fig. 3 Concluded



a. Photograph
Fig. 4 Autovalve

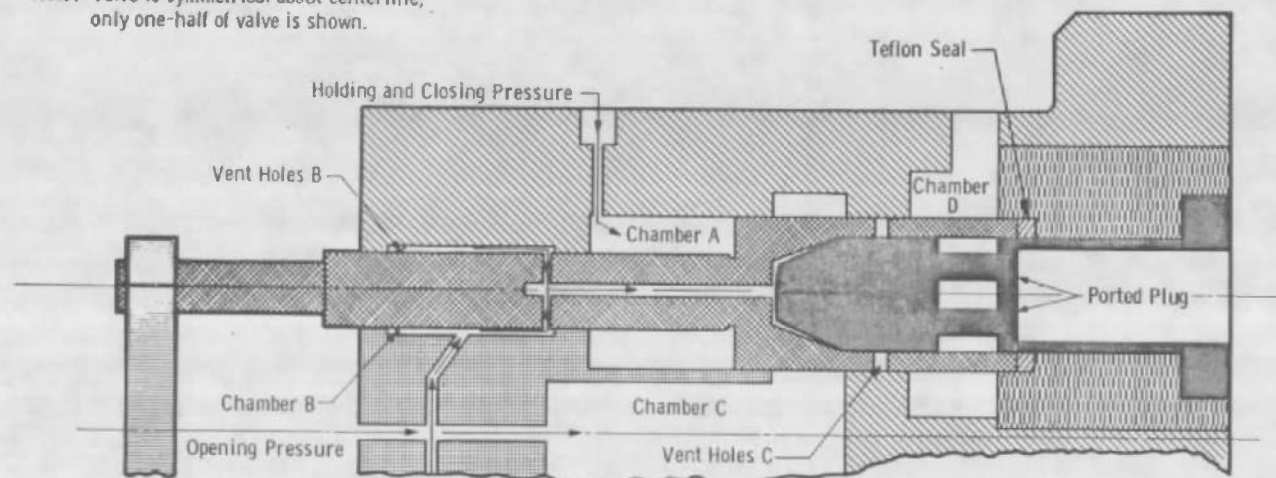


b. Installation Photograph
Fig. 4 Concluded



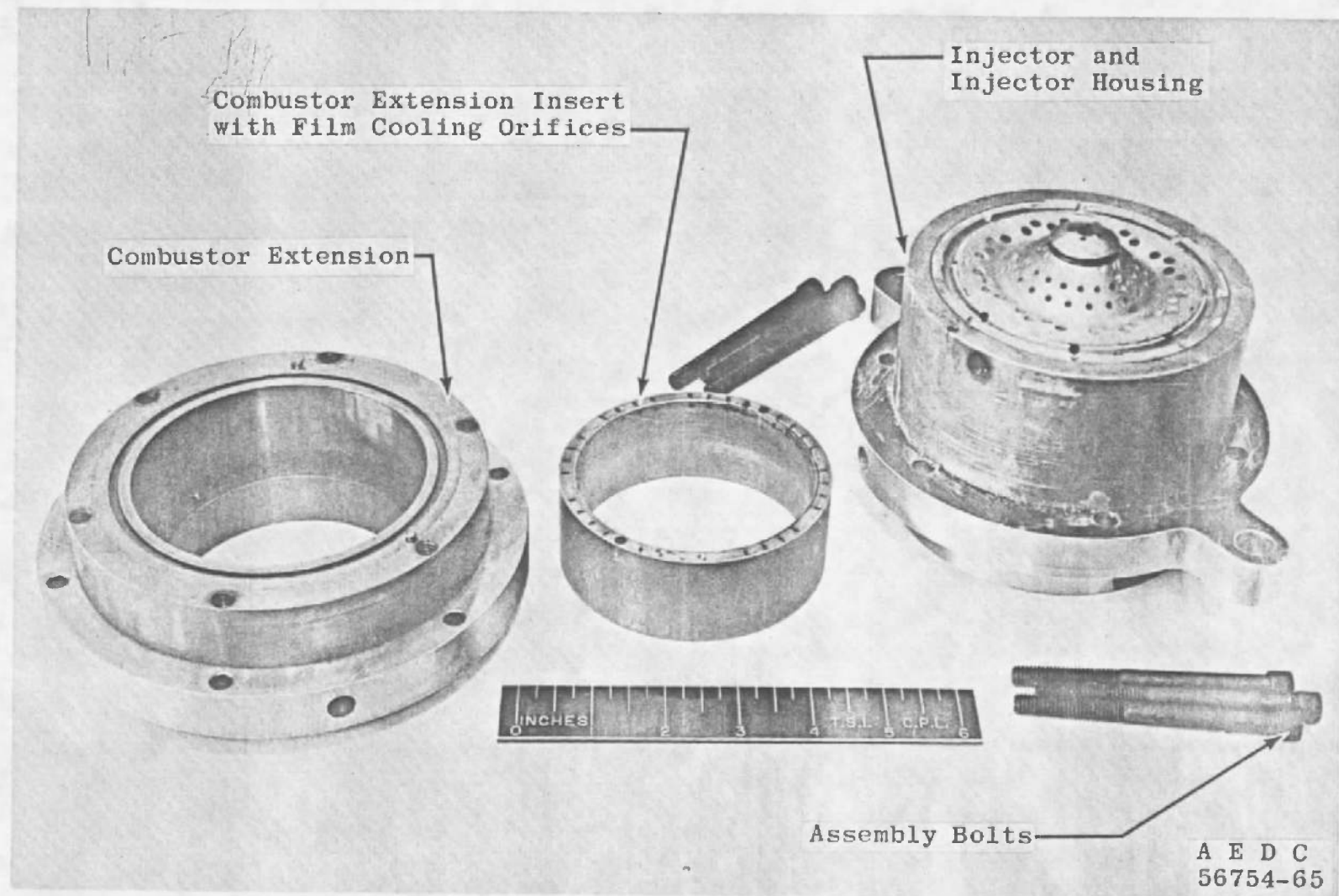
a. Open Position

Note: Valve is symmetrical about centerline;
only one-half of valve is shown.

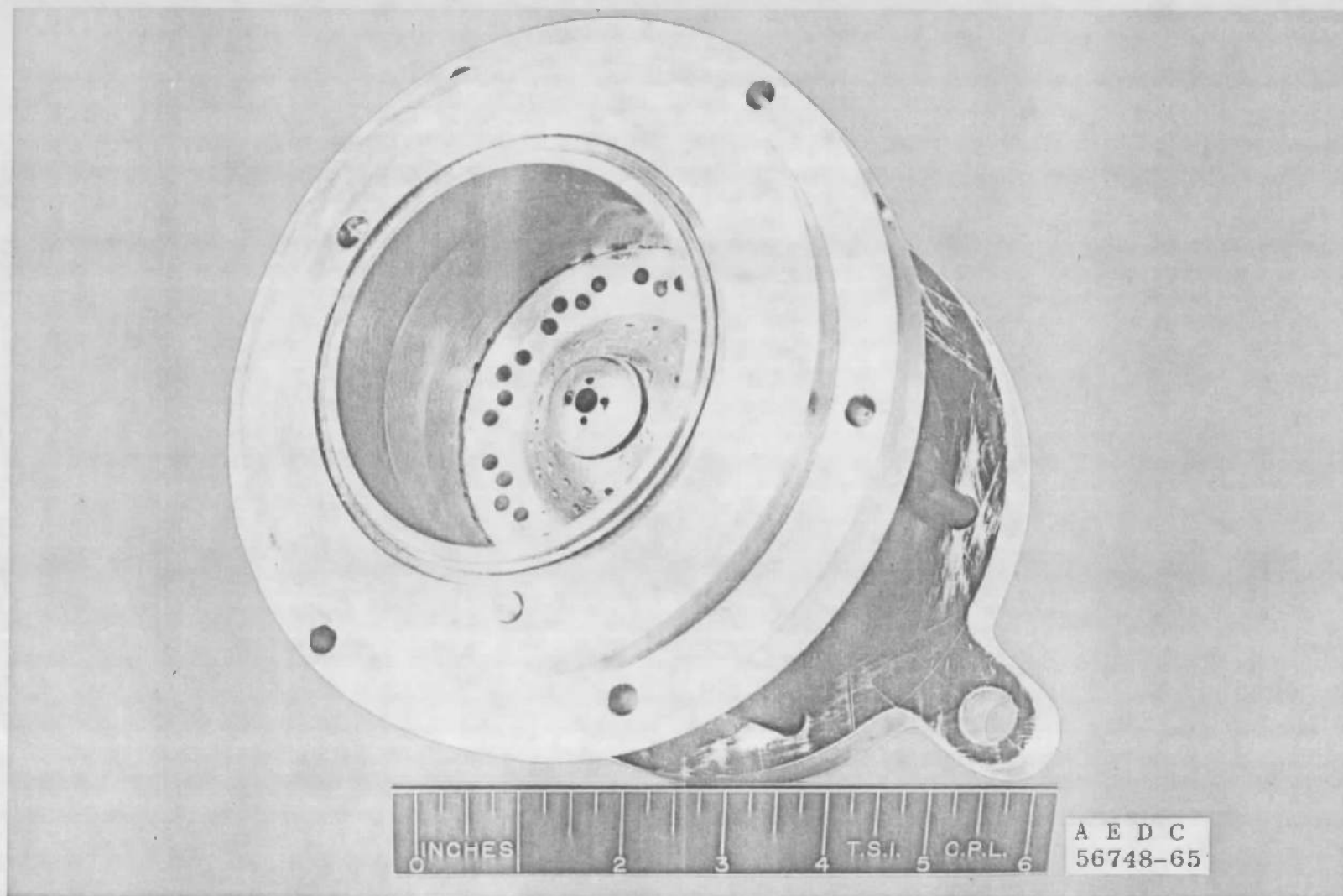


b. Closed Position

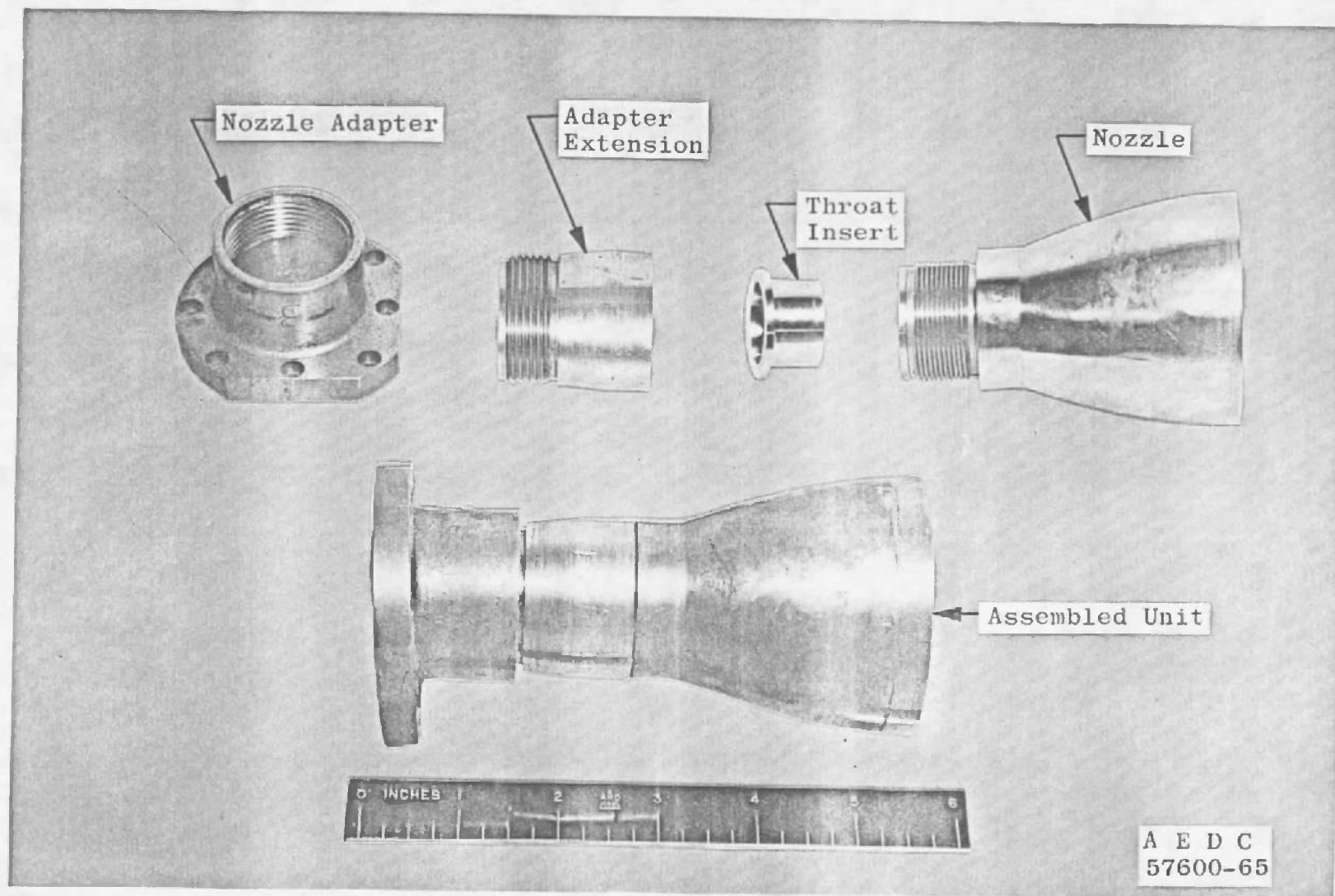
Fig. 5 Autovalve Schematic



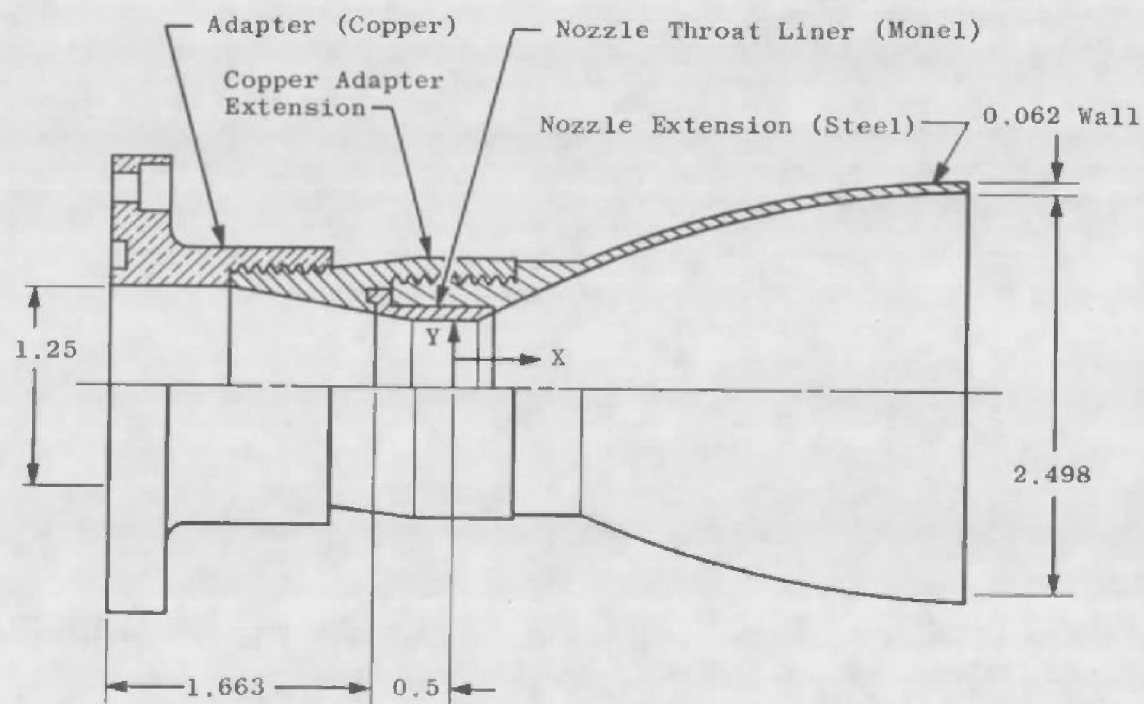
a. Components
Fig. 6 Propellant Injector



b. Assembly
Fig. 6 Concluded

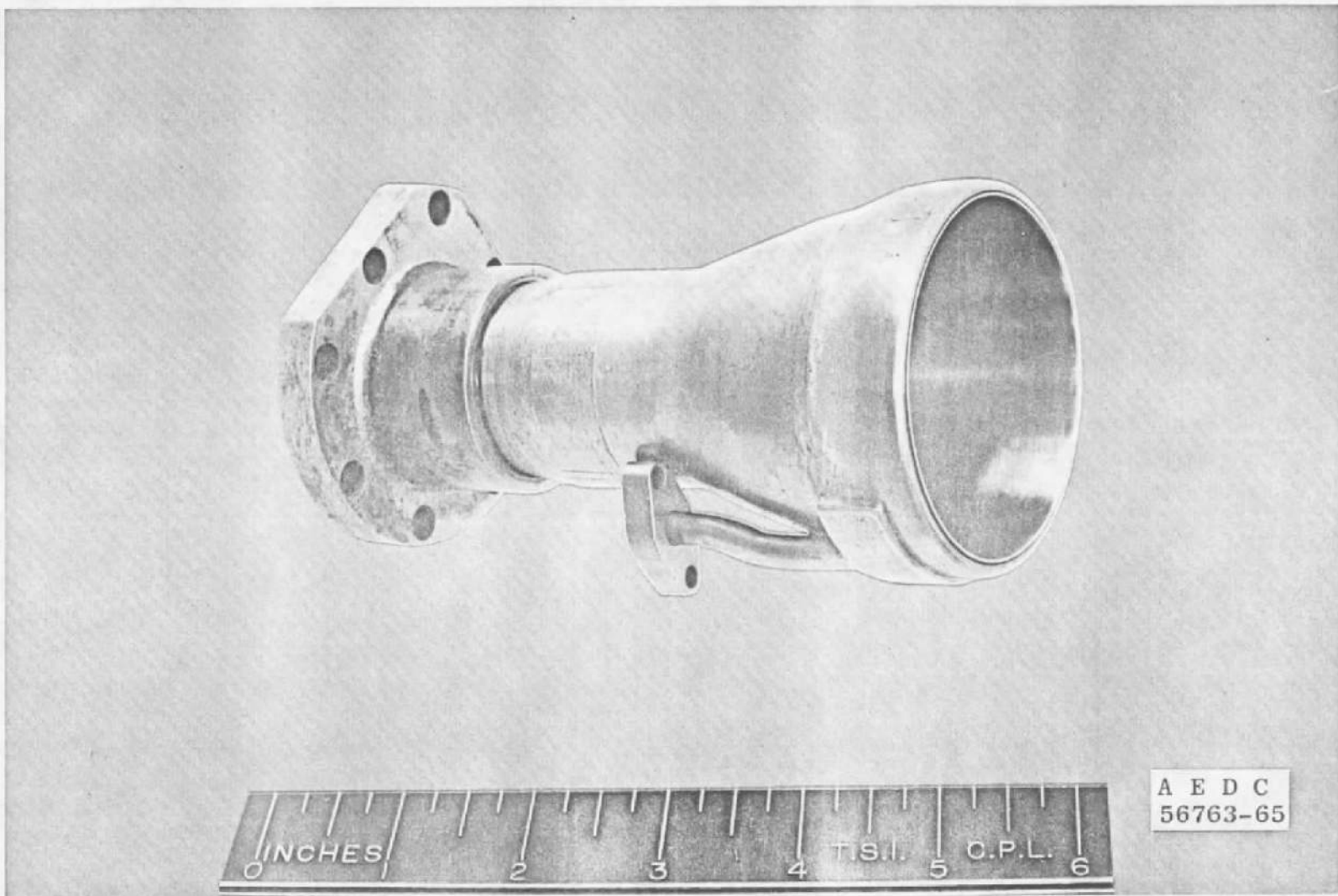


a. Photograph
Fig. 7 Model Exhaust Nozzle

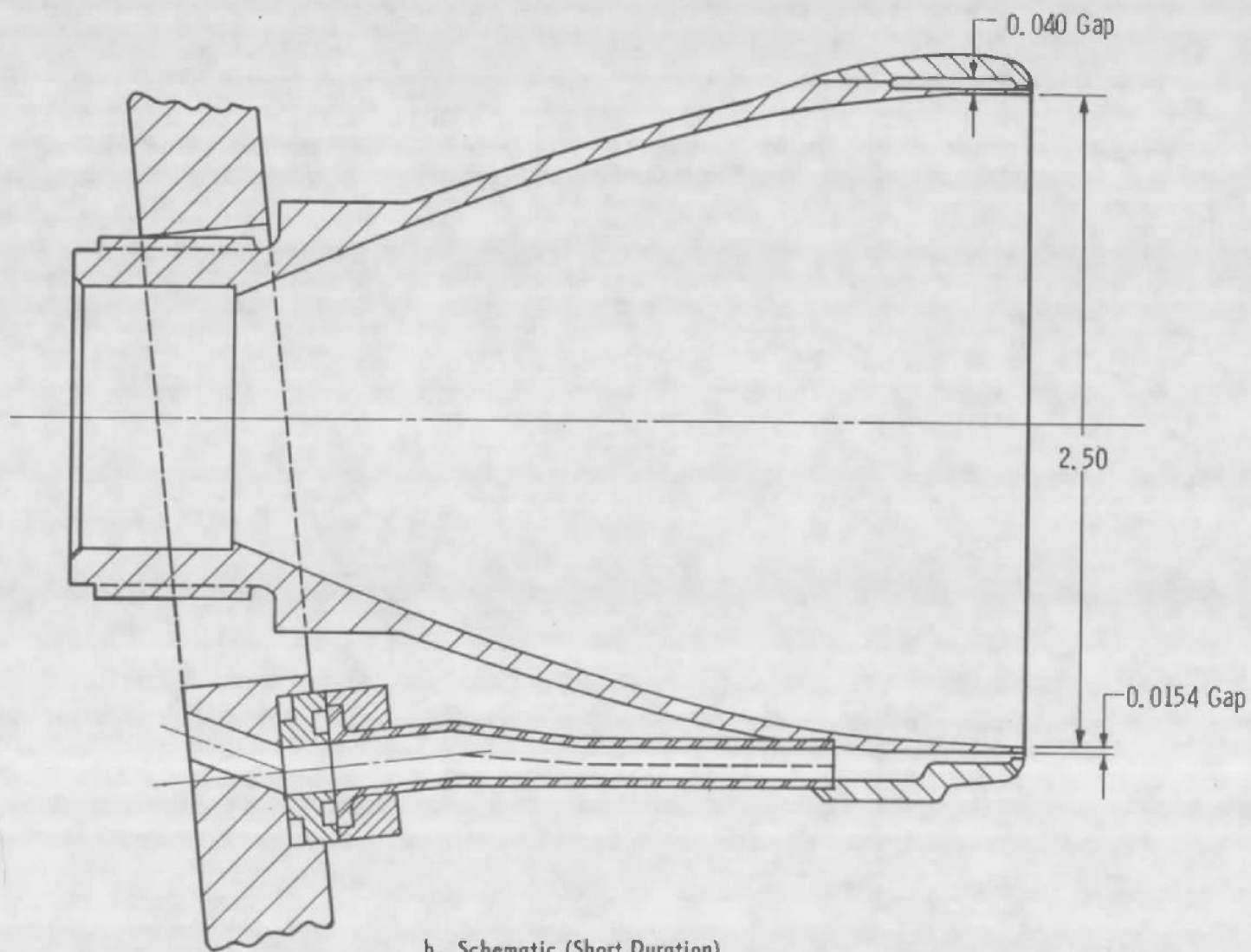


<u>X, in.</u>	<u>Y, in.</u>
0	0.442
0.073	0.456
0.202	0.508
0.448	0.608
0.694	0.706
0.972	0.814
1.1227	0.907
1.447	0.977
1.771	1.066
2.027	1.125
2.242	1.168
2.458	1.205
2.633	1.225
2.808	1.238
2.961	1.247

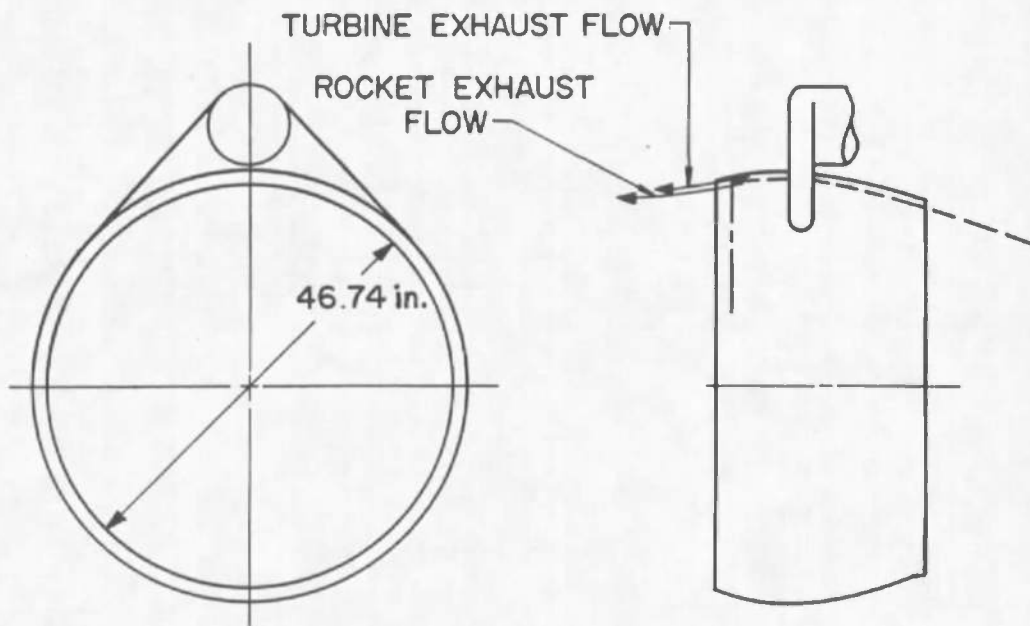
b. Schematic
Fig. 7 Concluded



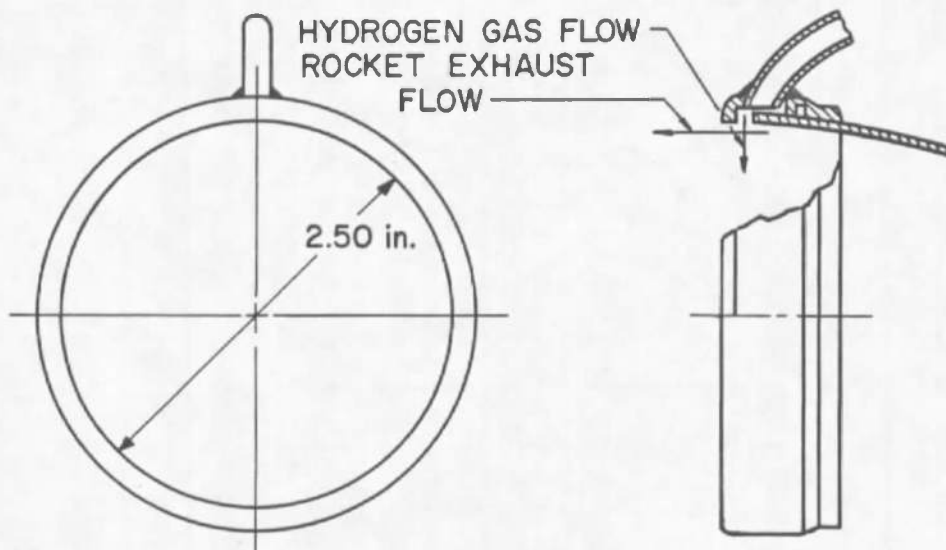
a. Photograph (Short Duration)
Fig. 8 Outboard Nozzle with 360-deg Exhausterator



b. Schematic (Short Duration)
Fig. 8 Continued



c. Schematic (Full Scale)



d. Schematic (Long Duration)
Fig. 8 Concluded

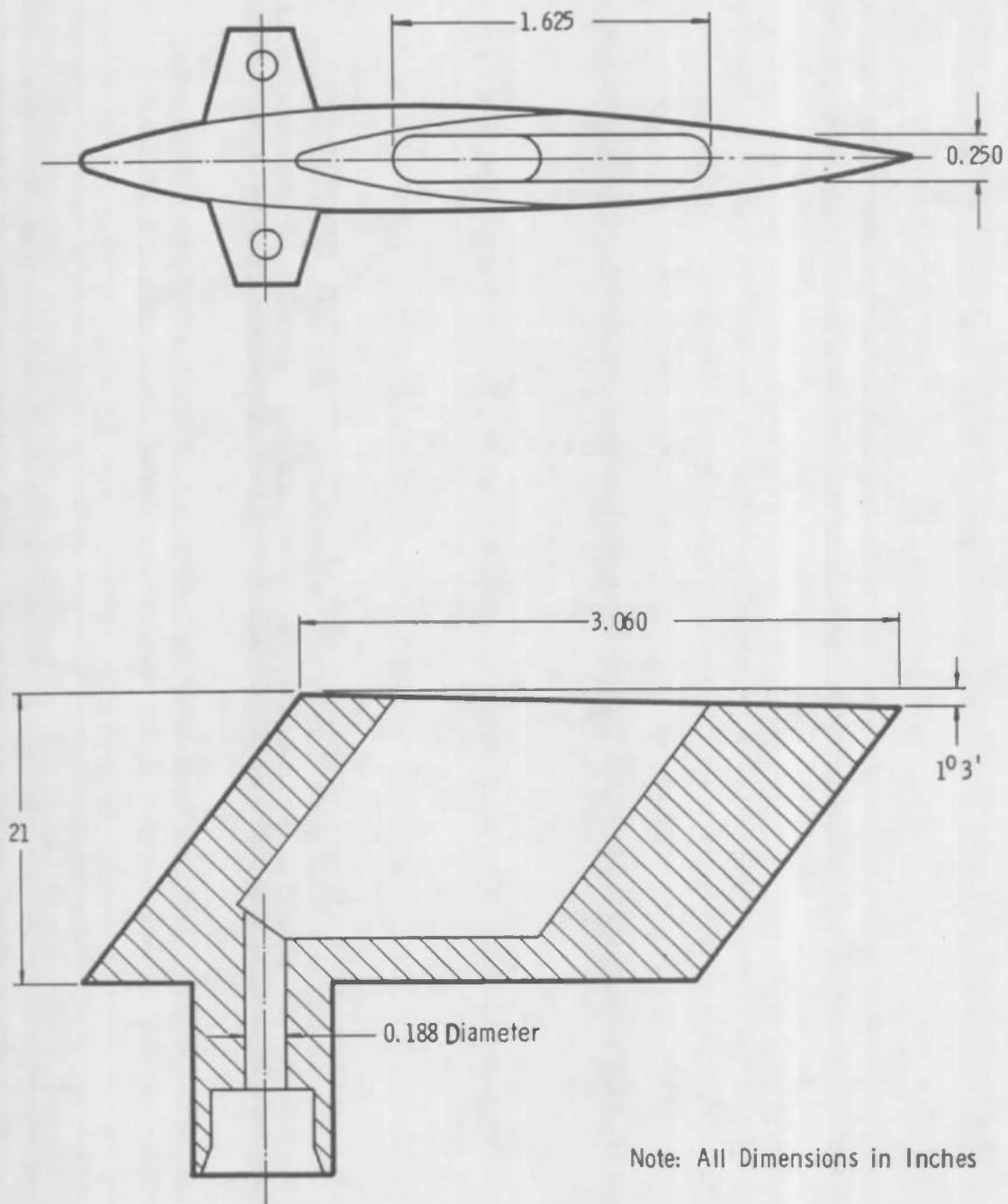
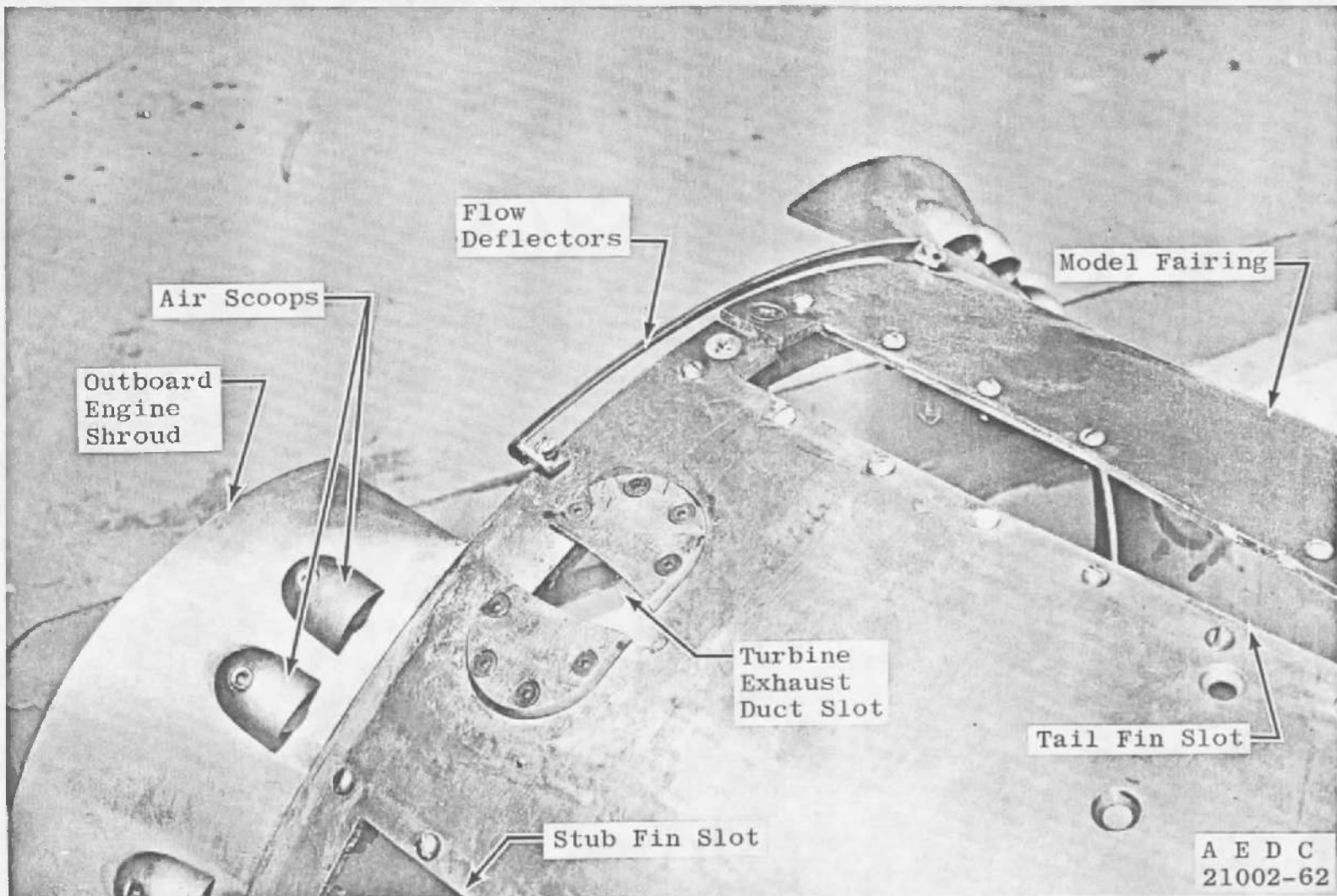
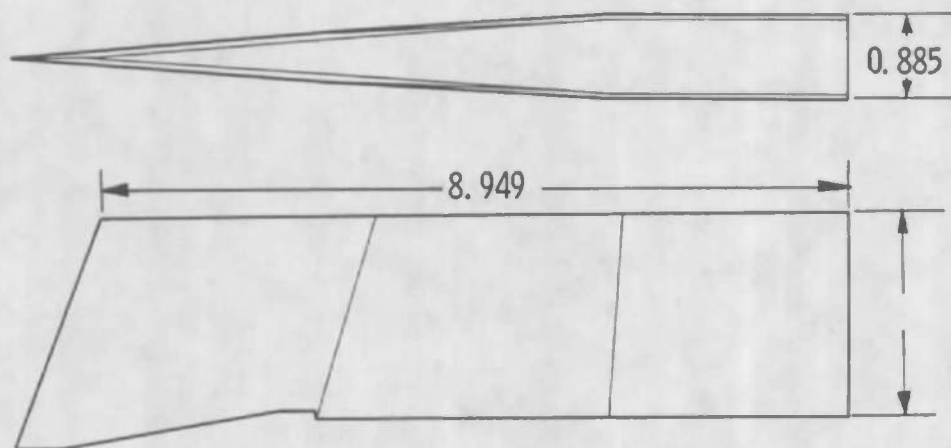


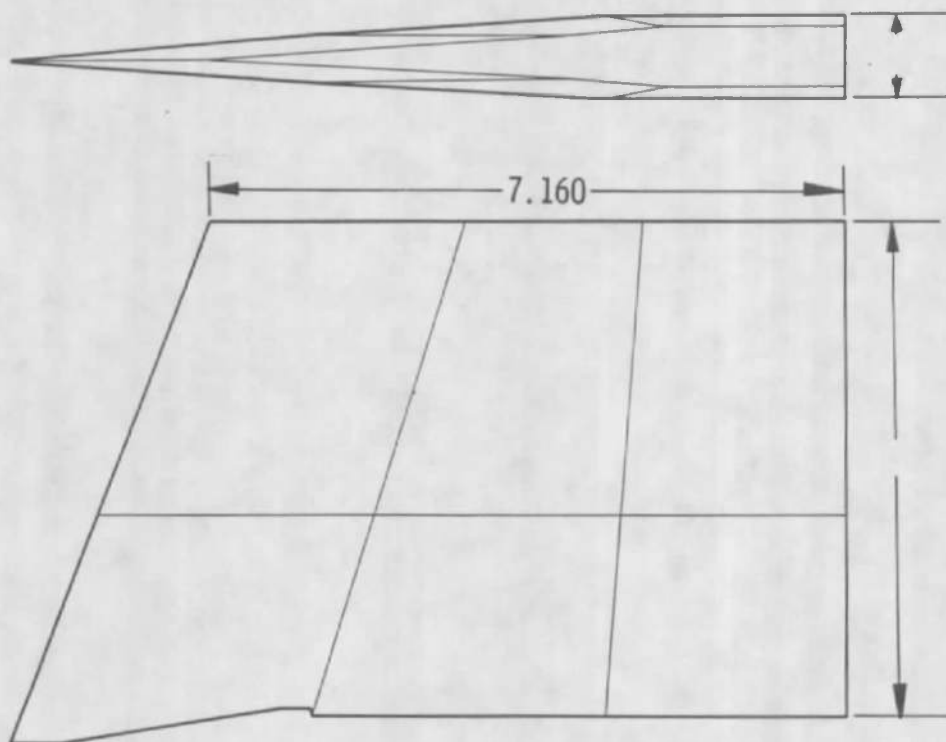
Fig. 9 Turbine Exhaust Duct and Hydrogen Chilldown Duct Design



a. Model Air Scoops, Flow Deflectors, and Outboard Engine Shrouds
 Fig. 10 Model External Hardware



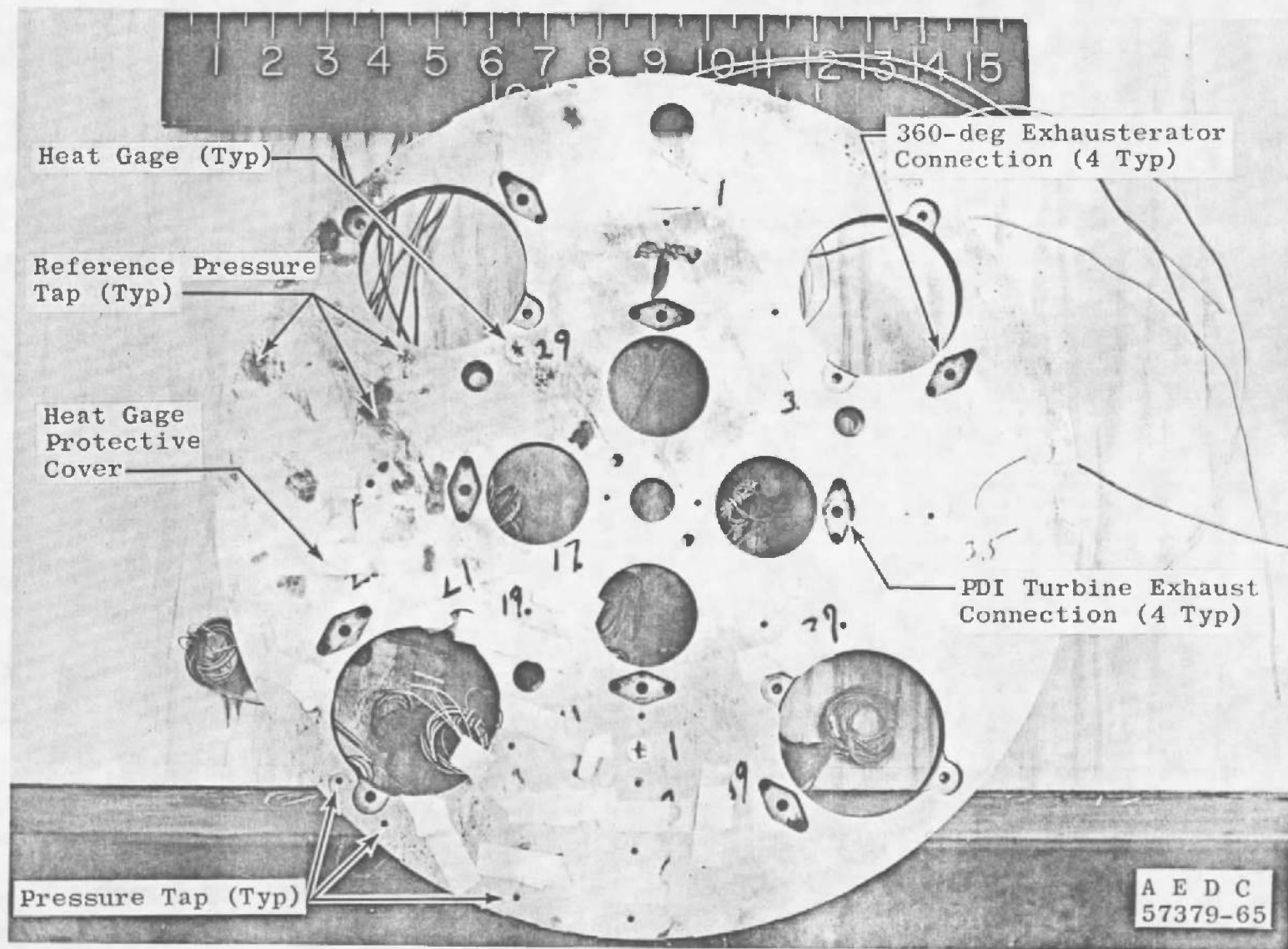
Stub Fins



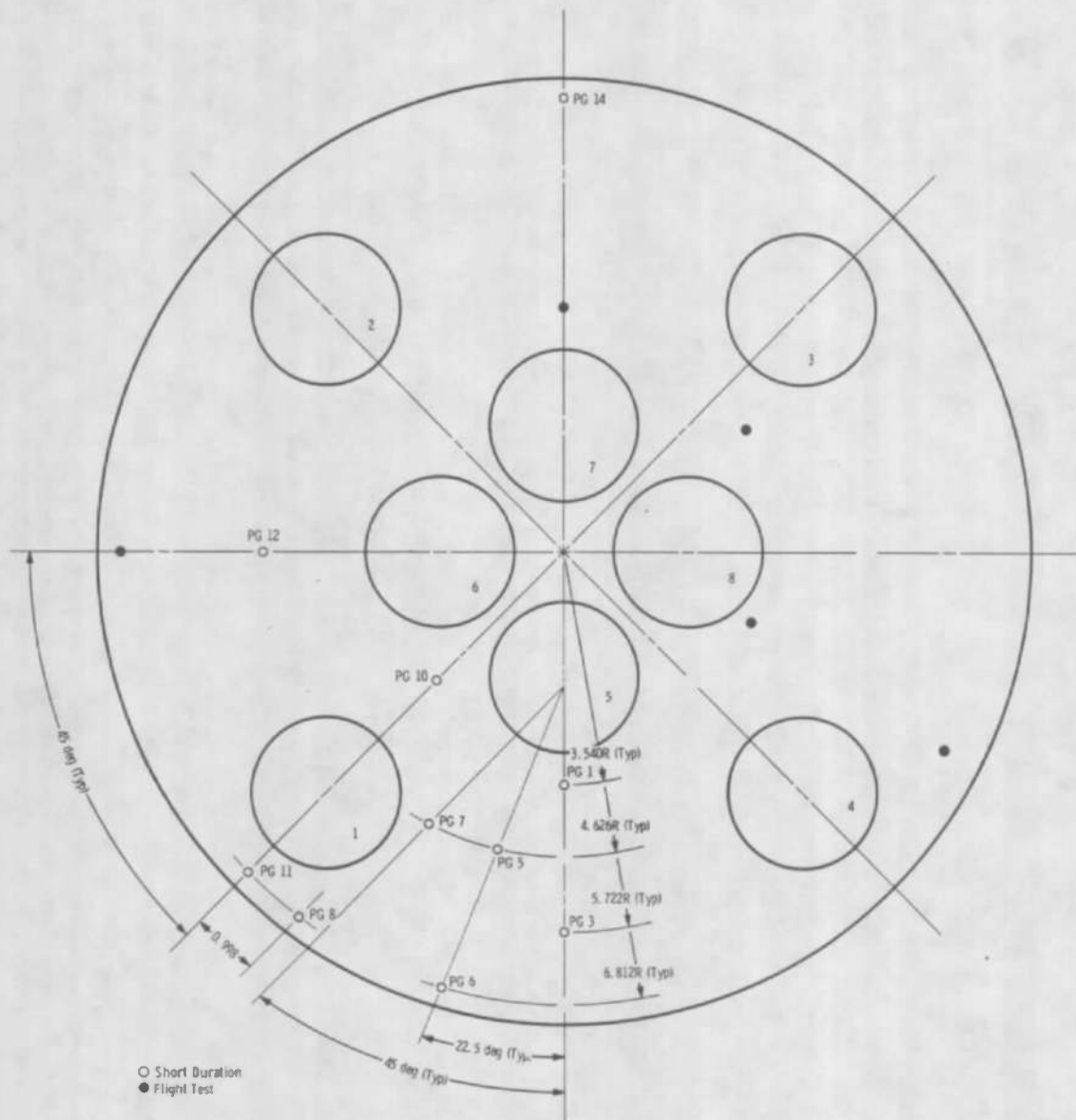
All Dimensions in Inches

Tail Fins

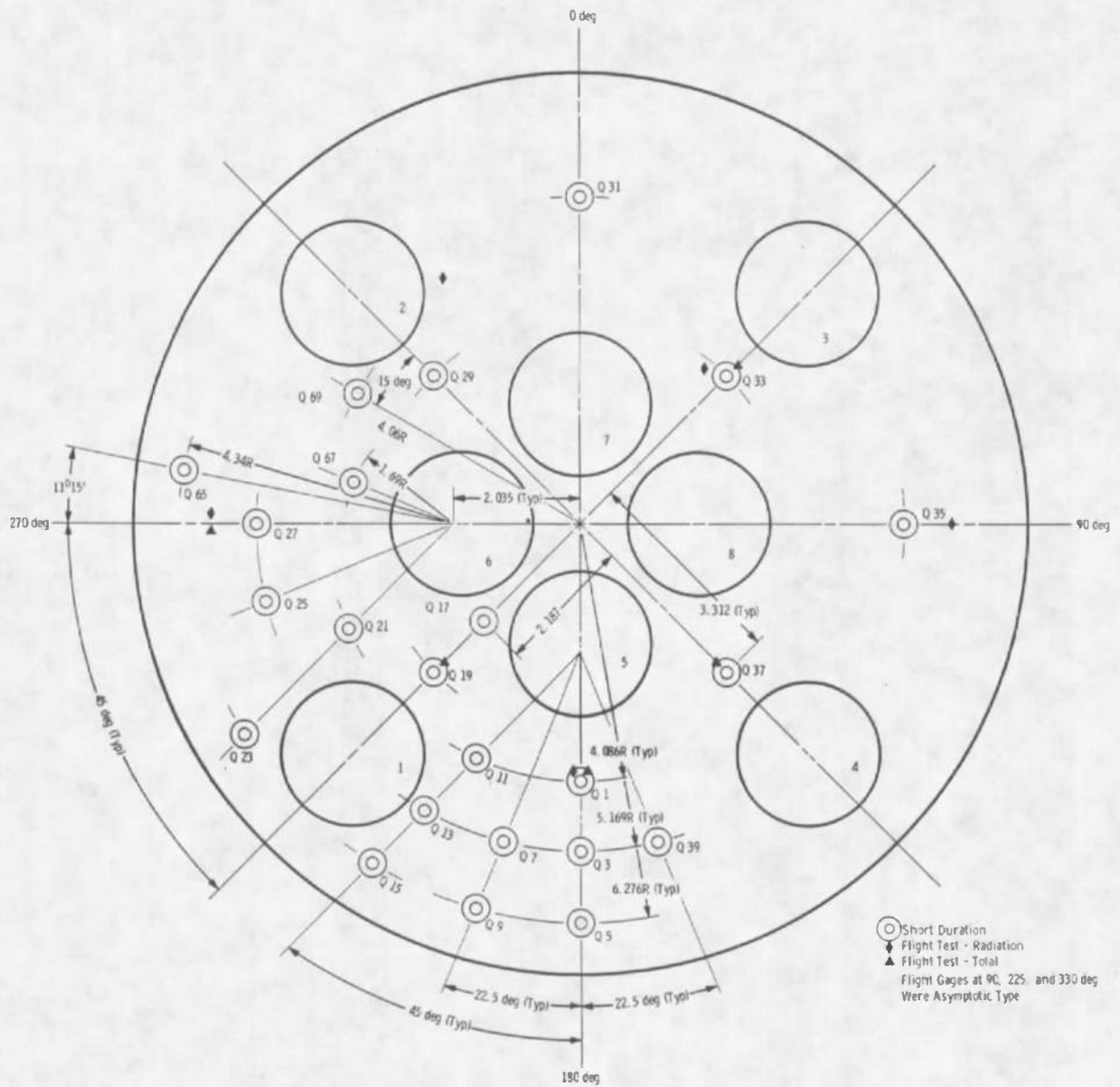
b. Model Fins
Fig. 10 Concluded



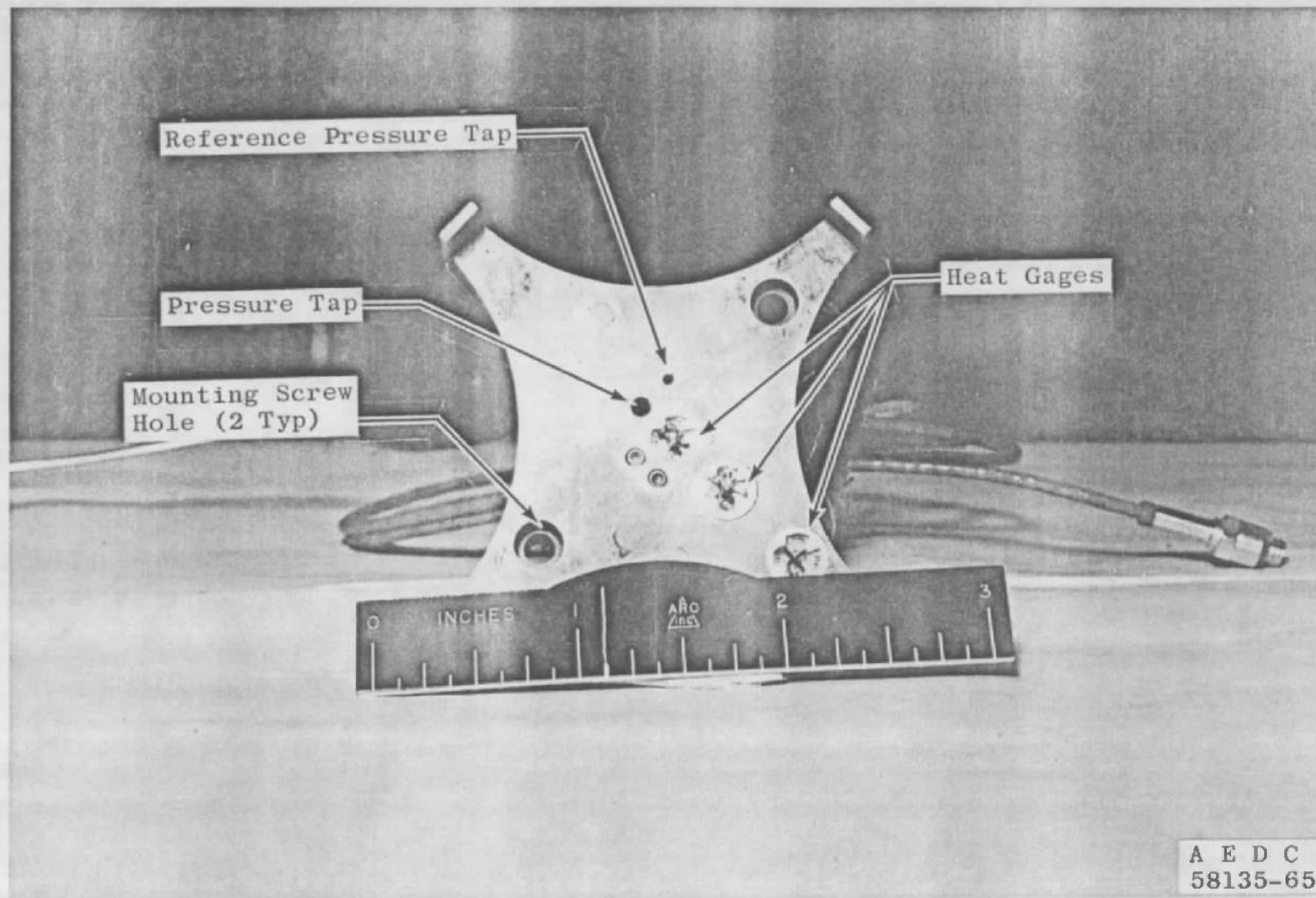
a. Photograph
Fig. 11 Model Base Shield



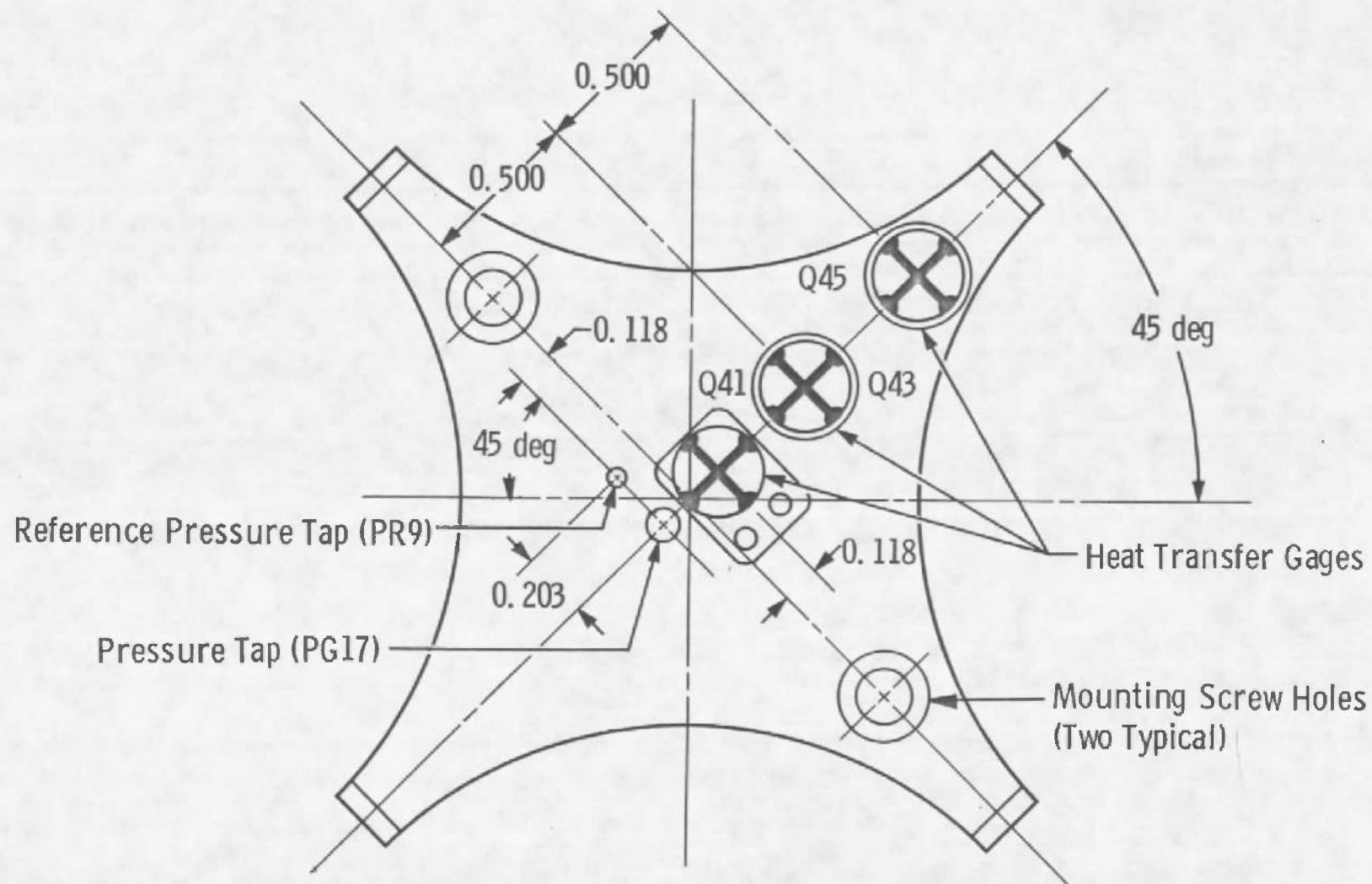
b. Base Pressure Locations
Fig. 11 Continued



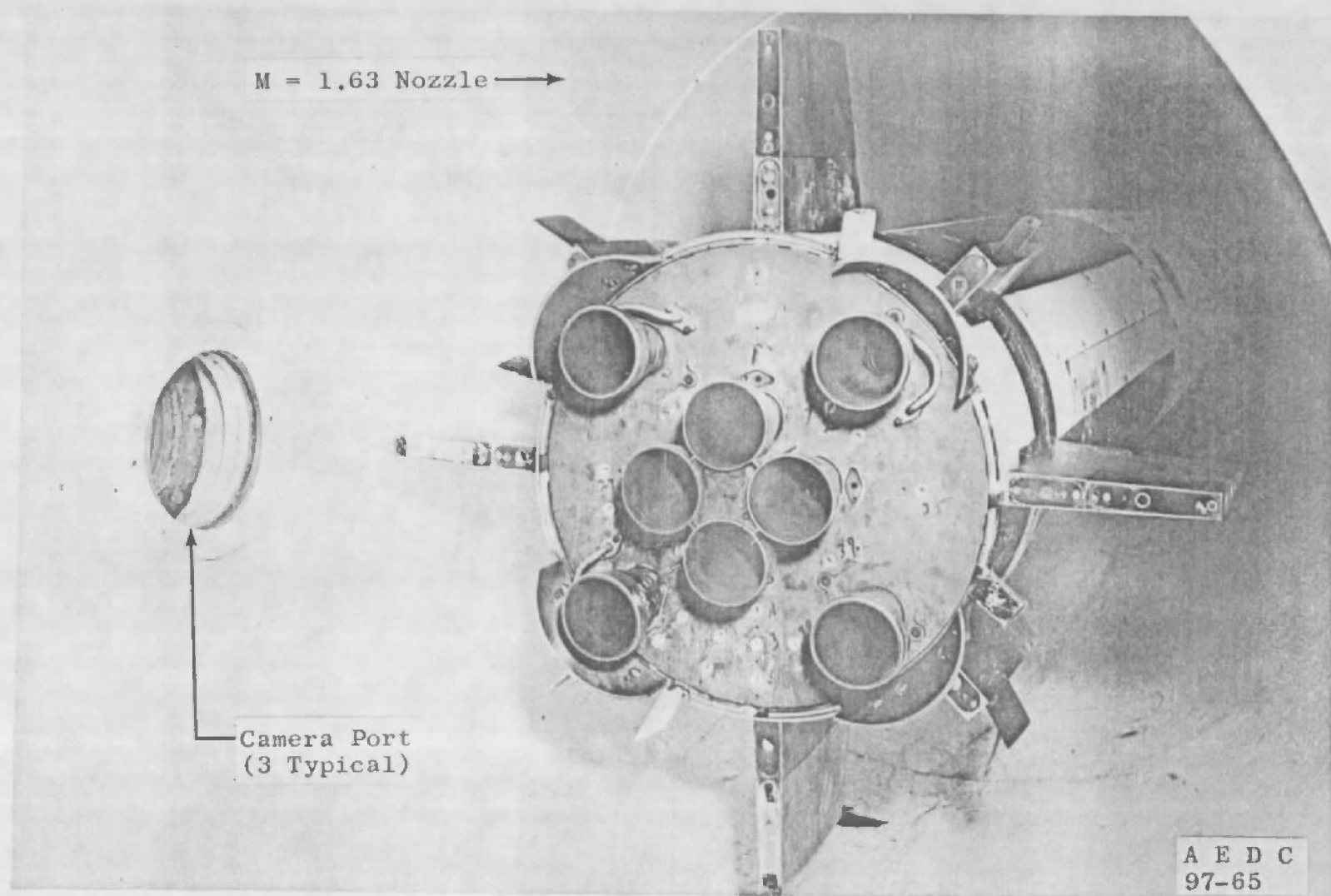
c. Base Heat Transfer Gage Locations
Fig. 11 Concluded



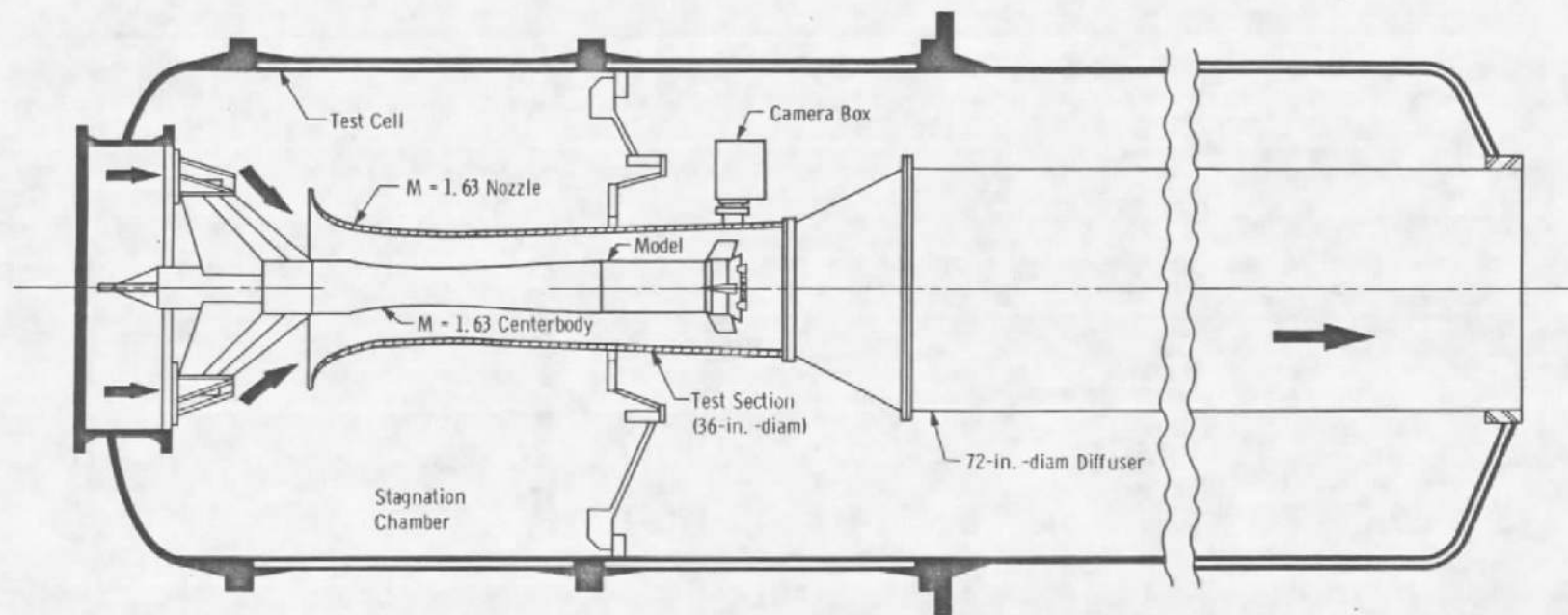
a. Photograph
Fig. 12 Flame Shield



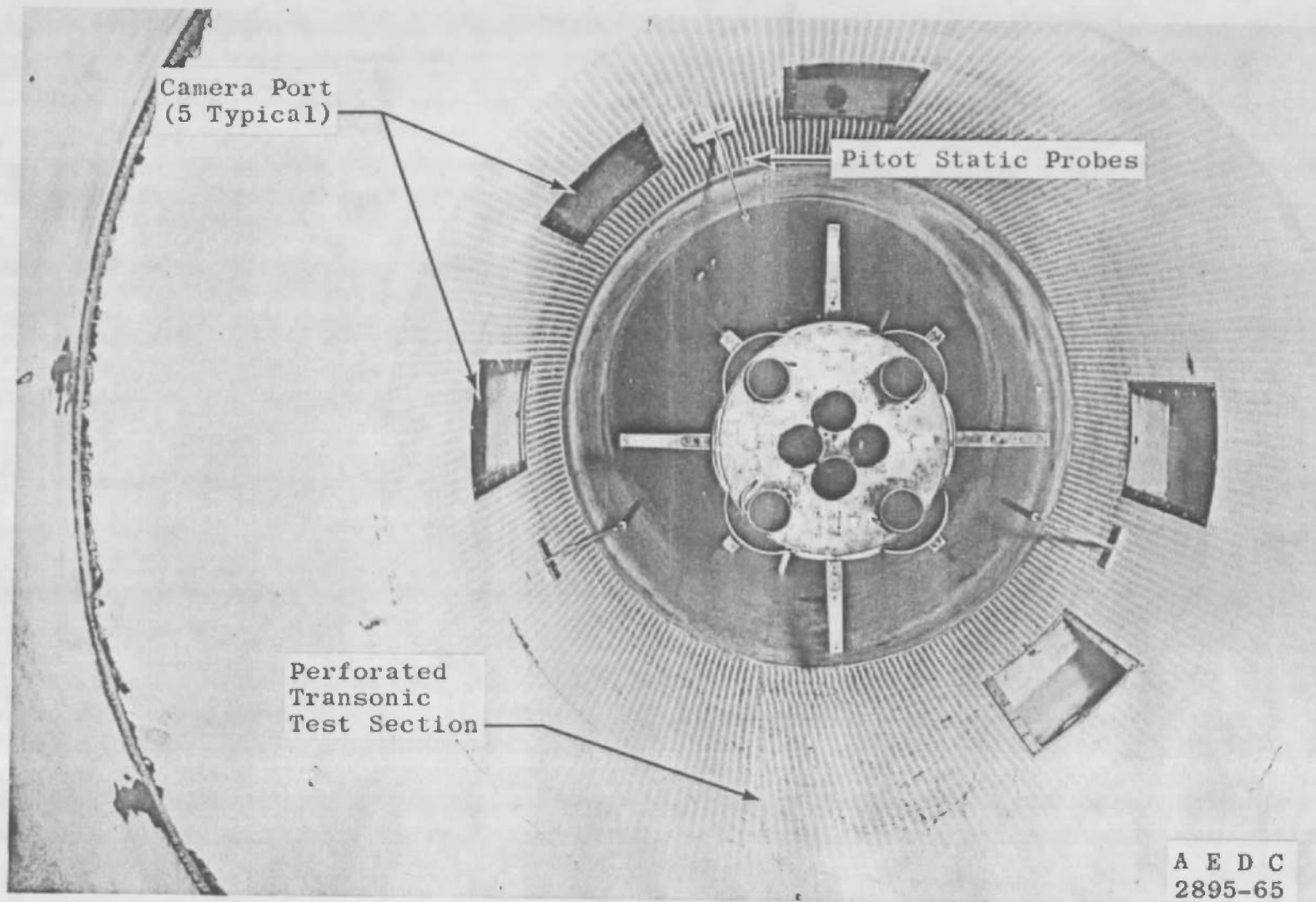
b. Instrumentation Locations
Fig. 12 Concluded



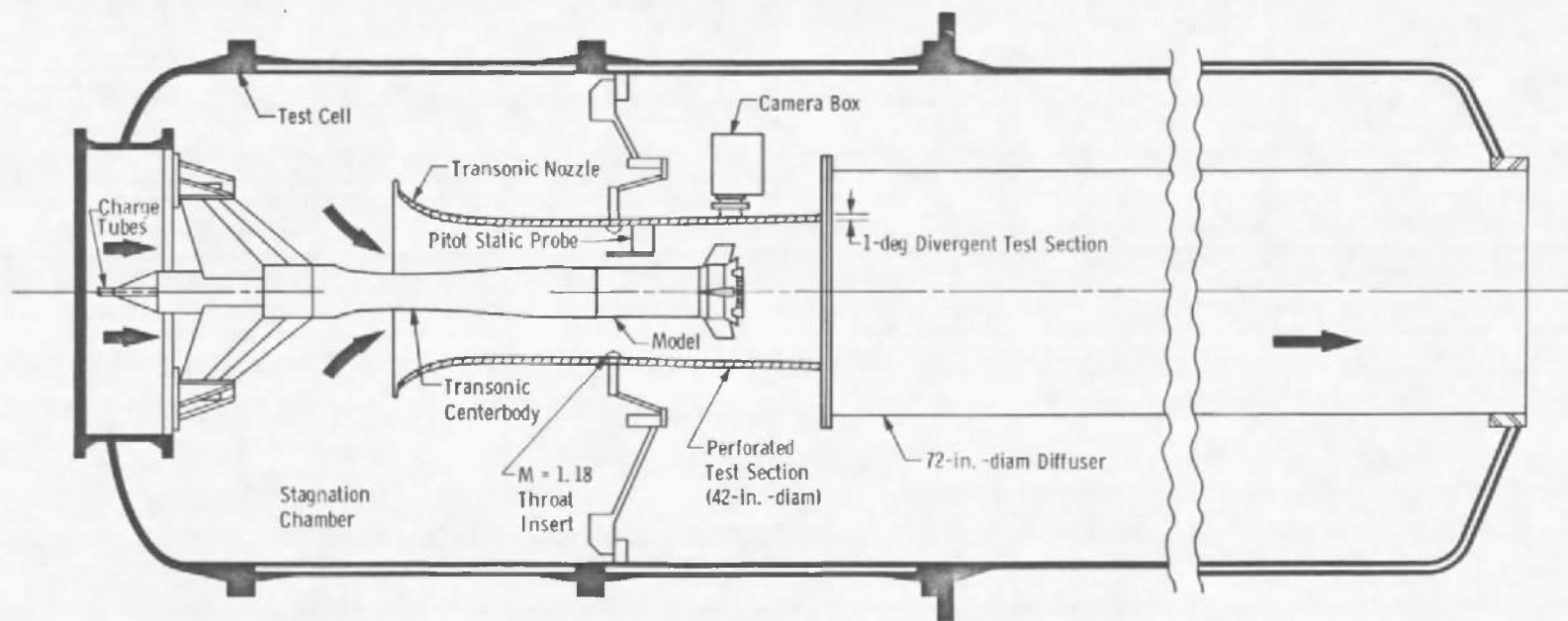
a. Photograph Mach Number 1.63
Fig. 13 Model Installation



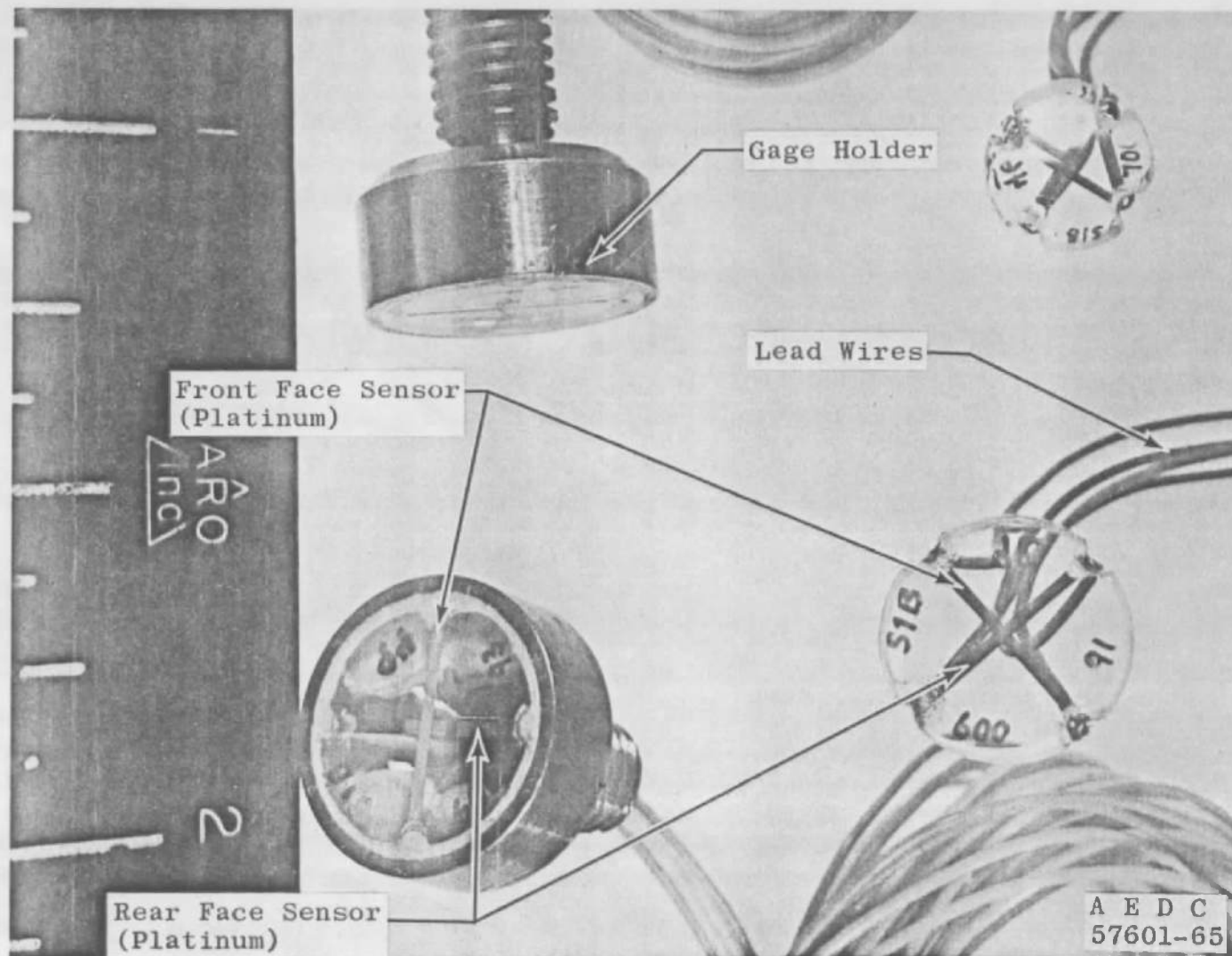
b. Schematic Mach Number 1.63
Fig. 13 Continued



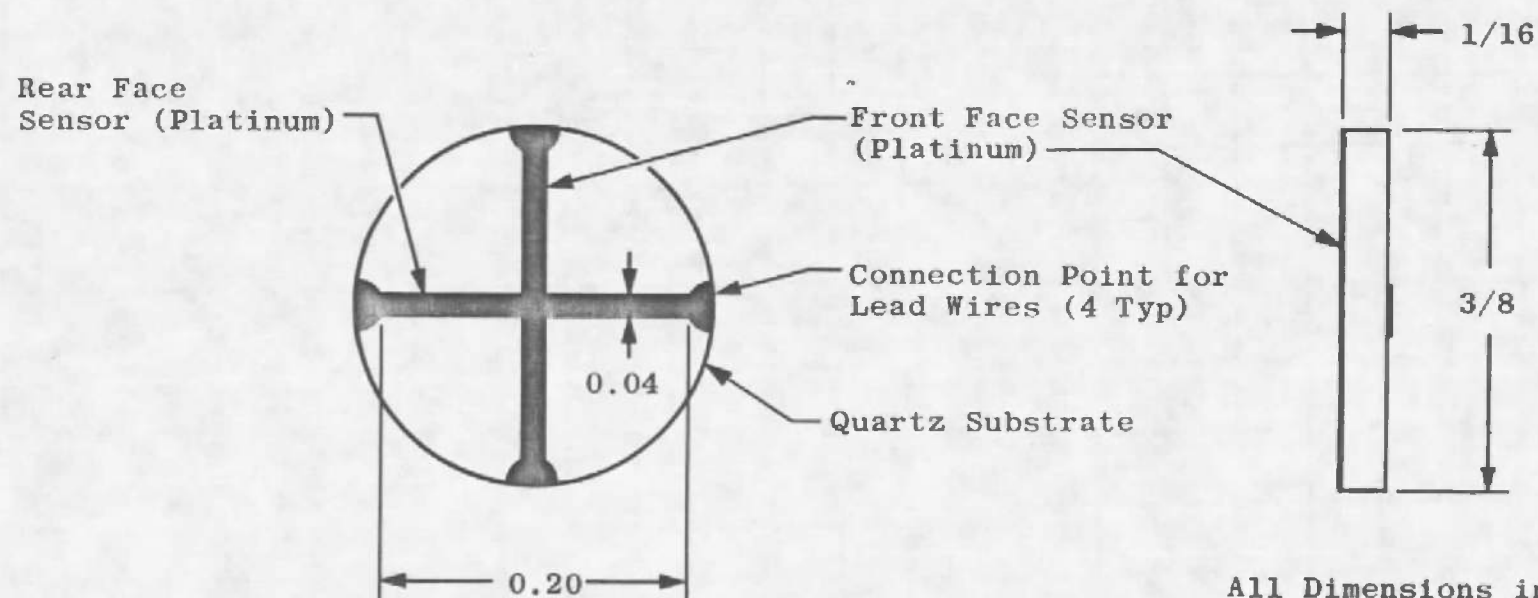
c. Photograph Mach Number 1.16
Fig. 13 Continued



d. Schematic Mach Number 1.16
Fig. 13 Concluded

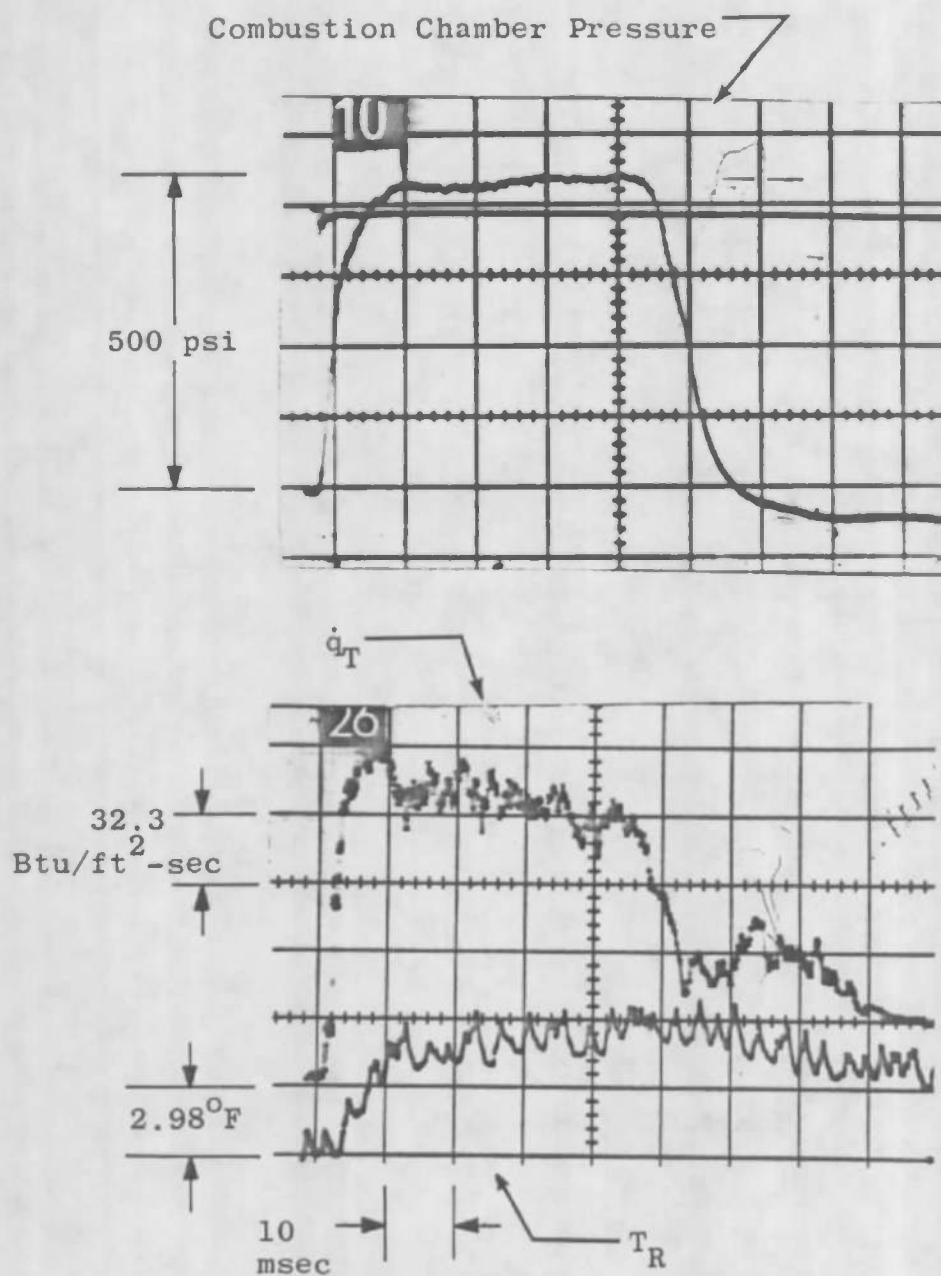


a. Photograph
Fig. 14 Thin-Film Heat Transfer Gage



All Dimensions in Inches

b. Schematic
Fig. 14 Concluded



- Notes:
1. \dot{q}_T is the recorded output of the front face of a typical heat transfer gage which has been converted from ΔT to \dot{q} by an electronic passive differentiator or \dot{q} meter.
 2. T_R is the recorded temperature of the rear face of a typical gage.

Fig. 15 Short-Duration Heat Gage Circuit Schematic

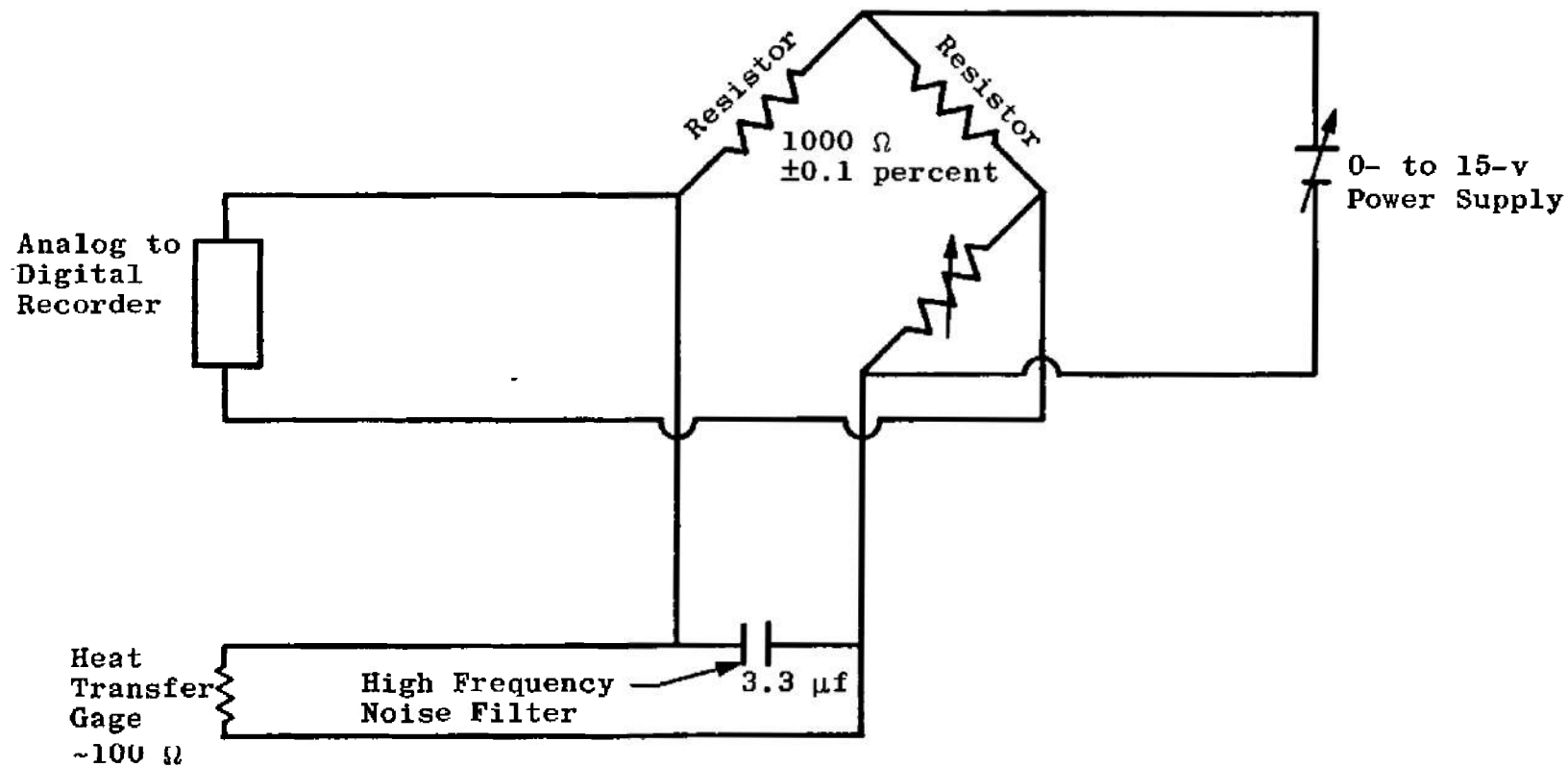


Fig. 16 Typical Oscilloscope Chamber Pressure and Heat Transfer Gage Output Photographs

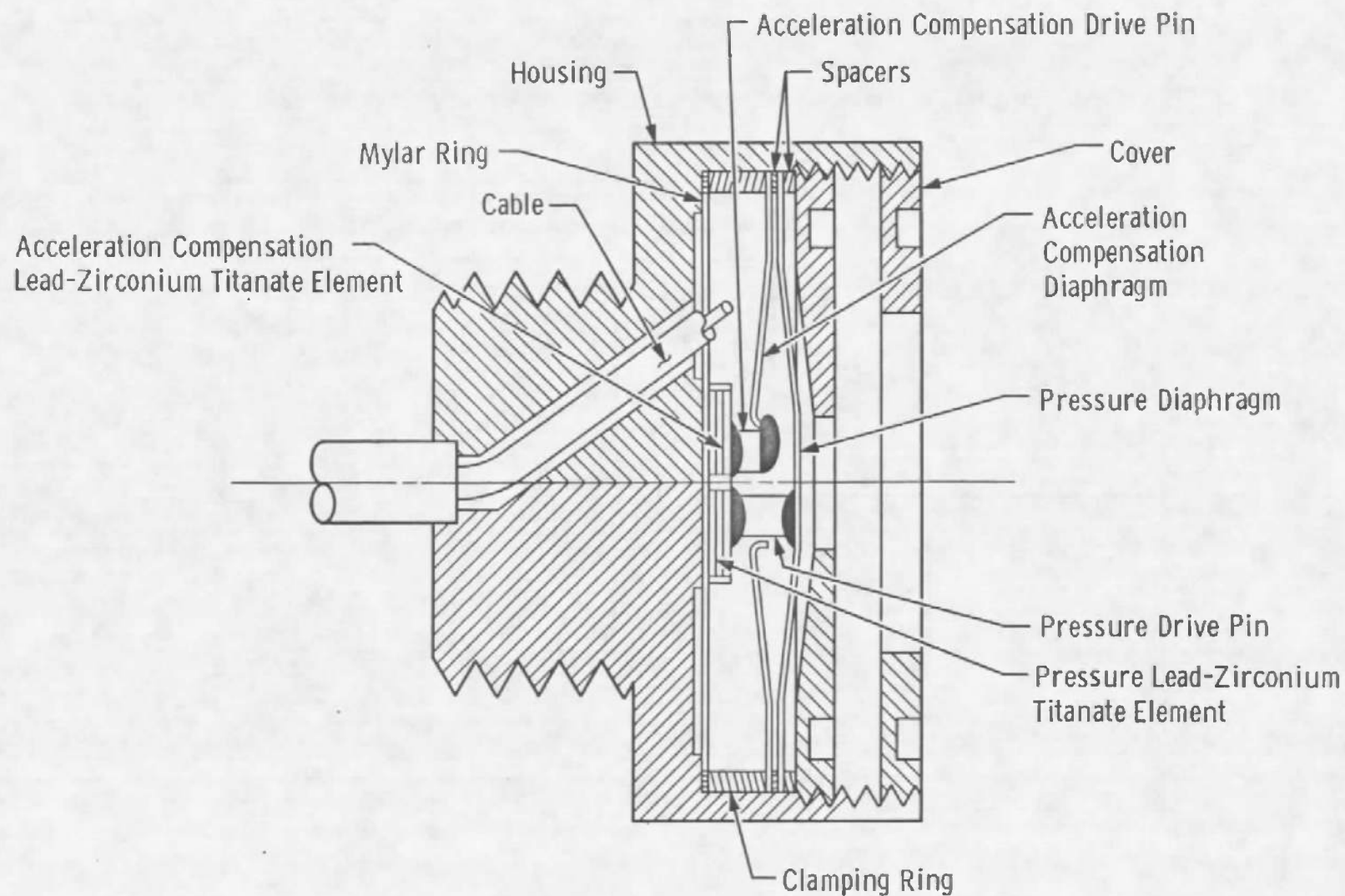
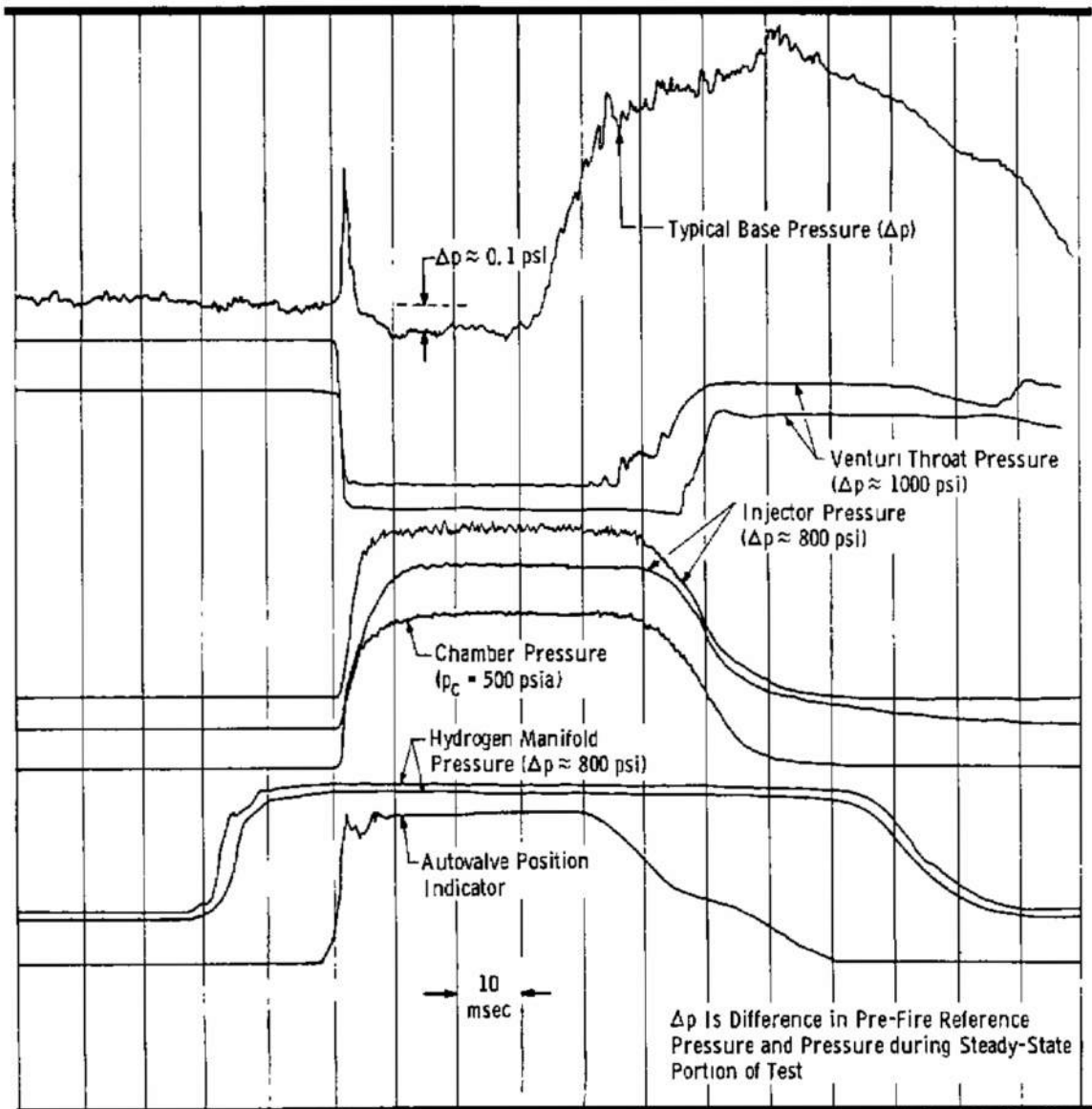
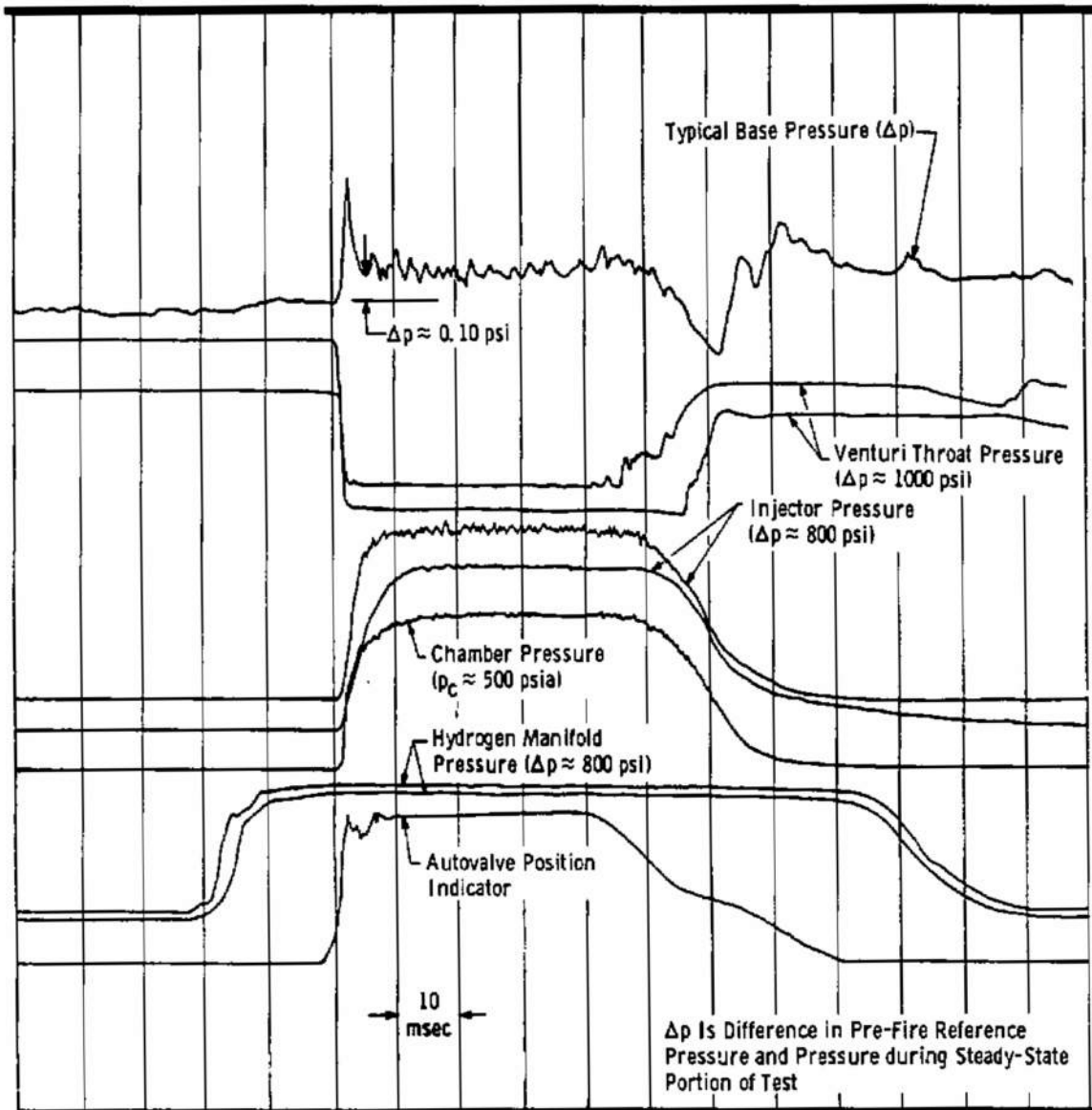


Fig. 17 Schematic of Lead Zirconium Titanate Short-Duration Pressure Transducer

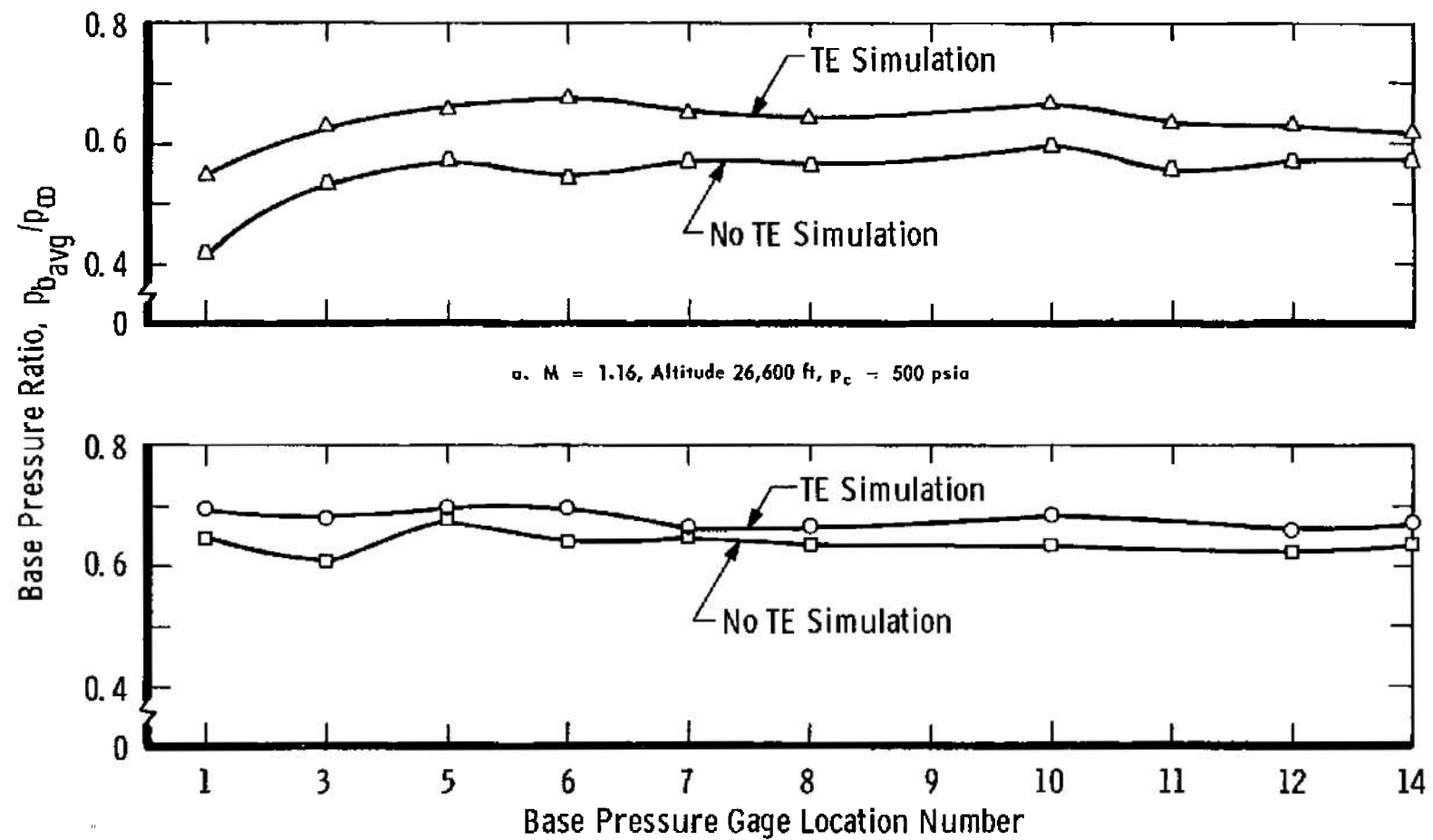


a. $M = 1.16$

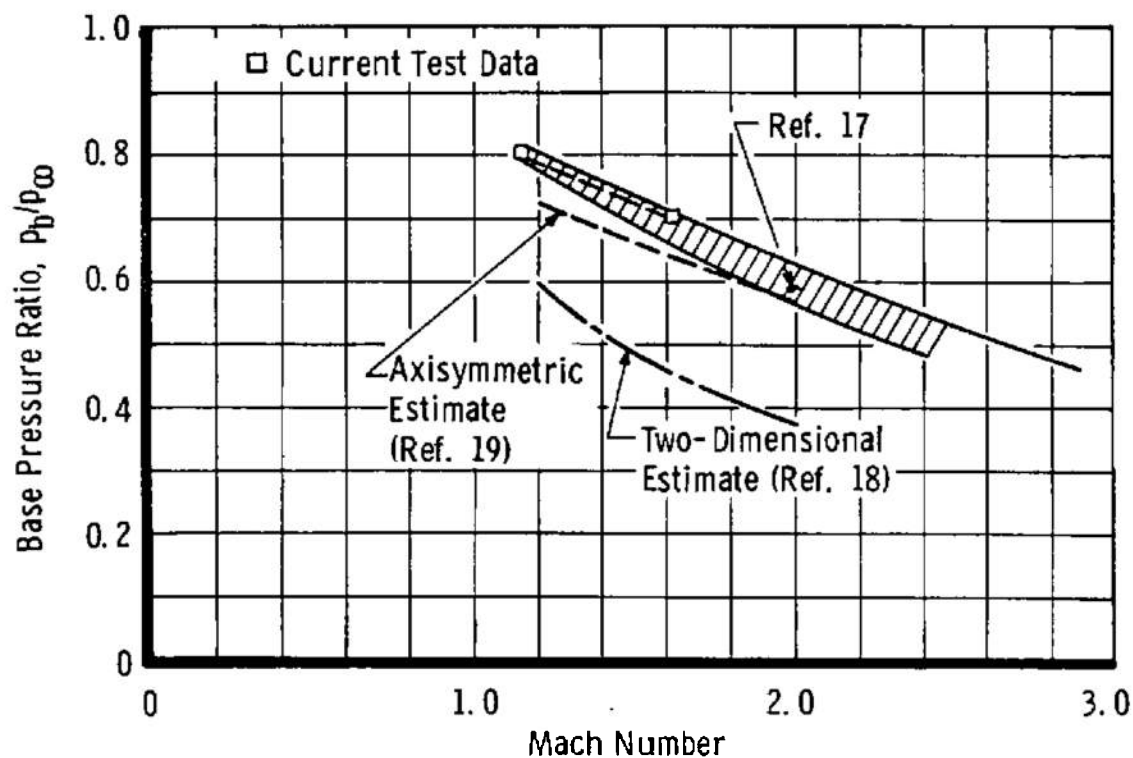
Fig. 18 Typical Oscillograph of Model Sequence of Operation and Pressure Traces



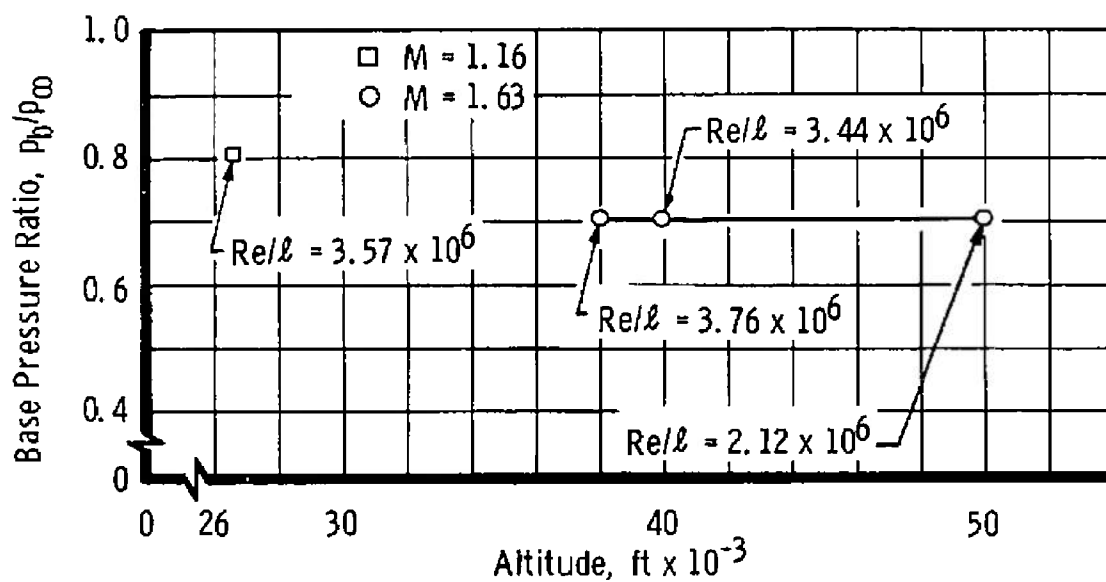
b. $M = 1.63$
Fig. 18 Concluded



b. $M = 1.63$, Altitude 38,000 ft, $p_c = 500$ psia
 Fig. 19 Base Pressure Distribution with Engines Operating

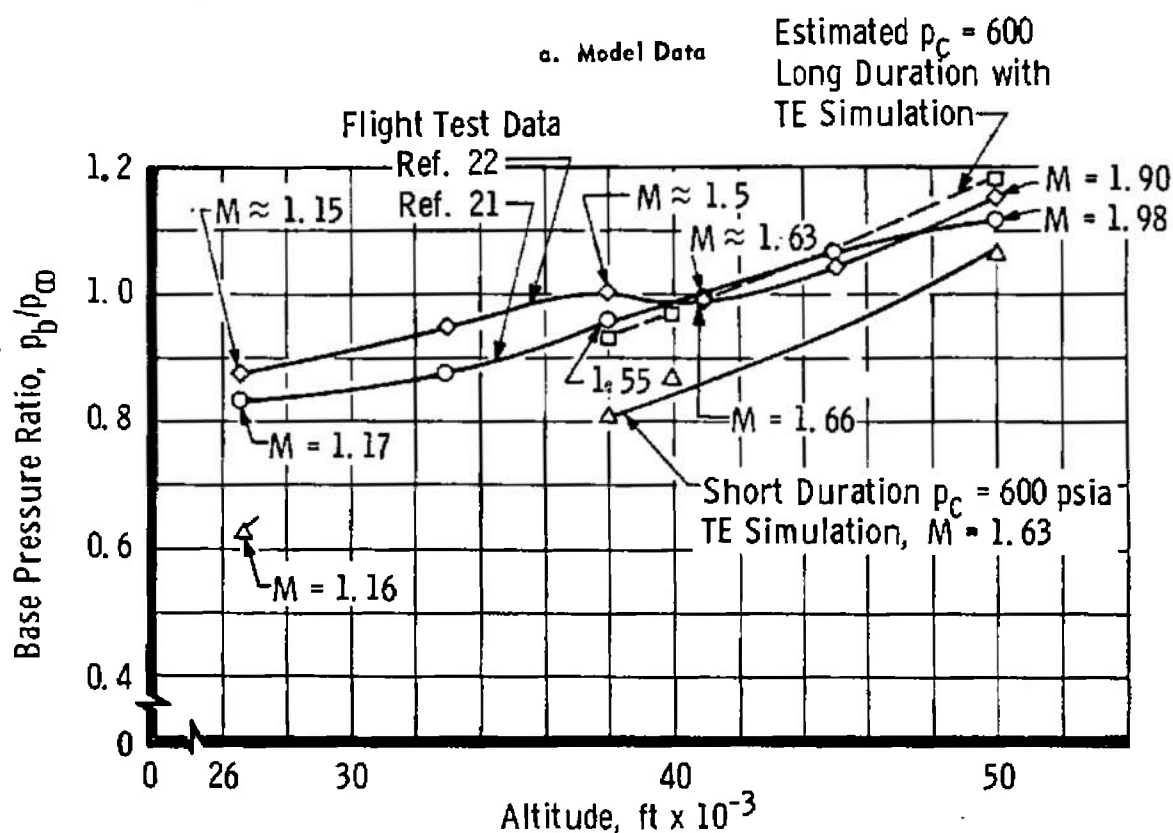
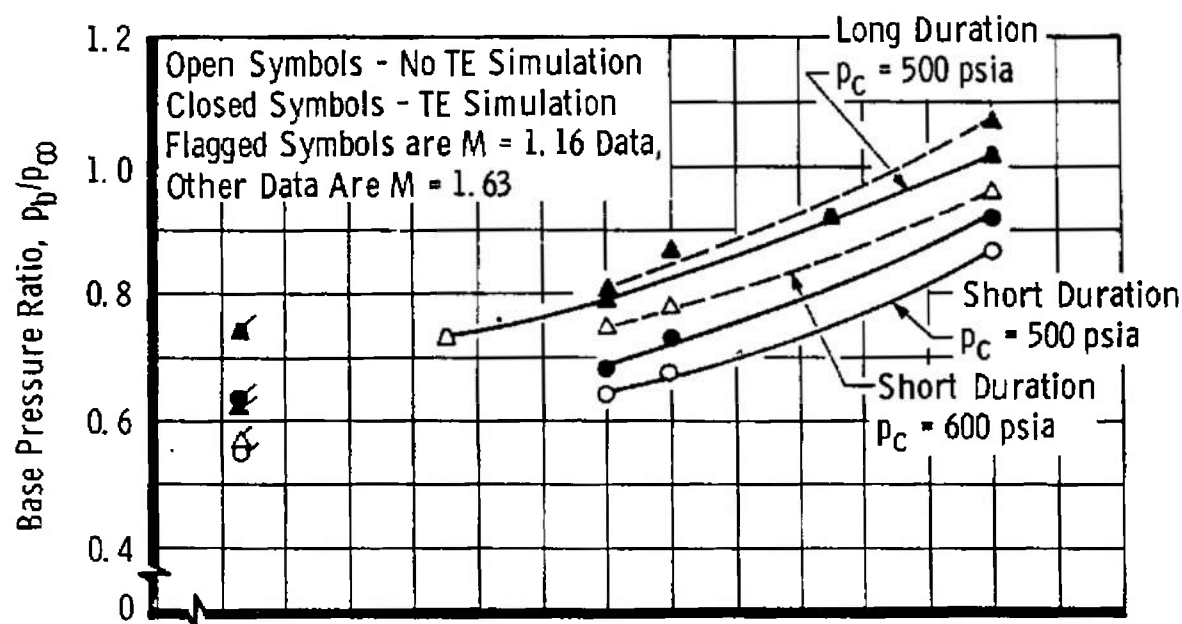


a. Cold Flow Base Pressure versus Mach Number



b. Cold Flow Base Pressure versus Altitude

Fig. 20 Cold Flow Base Pressure



b. Comparison of Model and Flight Data

Fig. 21 Effects of Altitude and Combustor Pressure on Base Pressure

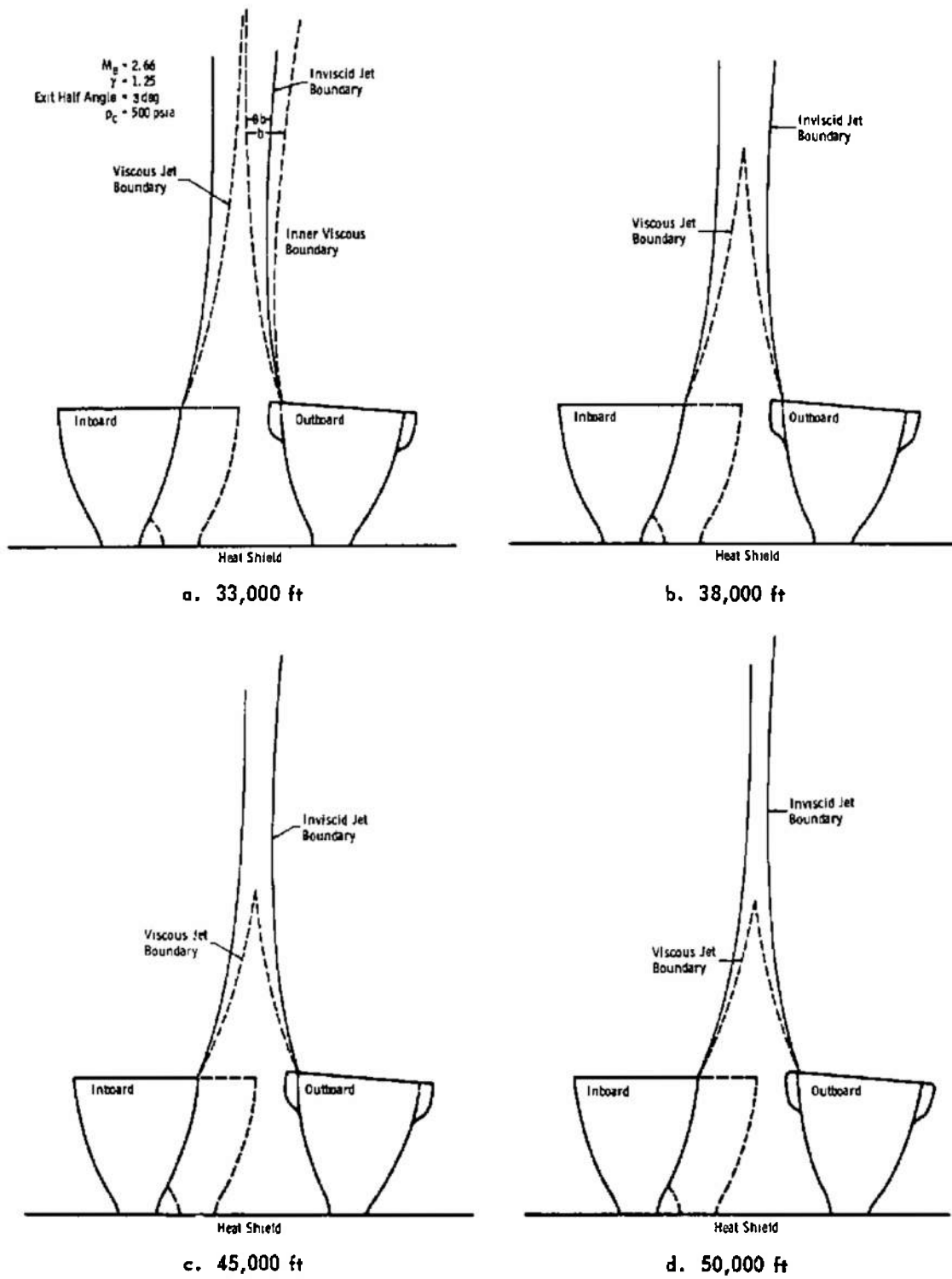
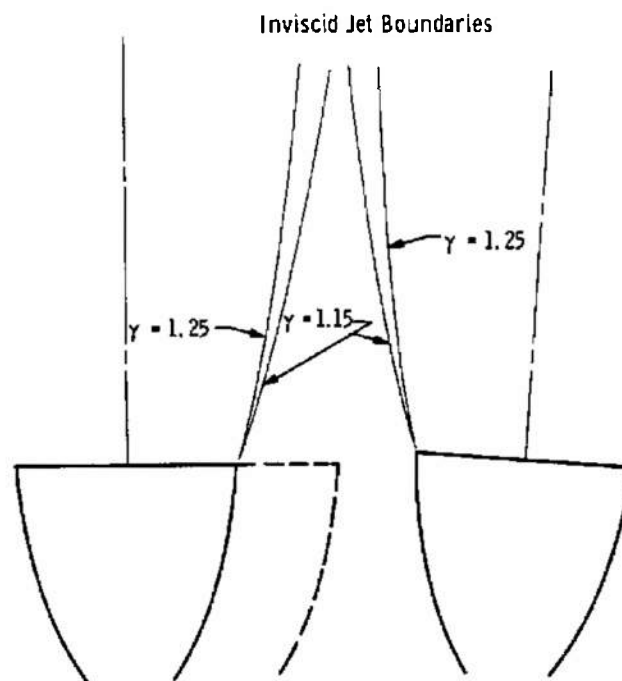


Fig. 22 Jet Boundaries Calculated for Various Altitudes

$p_c = 500$ psia
 $p_\infty = 3.0$ psia
 $\theta_N = 3.0$ -deg Nozzle Exit Angle
 $A/A^* = 80:1$



e. 38,000 ft, Comparison of $\gamma = 1.15$ and 1.25
 Fig. 22 Concluded

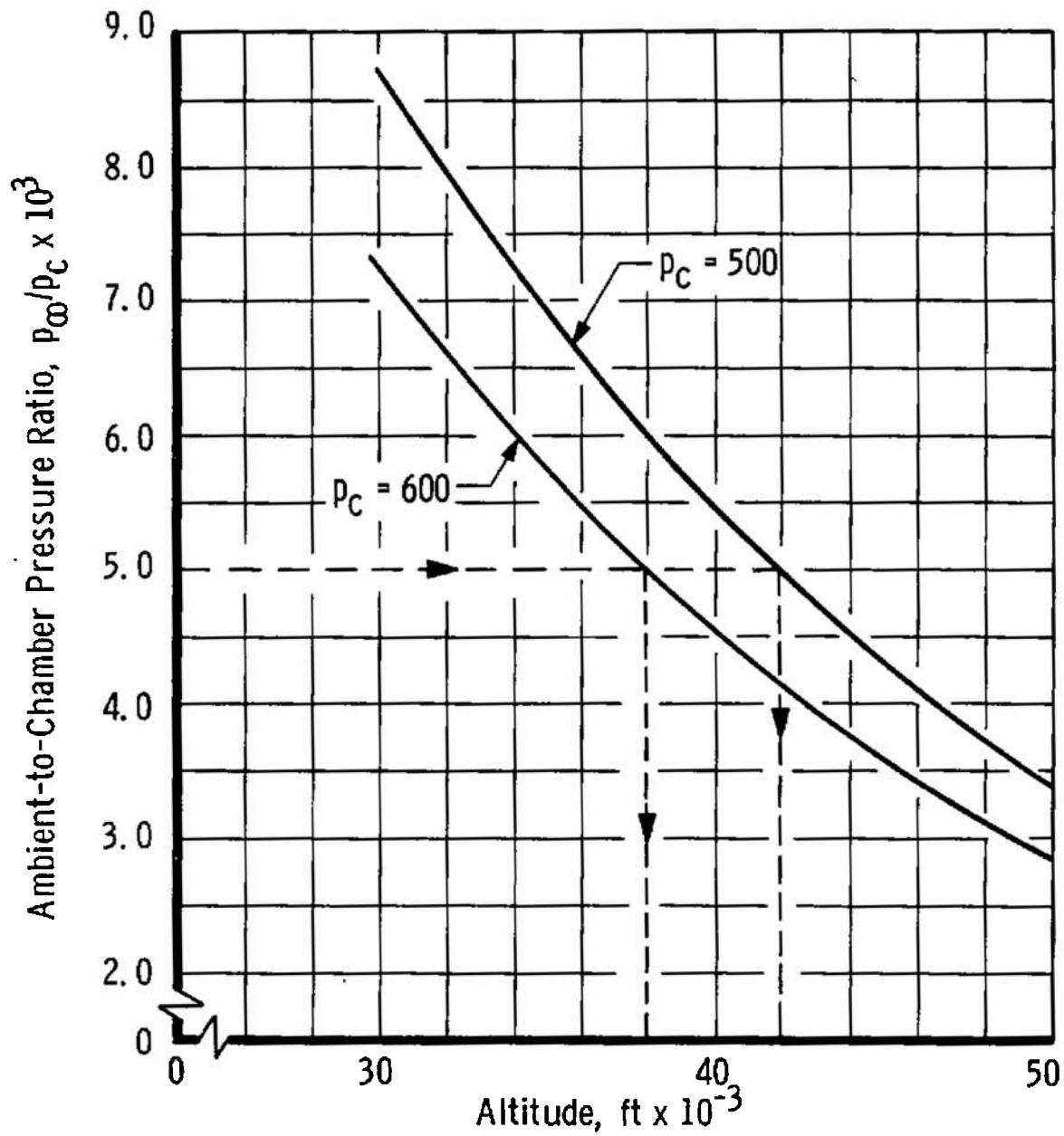


Fig. 23 Ambient-to-Chamber Pressure Ratio versus Altitude

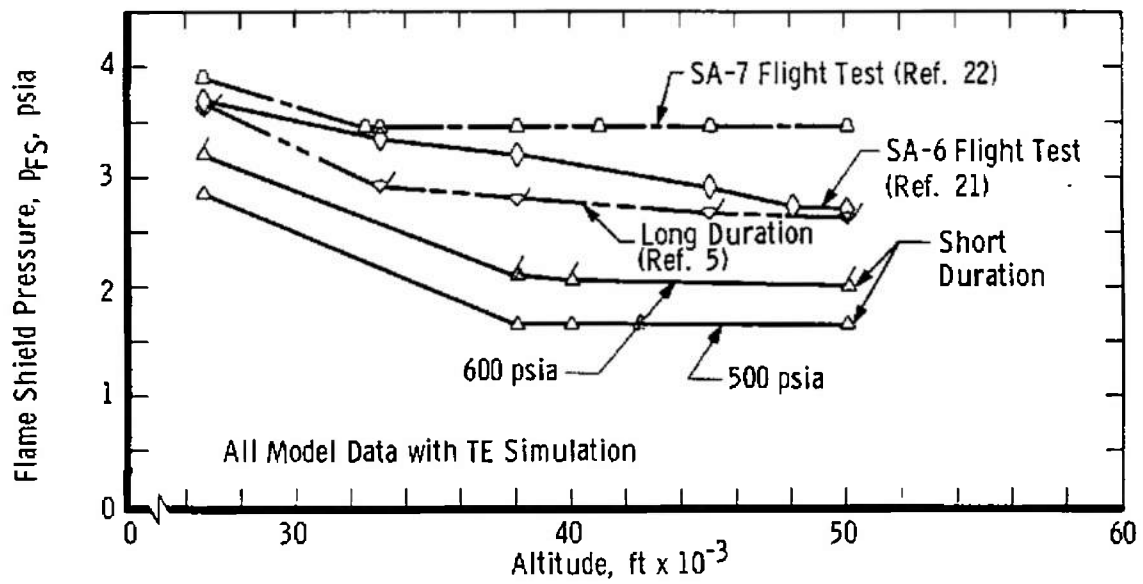


Fig. 24 Flame Shield Pressure versus Altitude

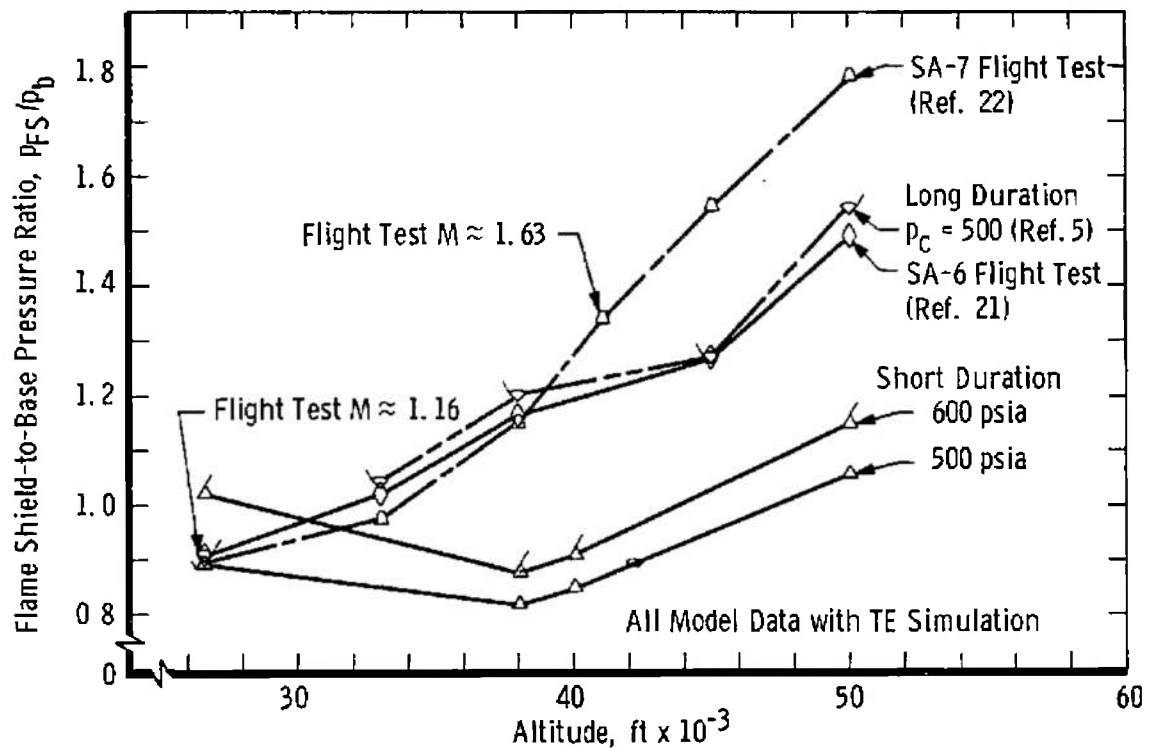


Fig. 25 Flame Shield-to-Base Pressure Ratio versus Altitude

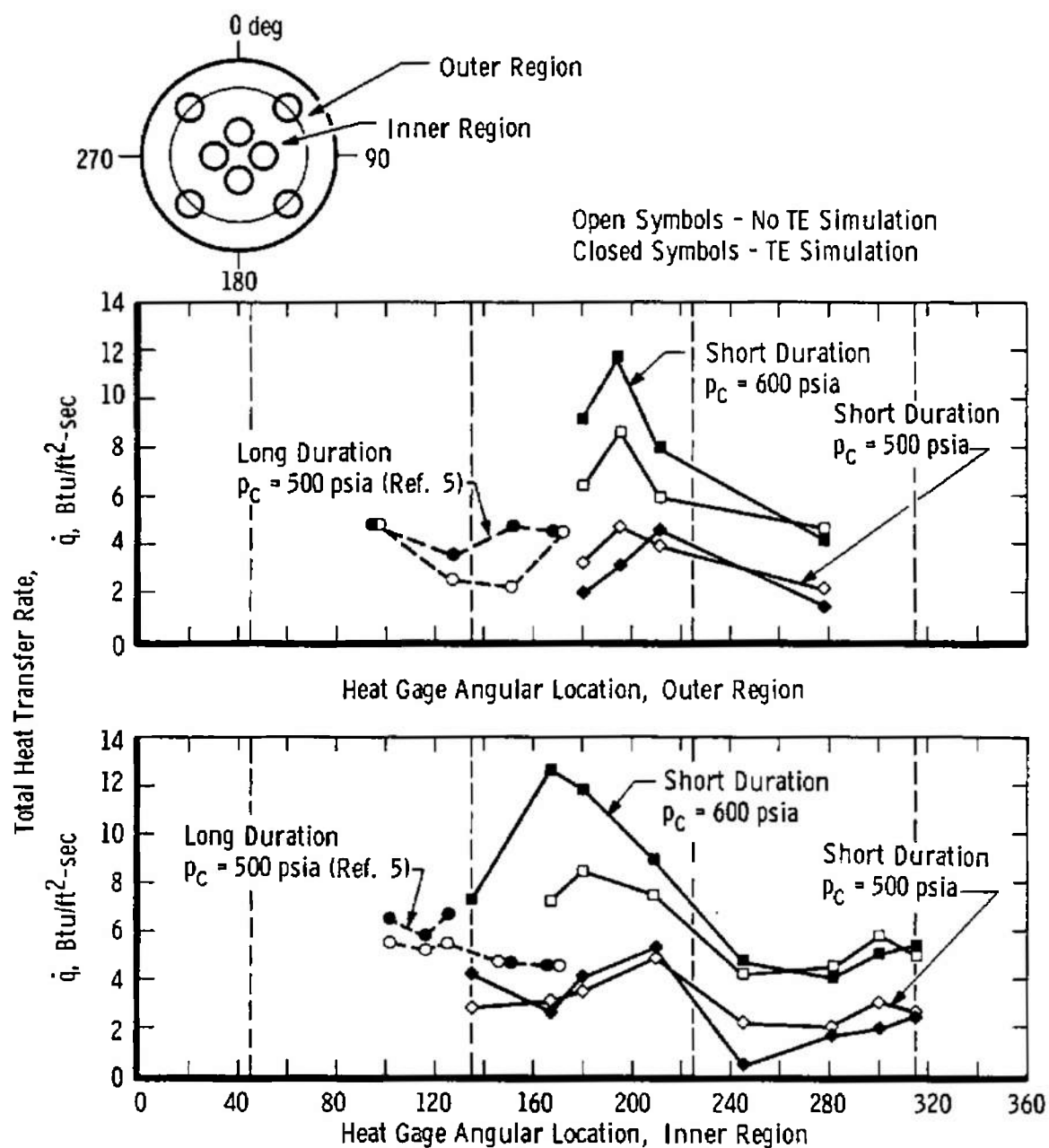


Fig. 26 Model Base Total Heat Transfer Distribution at $M = 1.63$ and 38,000 ft

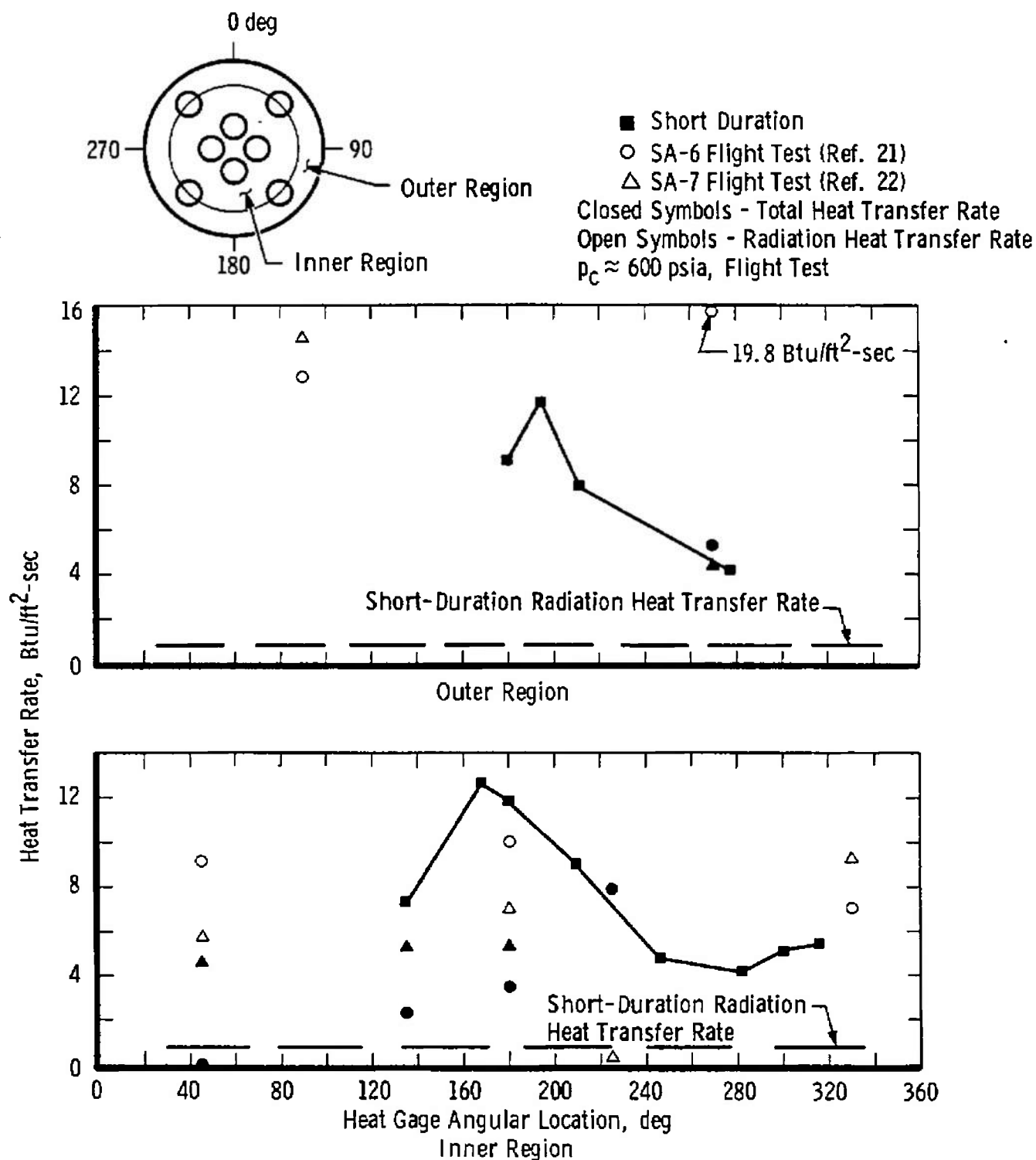
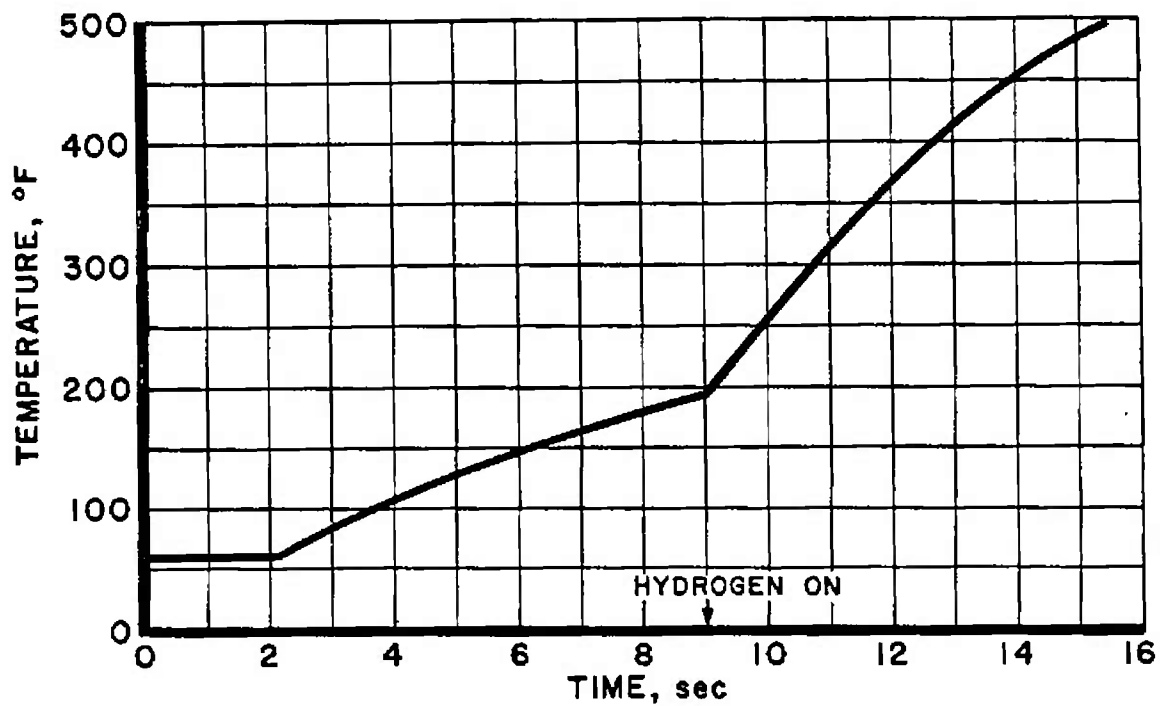
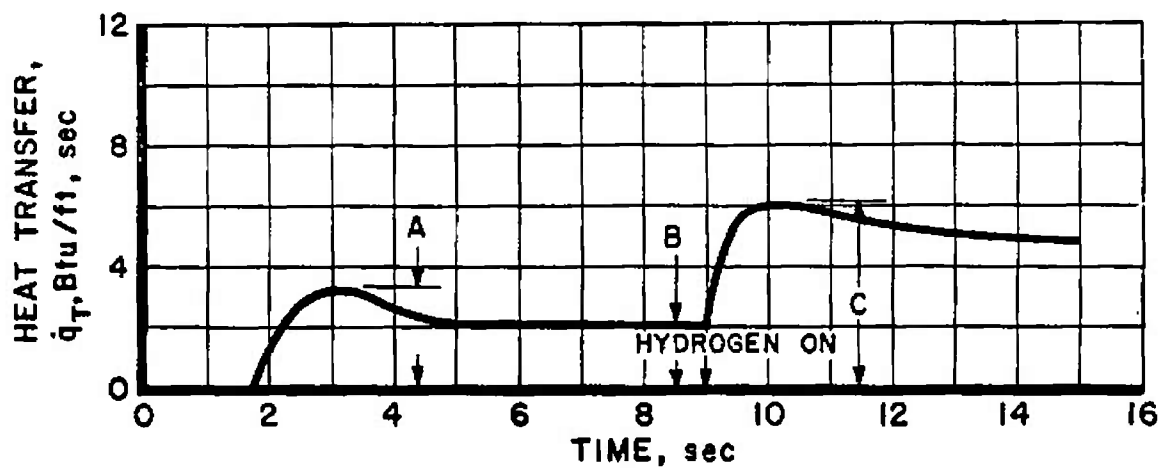


Fig. 27 Comparison of Model Data and Flight Test Base Heating Data



a. Temperature



b. Heat Transfer

Fig. 28 Typical Long-Duration Base Calorimeter Temperature and Heat Transfer-Time Histories

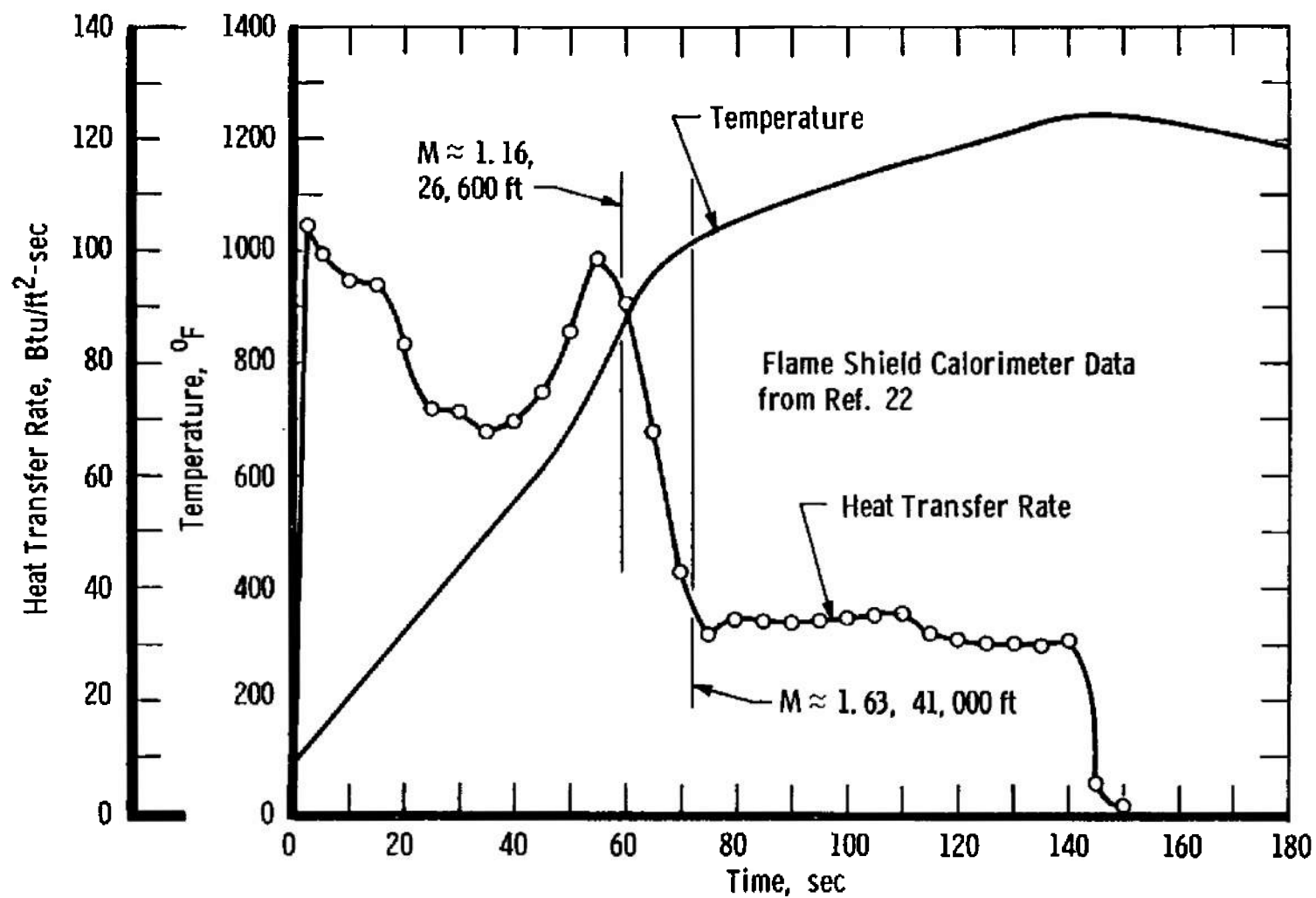
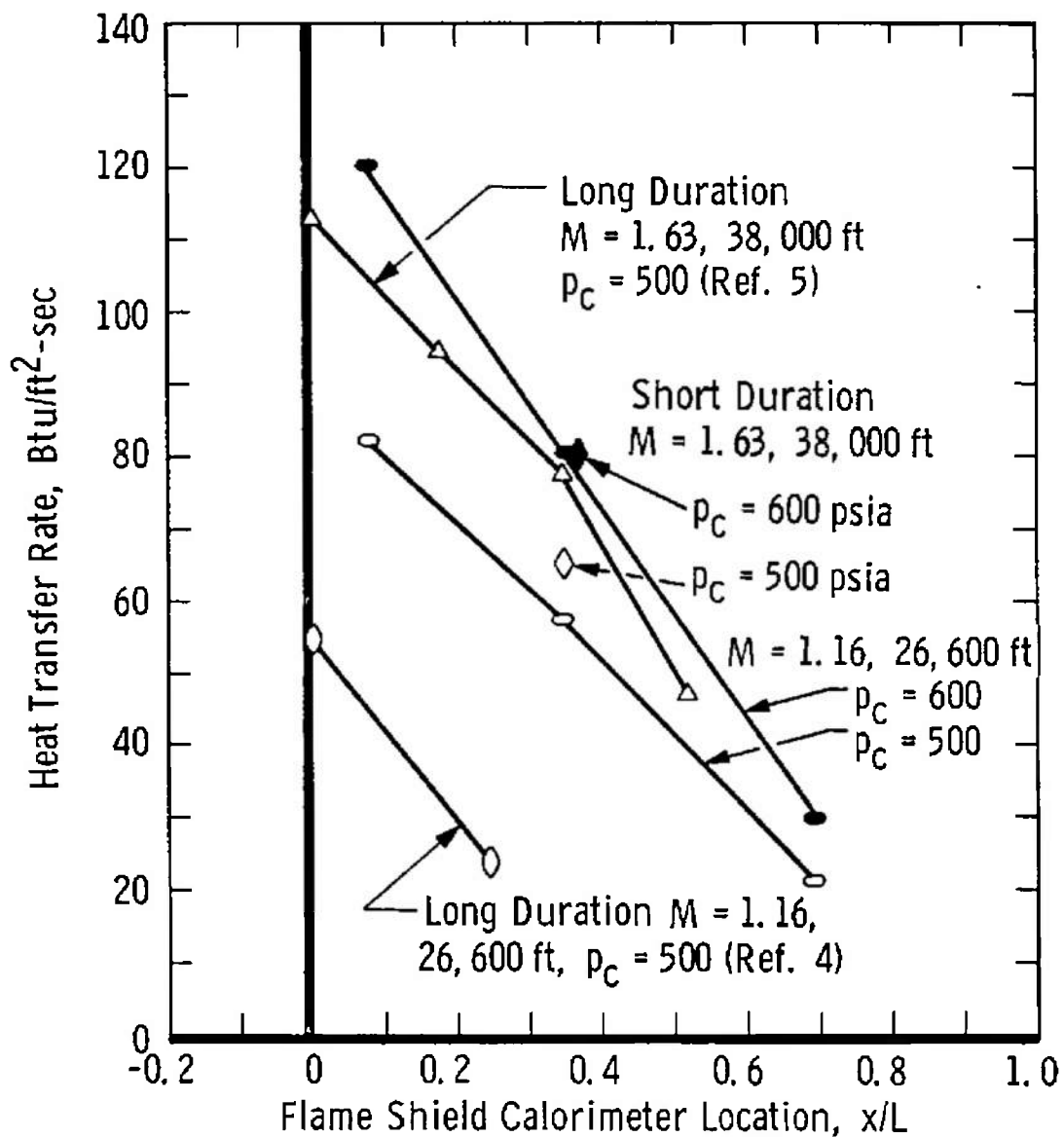
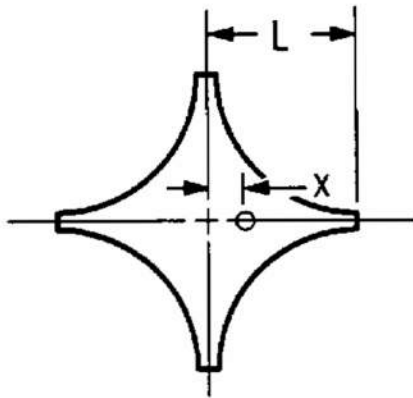
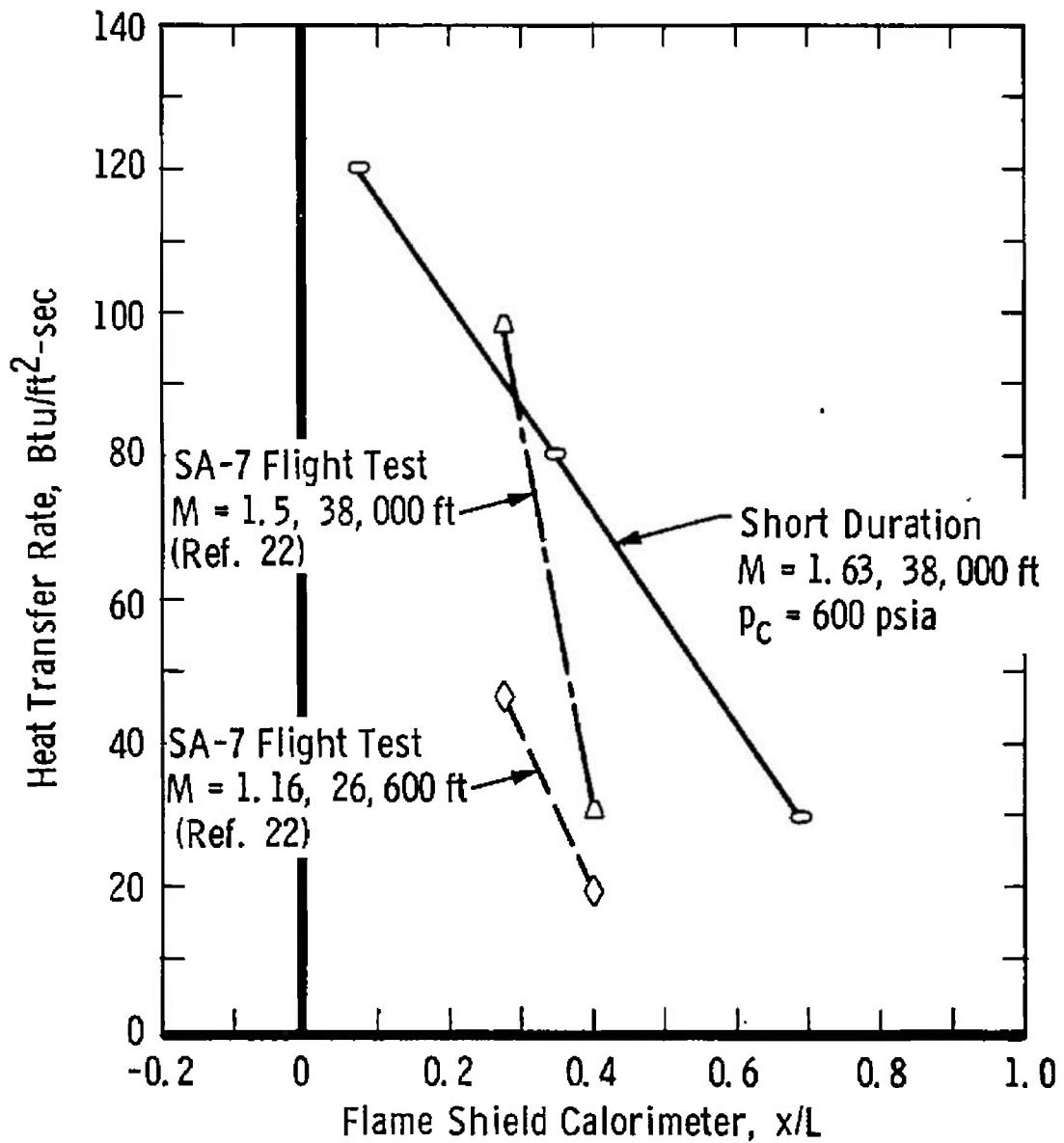
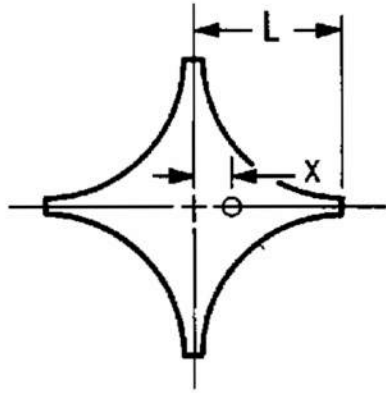


Fig. 29 Typical Temperature and Heat Transfer Time History for a Flight Test Heat Transfer Gage



a. Comparison of Short- and Long-Duration Model Data

Fig. 30 Flame Shield Heat Transfer Rate



b. Comparison of Model and Flight Data
Fig. 30 Concluded

TABLE I
ENGINE AND AFTERBODY DESIGN PARAMETERS

	Short Duration		Long Duration	Flight Vehicle
Afterbody Diameter, in.	14.8		14.8	277
Distance from Nozzle Exit to Heat Shield, in.	2.9		2.9	54.0
Distance from Nozzle Exit to Flame Shield, in.	0.25		0.25	6.0
Nozzle Throat Diameter, in.	0.884		0.9	16.50
Nozzle Exit Diameter, in.	2.5		2.5	46.74
Nozzle Characteristics	contoured		contoured	contoured
Exit Angle of Nozzle, deg	3		4	0
Nozzle Expansion Ratio	8.0:1		7.71:1	8.00:1
Chamber Pressure, psia	500	600	500	600
Total Propellant Flow Rate per Engine, lb _m /sec	1.56	1.89	2.23	716
Operating O/F Ratio	2.16	2.44	2.2	2.38
Characteristic Velocity, ft/sec	6200	6200	4590	5537
c* Efficiency, percent	≈100	≈100	79	96
Isentropic Exponent				
Ratio of Specific Heats, γ	1.15	1.20	1.25	1.22
Exhaust Gas Exit Mach Number*	2.98	2.94	3.02	2.98
Exhaust Gas Exit Static Temperature, °R*	4200	4650	2220	3600
Inboard Engine Cant Angle, deg	3	3	0	3
Outboard Engine Cant Angle, deg	6	6	6	6
Fuel	C ₂ H ₄		RP-1	RP-1
Oxidizer	GO ₂		LO ₂	LO ₂

TABLE II
INSTRUMENTATION

Parameter	Estimated System Accuracy	Measuring Device	Range of Measuring Device	Recording Device
	Assumes Steady-State Signal at Operating Level			
Combustion Chamber, Injection, Venturi, Turbine Exhaust, Manifold Pressures (Short Duration)	±2 percent	Kistler Crystal Transducers and Charge Amplifiers	0 to 2000 psid	Direct Print Oscillograph
Charge Tube Pressures (Pre-Fire) and Autovalve Pressures	±2 percent	Conventional Strain-Gage-Type Pressure Transducers	0 to 2500 psia	Strip Charts and Dial Gages
Model Base Pressures (Short Duration)	±5 percent	CAL Crystal Transducers	0 to 15 psid	Oscillograph
Model Base Reference Pressures and Tunnel Aerodynamic Pressures	±0.05 in. Hg	Mercury Manometers	0 to 120 in. Hg	Photograph
Model Base Heat Transfer Gage Temperature Rise (Short Duration)	±5 percent	CAL Thin-Film Gages	0 to 1000°F	Magnetic Tape via SEL - 600
Model Base Temperatures	±5°F	I-C Thermocouples	0 to 200°F	Multichannel Strip Chart
Propellant System Temperatures	±10°F	C-A Thermocouples	0 to 500°F	Strip Charts

UNCLASSIFIED

Security Classification

DOCUMENT CONTROL DATA - R&D

(Security classification of title, body of abstract and indexing annotation must be entered when the overall report is classified)

1 ORIGINATING ACTIVITY (Corporate author) Arnold Engineering Development Center ARO, Inc., Operating Contractor Arnold Air Force Station, Tennessee		2a REPORT SECURITY CLASSIFICATION UNCLASSIFIED	
		2b GROUP N/A	
3 REPORT TITLE EVALUATION OF SHORT-DURATION ROCKET ENGINE TECHNIQUE FOR BASE HEAT TESTING WITH EXTERNAL AIRFLOW			
4 DESCRIPTIVE NOTES (Type of report and inclusive dates) N/A			
5 AUTHOR(S) (Last name, first name, initial) Dawson, John G., Jr., ARO, Inc.			
6 REPORT DATE July 1966	7a TOTAL NO OF PAGES 91	7b NO OF REFS 32	
8a CONTRACT OR GRANT NO AF 40(600)-1200	9a ORIGINATOR'S REPORT NUMBER(S) AEDC-TR-66-103		
b PROJECT NO c System 921A d	9b OTHER REPORT NO(S) (Any other numbers that may be assigned this report) N/A		
10 AVAILABILITY/LIMITATION NOTICES Qualified requesters may obtain copies of this report from DDC. Transmittal to foreign governments and foreign nationals must have prior approval of AEDC.			
11 SUPPLEMENTARY NOTES N/A		12. SPONSORING MILITARY ACTIVITY Arnold Engineering Development Center (AEDC), Air Force Systems Command (AFSC), Arnold AF Station, Tennessee	
13 ABSTRACT Base recirculation data were obtained on a 5.47-percent-scale model of the Saturn I-Block II booster at trajectory Mach numbers of 1.16 and 1.63. The rocket nozzle flow was produced by use of the Cornell Aeronautical Laboratory short-duration combustor. The turbine exhaust gases were simulated by hydrogen. The test objectives were (1) to compare results obtained by the short-duration technique to those obtained by long-duration test methods and (2) to evaluate the operational advantages of the short-duration method as compared to other techniques. A comparison of model test to flight test data is also presented.			

This document has been approved for public release
and its distribution is unlimited.

UNCLASSIFIED
Security Classification